2-1-2012

LOCSET phase locking : operation, diagnostics, and applications

Benjamin Pulford

Follow this and additional works at: https://digitalrepository.unm.edu/ose_etds
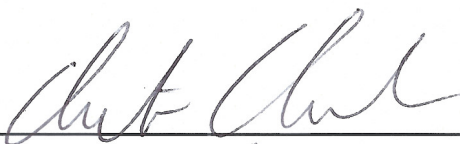
Benjamin N. Pulford
_____

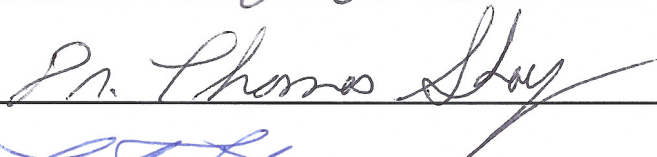*Candidate*

Physics & Astronomy
_____

Department

This dissertation is approved, and it is acceptable in quality
and form for publication:

Approved by the Dissertation Committee:

Dr. Christos Christodoulou, Chairperson _____
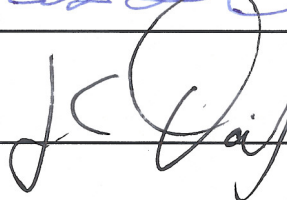
Dr. Thomas Shay _____

Dr. Luke Lester _____

Dr. Jean-Claude Diels _____

LOCSET Phase Locking:
Operation, Diagnostics, and Applications

By

Benjamin N. Pulford

B.S. Applied Physics, Bethel University, 2004
M.S. Optical Science and Engineering, University of New Mexico, 2010

DISSERTATION

Submitted in Partial Fulfillment of the
Requirements for the Degree of

Doctor of Philosophy
Optical Science and Engineering

The University of New Mexico
Albuquerque, New Mexico

December 2011

DEDICATION

I dedicate this dissertation to my wife Effie for her selfless support of all my academic endeavors. I love you Sweets.

ACKNOWLEDGEMENTS

I'd like to begin by acknowledging a string of professors and teachers who saw abilities in me that I was unable to see in myself. First there was Mr. Arlyn Thomas, my high school physics teacher, who somehow found it in himself to ask the right questions and keep my attention in class (more difficult than one might think). A few years later, at Bethel University, I met Dr. Richard Peterson who proceeded to look past my course work struggles and began the cultivation of a young experimentalist. Shortly thereafter, at UNM, there was Dr. Wolfgang Rudolph who, in my first few years of graduate school, instilled in me a relentlessly detailed approach to experimental research without losing focus on the bigger picture. Midway through my graduate career I was introduced to Dr. Thomas Shay, formerly of AFRL and UNM, who brought me into the fold of a tirelessly cultivated research environment focused on individual self-reliance in the bounds of teamwork and community. Said environment played, and continues to play, an important role in the success of this author.

I wish to thank each of my Ph.D. committee members, Dr. Christodoulou, Dr. Lester, Dr. Diels, and Dr. Shay, for their individual efforts pertaining to this dissertation. Without their time and advice this work would not have been possible.

I extend my most humble thanks to all levels of AFRL management for their patience and advice during this undertaking. It isn't everyday you find a workplace willing to permit one of its employees the time and flexibility required to undertake such a lengthy effort.

I'd also like to thank the team of researchers and technicians within RDLA for their time and support in this effort. Simply bouncing ideas around with each of you played an important role in this endeavor.

Last, but certainly not least, I'd like to thank my family for molding me into the person I am today. Your time, love, and efforts did not go unnoticed and will not be forgotten.

LOCSET Phase Locking:
Operation, Diagnostics, and Applications

by
Benjamin N. Pulford

B.S. Applied Physics, Bethel University – 2004
M.S. Optical Science & Engineering, University of New Mexico – 2010
Ph.D. Optical Science & Engineering, University of New Mexico – 2011

ABSTRACT

The aim of this dissertation is to discuss the theoretical and experimental work recently done with the Locking of Optical Coherence via Single-detector Electronic-frequency Tagging (LOCSET) phase locking technique developed and employed here are AFRL. The primary objectives of this effort are to detail the fundamental operation of the LOCSET phase locking technique, recognize the conditions in which the LOCSET control electronics optimally operate, demonstrate LOCSET phase locking with higher channel counts than ever before, and extend the LOCSET technique to correct for low order, atmospherically induced, phase aberrations introduced to the output of a tiled array of coherently combinable beams. The experimental work performed for this effort resulted in the coherent combination of 32 low power optical beams operating with unprecedented LOCSET phase error performance of $\lambda/71$ RMS in a local loop beam combination configuration. The LOCSET phase locking technique was also successfully extended, for the first time, into an Object In the Loop (OIL) configuration by utilizing light scattered off of a remote object as the optical return signal for the LOCSET phase control electronics. Said LOCSET-OIL technique is capable of correcting for low order phase aberrations caused by atmospheric turbulence disturbances applied across a tiled array output.

Table of Contents

Table of Figures

xiv

List of Tables

Chapter 1.   Introduction

In general there are two methods to creating a high power laser system. The first is to invest all R&D efforts into creating a single high power laser that meets specific application requirements. Such a method is fraught with expected and unexpected hurdles such as non-linear effects and material damage thresholds. The second technique is to design and build a number of lower power lasers and somehow merge them into a single, much higher power, laser system. Though such a beam combination system might side step many problems faced by single, very high power lasers, it will inevitably encounter many of its own; not the least of which is how to combine may laser outputs into a single beam easily and efficiently. Such is the topic of this dissertation. In the following chapters the reader will be introduced to some of the more prominent methods of active/electronic phase locking and subsequent methods of coherent beam combination (beam overlap). This dissertation will then progress into a thorough discussion on the theory pertaining to the Locking of Optical Coherence via Single-detector Electronic-frequency Tagging (LOCSET) phase locking technique outlining, in great detail, how the LOCSET electronics generate and apply the required phase error corrections to each beam in a broader beam combination system. From there the reader will be introduced to an important method for measuring the optical phase behavior for both single and multi-beam systems as measured with respect to a stable, frequency shifted, reference beam. Once the reader is comfortable with the general theory of phase error measurements said technique will be applied to measure the phase behavior of a single 100W fiber amplifier as well as the beam combination performance of 2, 16, and 32 channel beams, coherently combined via the LOCSET phase locking technique. This dissertation will then conclude

with a discussion, and demonstration, on how to extend the LOCSET phase locking technique to automatically correct for low order atmospheric aberrations when implemented with a tiled array beam combiner illuminating a remote object immersed in atmospheric turbulence.

Chapter 2.   Background

Before delving into the details of LOCSET operation and implementation it is important to form a general understating of active phase locking and coherent beam combination. An excellent way to achieve said understanding is to review some of the more prominent methods of active optical phase control and beam combination techniques in the literature today. Our discussion will begin with a review of solid state slab lasers and their overall performance in an impressive beam combination system. The focus of the text will then shift to that of high power fiber lasers/amplifiers with their inherent beam quality benefits and their most unfortunate output power down falls. This chapter will then transition into methods of active phase control and beam combination techniques utilized in combining multiple optical beams into a single high power output.

2.1. Solid State Laser Technology (Slab Lasers)

Solid state laser technology has come a long way since 1960 when Theodore Maiman, of Hughes Research Labs, published on the first ever laser demonstration via flash lamp pumping a ruby crystal [1,2]. Though solid state lasers today take many forms one of the more prominent solid state lasers, at least in relation to coherent beam combination, is that of the optically pumped slab laser. Slab lasers are thin, optically pumped, slabs of rare earth doped crystals used to amplify light coupled into it. In relation to coherent beam combination slab lasers are typically implemented in a *master oscillator power amplifier* (MOPA) configuration where the amplification chain begins with a relatively low power seed laser, or *master oscillator (MO)*, maintaining the optical characteristics to be amplified (i.e. wavelength, linewidth, polarization state, etc.). The light from the seed laser is then amplified via sequential amplification stages where, at

each stage, the total optical power is increased while, ideally, maintaining the desired optical characteristics of the seed laser, *the power amplifier (PA)*. In papers published in 2009, McNaught and team reported on the world's first 100kW solid state laser system consisting of seven, coherently combined, 15kW MOPA slab amplifiers [3,4].

Figure 1: Laser system enclosure for a 7 channel, coherently combined, slab laser system for an output of 100kW [3].

Such a demonstration is worthy of much praise but slab laser systems come with their own array of pros and cons. Beginning with the pros, slab lasers are typically quite compact (enclosure for the 100kW slab laser mentioned above is shown in Figure 1) and robust [3,4]. The reader would be hard pressed to find another 100kW solid state laser system with such a small footprint. The con's of the slab laser present themselves in other ways, primarily in the output beam quality, free space optical design, and relatively low electrical to optical efficiencies. For the system shown in Figure 1 each of the 7 beams required separate closed loop adaptive optical (AO) corrections due to distortions of the output wavefront caused by thermal effects in the optically pumped slab gain media [3].

With said AO corrections the final optical output of each beam maintained a respectable beam quality, M^2, of approximately 3; though, in this author's opinion, it came at a relatively high cost in system complexity.

Slab lasers, more efficient than many other laser systems, aren't as efficient as many situations or implementations might require. Reported DC to optical efficiencies of approximately 20% for the 100kW system described above [3,4] are nothing to scoff at but, for high power laser systems, such efficiencies may only be practical in laboratory and/or industrial settings. When considering mobile platforms electrical power comes at a premium as it most likely comes from a portable generator. 20% efficiency for a 100kW optical output dictates that 500kW of electrical power must be supplied to generate 100kW of optical power from the broader slab laser system, a tall order for many mobile applications.

The slab laser system described above is a worthy achievement as it is the first solid state laser system to reach 100kW of optical output power while maintaining respectable beam qualities and reasonable electrical to optical efficiencies. Unfortunately, when electrical power is at premium, slab laser systems may not be the best way to proceed. Therefore, it is worth exploring other, possibly more efficient, light amplification and beam combination methods in the quest to reach such power levels.

2.2. Fiber Lasers/Amplifiers

Optically pumped fiber lasers entered the research scene in 1961, about a year after the demonstration of the first solid state laser [1], when Snitzer and team flash lamped pumped a Neodymium (Nd^{+3}) doped barium crown glass waveguide [5,6]. After said

demo progress in fiber laser research remained relatively stagnant for about 25 years until improvements in fiber production and the availability of low cost per watt diode laser modules (to replace inefficient flash lamp pumping) were well realized [7]. Later, in 1985, Payne and team demonstrated the potential for low loss, and very high gain, rare earth doped fibers [8,9] and seemingly overnight interest in fiber lasers renewed. With high optical gains rare earth doped fibers were no longer constrained to acting as optical gain media in laser cavities. Instead, fiber gain media could be used in a single pass MOPA configuration, described above for slab lasers, greatly simplifying the laser system and paving the way to more and more powerful optical outputs.

Early on, even with high optical gain rare earth doped fibers, maximum optical output power remained in the milli-watt regime primarily because said fiber lasers were only single clad and had to be optically pumped via the fiber core. Core pumping of a single mode fiber amplifier requires single mode, high brightness, diode laser pump modules "which are both expensive and intrinsically limited as far as achievable power in concerned" [7]. With the advent of double clad rare earth gain fiber [10] researchers were no longer limited to core pumping and could now couple single, or multi-mode, pump light into the larger inner cladding of a double clad fiber and still maintain a single mode optical output [7,11]. Optical outputs of single mode fiber amplifiers began increasing from just a few milli-watts into the watt and 10's of watts regime [7] simply because fiber lasers were no longer constrained to core pumping. Later, for the first time in 1999, optical output exceeded 100W in a single mode Yb-doped fiber [12]. Said achievement seemed to open the flood gates in advancements of total optical power from single and multi-mode fiber lasers and amplifiers.

To date 10kW and 50kW fiber amplifiers have been demonstrated by the IPG Photonics

corporation [13,14]. Such an achievement is no small feat but the optical outputs of such

high power fiber amplifiers are multi-mode, maintain very large linewidths, have

relatively poor beam quality, and typically do not maintain a stable polarization state

[14]. Such high power amplifiers are excellent for industrial applications where cutting

and welding of different materials occurs at a very short distance from the amplifier

output. If the applications are more remote and require cutting and welding at a larger

distance then the amplifiers described above are of little use. Due to their poor beam

quality such beams do not propagate well and maintain large spot sizes, much larger than

the diffraction limit, at large distances.

Enter the single mode fiber amplifier, with their near diffraction limited optical outputs,

it is much easier to maintain a smaller spot while propagating large distances.

Unfortunately, single mode fiber amplifiers are plagued with problems when it comes to

high power operation. To date, only 500 watts of single mode, single frequency,

polarized, and near diffraction limited optical outputs have been demonstrated from fiber

amplifiers [15,16,17,18]. The phenomena primarily responsible for these relatively low

optical output powers is known as Stimulated Brillouin Scattering (SBS) and is defined

quite well by Dr. Craig Robin in his recent PhD dissertation [19].

> Stimulated Brillouin scattering is a non-linear optical
>
> interaction between a pump wave and a counter-propagating Stokes
>
> wave mediated by an acoustic wave. Figure 2 shows an input laser at
>
> frequency ω_L scattering from the refractive index variation associated
>
> with an acoustic wave of frequency Ω_B. The reflected Stokes light is

frequency shifted downward since the acoustic wave front is co-propagating with the input laser.
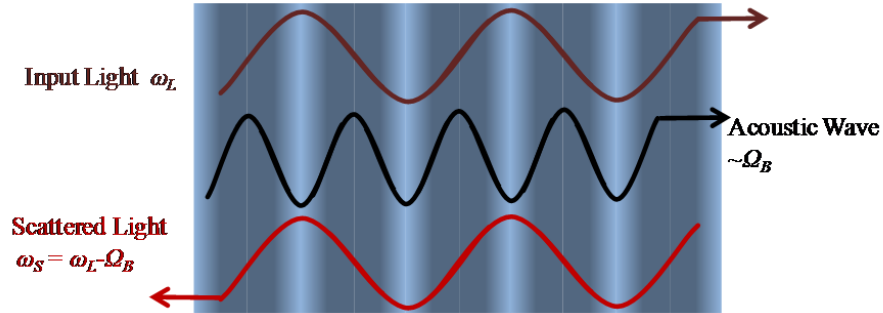
Figure 2: Stimulated Brillouin scattering. Input light at ω_L is scattered by refractive index variations (shown by modulated shading in background) associated with sound wave at Ω_B. The reflected Stokes light, ω_S, is frequency downshifted by Ω_B.

The process is initiated by thermal fluctuations in the fiber which manifest as spontaneous Brillouin scattering. In an optical fiber, the transition from spontaneous to stimulated scattering occurs when interference between the input laser and reflected Stokes light is sufficient to drive the acoustic wave through electrostriction. The combination of single-frequency amplification, long interaction lengths, and tight confinement of the optical field result in the onset of SBS at low power levels.

Even though this discussion is focused on fiber amplifiers much understanding of this process can be gained by discussing the SBS threshold behavior of passive optical fibers as manipulations applied to passive fibers, to suppress SBS, typically work in suppressing SBS in active fibers. The SBS optical power threshold, P_{th}, of a passive fiber is approximated as follows [19],

$$P_{th} \sim \frac{A_{eff}}{g_{B,Max} \cdot L_{eff}}\left(1 + \frac{\Delta v_L}{\Delta v_B}\right), \qquad\qquad 2.1$$

where A_{eff} is the effective non-linear interaction area of the optical mode in the fiber core,

L_{eff} is the effective non-linear interaction length of the optical mode along the length of

the optical fiber, $g_{B,Max}$ is the peak, Lorentzian lined shaped, SBS gain, Δv_L is the laser

linewidth, and Δv_B is the linewidth of the generated SBS signal. Looking at equation 2.1

we realize that there are a number of ways to manipulate, and therefore potentially

increase, the SBS threshold power. The most obvious is to simply increase the active

area, A_{eff}, of the guided optical mode by increasing the area of the fiber core. In practice

this works quite nicely, partially evidenced by the 50kW fiber amplifiers by IPG [14],

but, with no other manipulations, it will result in multi- mode operation of the fiber

amplifier and therefore degrade the output beam quality. The next possible method is to

decrease the effective non-linear interaction length, L_{eff}, between the optical mode and

the fiber core. The problem here is that, by shortening the fiber amplifier, you will also

reduce your pump interaction length with the fiber material and therefore lower the

overall optical to optical efficiency as well as total output power of the fiber amplifier

(optical to optical efficiencies of 70% are often reported for single mode fiber amplifiers

[7,19]). This can be mitigated by increasing the rare earth dopant concentration in the

fiber core but that too comes with its own set of tradeoffs. The third easily implementable

change, without altering the material properties of the fiber, is to broaden the linewidth of

the output laser signal by broadening the linewidth of the amplifier seed source. This

method is very effective in mitigating SBS as, again, is evidenced by the 50kW IPG laser

systems with greater than 10nm linewidths [14], but it is not very conducive to coherent

beam combination applications. By increasing the linewidth of the amplified signal the

coherence length of that particular beam will decrease as dictated by the following expression,

$$l_c = \frac{c}{\Delta \nu_L},$$

<div align="right">2.2</div>

where l_c is the coherence length of an optical beam, c is the speed of light (~3x10^8 m/s) and $\Delta \nu_L$ is the linewidth of the laser source. By decreasing the coherence length of any or all beams in a coherent beam combination system you introduce an optical path length matching requirement that may be impossible to overcome.

It is clear that fiber amplifiers have some significant advantages over other solid state lasers systems. Given their high optical to optical efficiencies and, for single mode systems, nearly diffraction limited optical outputs, fiber amplifier systems appear to be the better choice for longer distance applications. Unfortunately, given the state of current fiber amplifier technology, bulk solid state laser systems are capable of much higher optical output powers with the caveat of lower beam quality, lower operating efficiencies, and higher system complexity. This output power gap can potentially be closed, while maintaining excellent output beam quality, by coherently combining many of the high power fiber amplifier outputs together into a single, much higher power, output. Such methods of active phase locking and beam combination are discussed in detail in the sections to follow.

2.3. Active Phase Control Technologies

The benefits of beam combination are, for the most part, inherently understood by everyone whether or not he or she fully realizes it. Consider a young child playing in a dark room with a couple of flashlights. It doesn't take very long for that child to figure out that if he or she points both flash lights at the same space on a wall the combined beam spot gets much brighter than if only one flashlight was used to illuminate the same space. This simple example is an excellent demonstration of the benefits of incoherent beam combination. Two mutually incoherent sources, the flashlights, are used to illuminate a common space on a wall. As it turns out the combined beam spot will be twice as bright, or intense, as that of a single flashlight.
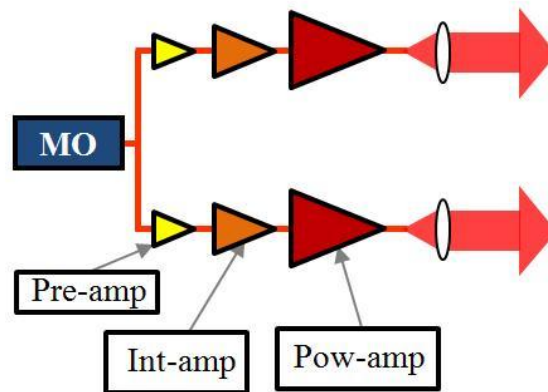
Figure 3: Multi-channel beam combination system consisting of 2 identical MOPA chains sharing a common master oscillator (MO).

This same, very basic, principle can also be applied to lasers though the rules change a bit if the laser sources are not mutually incoherent. Let's assume that there are two master oscillator power amplifier (MOPA) chains, identical in every way, sharing a common master oscillator (MO), in a beam combination system similar to that shown in Figure 3. The output of said beam combination system is that of a basic tiled array of

arbitrarily distributed sub-apertures emitting collimated beams with common optical characteristics (wavelength, linewidth, polarization, etc). In the scenario shown in Figure 3 the two beams will combine in the far field some distance away from the launch aperture of the beam combination system. Not taking into account path and coherence length considerations, when the individual beams overlap on a wall, or some other object, in the far field the combined spot will not be a single uniform spot twice as bright as that of a single MOPA; as demonstrated with the mutually incoherent flashlights above. This time the resulting spot will be a series of bright and dark fringes moving in time due to temporal variations in each beams optical path length. This new, more complex, interaction of the two beams is known as coherent beam combination and will be exploited in the beam combination discussions to follow.

In order to fully realize the benefits of coherent beam combination one must somehow control and correct for the time varying optical phase states of each individual beam in the beam combination system. This can either be done actively or passively. *For the purposes of this dissertation we will limit the scope of our discussion to methods of active phase control and related methods of beam combination*. First, the reader will be introduced to three of the more prominent methods of active phase control in coherent beam combination systems including the heterodyne, Stochastic Parallel Gradient Decent (SPGD), and Locking of Optical Coherence via Single-detector Electronic-frequency Tagging (LOCSET) techniques. From there we will continue our discussion with three prominent methods of beam combination to include tiled arrays, polarization beam combination, and Diffractive Optical Elements (DOE). The chapter will then conclude

with a brief discussion on methods of correcting for atmospheric turbulence by including

the illuminated remote object in the phase control feedback loop.

2.3.1 Heterodyne Technique
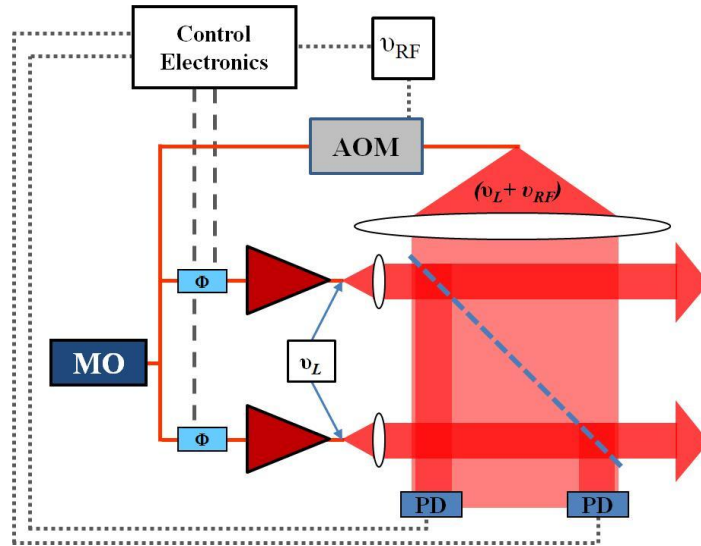
Figure 4: Heterodyne phase locking setup. Each optical channel phase locks to a common
frequency shifted reference beam (similar to setup shown in reference [20]).

The basic principles of the heterodyne active phase control technique are possibly

the most intuitive of the three techniques to understand. The heterodyne beam

combination setup shown in Figure 4 begins to the far left with a single master oscillator

(MO), the output of which is split three ways. Two of the beams pass through piston

phase controllers and are subsequently amplified. The amplified beams are then

collimated and directed to propagate along spatially separate beam paths and incident on

a common partial reflector (beam sampler). A fraction of the light in each beam is

reflected at the beam sampler and incident on separate photodetectors. Referring back to

the MO output the remaining beam passes through an acousto-optic modulator where the

light undergoes an RF shift in frequency. The frequency shifted light is collimated into a

single beam, larger than the tiled output of the amplified beams, and overlapped and interfered with both sampled beams at their respective photodetectors. Each photodetector measures an optical beat note, due to the interference between the frequency shifted reference beam and the individually sampled beams, that contains the optical phase information of each amplified beam measured with respect to the common reference beam [20,21,22,23,24]. The control electronics then determine the phase difference of each amplified beam, measured with respect to the common frequency shifted reference beam, and minimizes those differences [20,21,22,23,24]. With the phase difference of the individual beams minimized with respect to the common reference beam the two amplified beams will also have a minimized phase difference between each other resulting, ideally, in optimal beam combination at the output of the beam combination system.
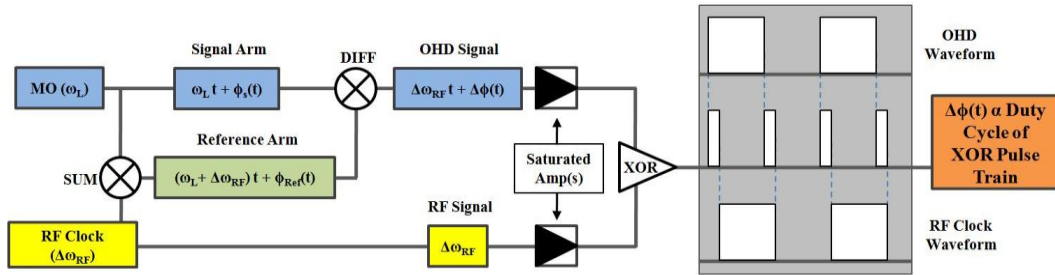
Figure 5: Optical Heterodyne beam combination control schematic. Goal is to minimize the pulse width from the exclusive OR (XOR) output of the control circuit [20].

Fundamental control loop operation for heterodyne beam combination aiming to minimize the phase difference between a single beam and a frequency shifted reference beam is shown in Figure 5 and is further discussed in reference [20]. The schematic begins to the far left with light of frequency ω_L generated at the MO. The light is split, similar to that shown in Figure 4, two ways with the upper most beam maintaining its

14

original frequency, ω_L, and phase state, ϕ_s, shown in Figure 5 as $\left(\omega_L \cdot t + \phi_s(t)\right)$. The second beam undergoes a frequency shift, $\Delta\omega_{RF}$, and maintains its own unique optical phase state, ϕ_{Ref}, shown in Figure 5 as $\left(\left(\omega_L + \Delta\omega_{RF}\right) \cdot t + \phi_{REF}(t)\right)$. When the two beams interfere together at the photodetector it effectively measures the difference in frequency and difference in phase between the two optical signals represented in Figure 5 as $\left(\Delta\omega_{RF} \cdot t + \Delta\phi(t)\right)$ where $\Delta\phi(t) = \phi_{REF}(t) - \phi_s(t)$ and labeled the optical heterodyne (OHD) signal. The oscillatory photodetector output is then 'square up' into a TTL like signal via a saturated electronic amplifier. The squared up OHD signal is then compared to the squared up RF reference signal, responsible for the frequency shift to the optical reference beam, via an exclusive OR circuit (XOR). When the OHD and the RF signals are not in phase a train of pulses, with some temporal width, are generated. These pulse widths are proportional to the optical phase difference between the frequency shifted reference beam and the original signal beam [20]. The circuit, armed with an error signal proportional to the optical phase difference, then applies the appropriate phase corrections to minimize the pulse widths in the train of pulses from the XOR circuit resulting in zero, or very small, phase difference between the frequency shifted reference beam and the original signal beam [20].

The heterodyne beam combination system described above has the advantage of being relatively simple to implement while maintaining excellent beam combination performance with RMS phase errors as low as $\lambda/80$ reported for 2 channel beam combination [23]. The down falls of such a beam combination system come when trying to scale to much higher channel counts. For example, when trying to combine 25 beams,

each beam must be well aligned to the common frequency shifted reference beam with minimal tip/tilt, and other wavefront errors, between them when incident on their individual photodetectors. Logistically this can be quite the nightmare to achieve in a laboratory setting, not to mention in a fieldable system. One other issue to be concerned with is in the event of losing the reference beam, maybe from a serious pointing error or a fiber/optical component failure in the reference beam path, the entire system would lose phase locking capabilities. Depending on the application it may not be in the best interest of a beam combination system to put so much faith in the operation and alignment of a single beam.

2.3.2 SPGD Technique

The primary limitation of the heterodyne technique is the need for multiple photodetectors, one for each beam, to phase lock each array element to a common frequency shifted reference. To overcome this limitation methods of coherent beam combination that utilize just one photodetector have been devised. One of the more prominent single detector beam combination methods is that known as the Stochastic Parallel Gradient Decent (SPGD) method [25,26,27,28,29,30] and is described in detail in the following text.
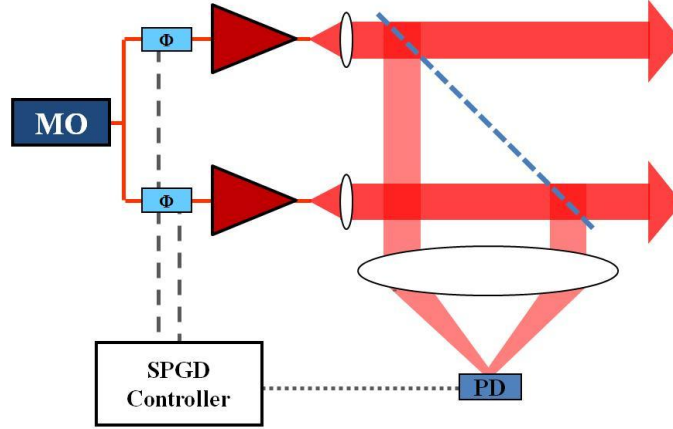
Figure 6: Stochastic Parallel Gradient Decent (SPGD) method of coherent beam combination. SPGD utilizes only a single photodetector to coherently combine N beams.

The SPGD method of coherent beam combination, shown in Figure 6, works much like the name implies. A *stochastic*, or random, perturbation in optical phase is applied, *in parallel*, to each phase controlled beam in the broader beam combination system. An algorithm working to minimize an intensity based error metric works to *descend*, or minimize, said metric along a error metric *gradient* in an effort to coherently combine multiple beams at the photodetector. By coherently combining the tiled array shown in Figure 6 at the photodetector each beam will be in phase with the other(s) at the exit aperture of the beam combination system, just to the right of the partial reflector in Figure 6.

To begin our discussion on SPGD implementation lets define a vector that represents the optical phase state, $\vec{\phi}_i$, of an N element array of optical beams [31],

$$\vec{\phi}_i = \left\{ \phi_1, \phi_2, \phi_3, ..., \phi_N \right\}. \qquad 2.3$$

Regardless of the phase state of the tiled array the SPGD controller will apply a random perturbation, $\vec{\rho}$, to $\vec{\phi}_i$ as shown mathematically below,

$$\hat{\phi} = \vec{\phi}_i + \vec{\rho}.$$

2.4

How the random phase perturbation, $\vec{\rho}$, is chosen is essentially a matter of preference and

how SPGD is implemented in the beam combination system. The simplest method of

implementing $\vec{\rho}$ is to predetermine a constant piston phase step size to be applied to each

phase modulator in the beam combination system leaving only the sign of said step, for

each phase controlled element, to the stochastic determinations of the SPDG algorithm

[31]. After said random phase perturbation a scalar error value, ε, is determined by

calculating the difference in intensity as measured for both phase states, $\vec{\phi}_i$ and $\hat{\phi}$,

$$\varepsilon = Int\left(\hat{\phi}\right) - Int\left(\vec{\phi}\right),$$

2.5

where $Int\left(\vec{\phi}_j\right)$ is the intensity, measured at the photodetector, of the combined beam for

some array phase state, $\vec{\phi}_j$. Said error value, ε, is then combined (multiplied) by another

scalar value, μ, which corresponds to SPGD control loop parameters such as electronic

gain and whether or not the SPGD system is working to maximize or minimize the

intensity at the photodetector [25]. When maximizing the intensity μ is chosen to be

positive and when minimizing the intensity of the combined beam μ is chosen to be

negative. The combined value, $\mu \cdot \varepsilon$, is then multiplied by the stochastically chosen phase

perturbation $\vec{\rho}$ to determine the required phase correction, $\Delta\vec{\phi}$,

$$\Delta\vec{\phi} = \pm\mu \cdot \varepsilon \cdot \vec{\rho},$$

2.6

to be applied to the original unperturbed array phase state, $\vec{\phi}_i$, to generate a corrected, or

more optical, phase state, $\vec{\phi}_{i+1}$,

$$\vec{\phi}_{i+1} = \vec{\phi}_i + \Delta\vec{\phi}.$$

2.7

The corrected phase state, $\vec{\phi}_{i+1}$, isn't necessarily the optimal phase state of the array when aiming to achieve coherent beam combination but, if the control algorithm is implemented correctly, it will be a step in the right direction (i.e. a more, or at least equally, optimal phase state than $\vec{\phi}_i$). The algorithm is then repeated, or iterated, until the SPGD system converges to optimal beam combination at the control loop photodetector [26,28] as shown in Figure 7.
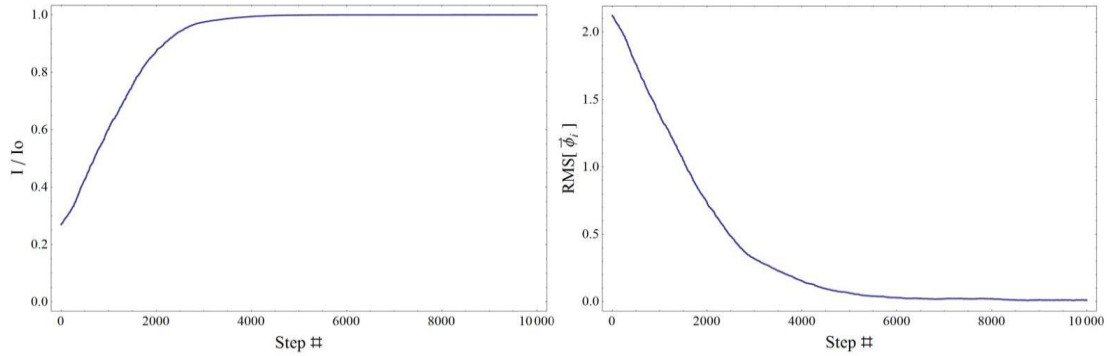
Figure 7: Results of numerical SPDG simulation. Left: Normalized peak intensity, as measured at the photodetector in Figure 6, for a 10 beam coherent beam combination system. Right: RMS value calculated from the phase states of the 10 coherently combined beams. Both: For simplicity all beams perfectly overlapped at photodetector (i.e. not a tiled array).

Shown in Figure 7 are the results of a numerical SPGD simulation written by this author. For said simulation it was assumed that there were 10 perfectly overlapped beams (not tiled), identical in nearly every way, beginning with randomly chosen phase states. At left in Figure 7, the peak intensity of the combined beam, as measured at the photodetector in Figure 6, is calculated for the applied phase state corrections, and normalized to the theoretical maximum value I_o, for each of 10,000 iterations of the SPGD algorithm (it is important to note that Figure 7 does not include intensity

19

fluctuations resulting from the stochastic phase perturbations needed to determine the error term, ε). At right in Figure 7 is the calculated RMS phase value of the combined beam for each iteration of the SPGD algorithm. Notice that as the peak intensity of the combined beam is optimized the RMS phase behavior of the combined beam approaches zero indicating that, by maximizing the optical intensity of the combined beam, the system is also minimizing the optical phase difference between the 10 beams.

SPGD is an excellent method of optical phase locking as it is relatively easy to implement in a real world system/experiment and has demonstrated phase locking performance of λ/30 per channel in a 48 channel, multi-detector system (separate SPGD controllers for each tiled array element) [32]. SPGD systems aren't without their problems though with the primary limitation being the relationship between the SPGD control loop bandwidth and the number of beams said technique is trying to combine. Though never explicitly stated, it can be inferred from the literature that the bandwidth of the SPGD control loop, BW_{SPGD}, is inversely proportional to the number of parameters, N, the control loop is working to correct [28],

$$BW_{SPGD} \propto \frac{1}{N}.$$

2.8

Therefore, assuming only piston phase control on each of N beams in a coherent beam combination system, as the total number of channels increases the SPGD control bandwidth will decrease accordingly. In the literature system sampling rates of 100kHz are often reported. Therefore, if the beam combination system has 10 beams the system bandwidth is reduced to at least 10kHz; if there are 100 beams the bandwidth is reduced even further to at least 1kHz. Depending on the application these tradeoffs may be

acceptable. If higher bandwidths are required then another phase locking technique may have to be implemented.

It is also worth noting that, as alluded to above, the SPGD beam combination technique is not limited to only piston phase corrections. Because the system is stochastic and intensity based any number of corrections can be applied to the combined beams such as individual tip/tilt and other higher order wavefront controls [26]. This added benefit doesn't come without a cost as the number of corrected phase aberrations in each beam increases the number of correction parameters, N, in the SPGD control loop. This increase in the N will further reduce the SPGD system bandwidth, as dictated by equation 2.8, but, on a more positive note, this can increase the beam combination performance in turbulent scenarios beyond that of phase locking techniques that can only apply piston phase corrections [26].

2.3.3 LOCSET Technique

Just like the SPGD method of coherent beam combination the Locking of Optical Coherence via Single-detector Electronic-frequency Tagging (LOCSET) technique, shown in Figure 8, utilizes a single photodetector to generate the necessary error correction signal to achieve optimal phase locking. Unlike the SPGD method, LOCSET is not a stochastic, intensity based, process. Instead, via a clever coherent RF demodulation technique, the LOCSET electronics is capable of independently determining an error signal proportional to the optical phase difference of each beam measured with respect to every other beam in the broader beam combination system [33,34,35,36,37,38,39,40,41,42,43]. Because LOCSET phase locking lies at the very heart of this dissertation it will not be described in great detail here. Instead this author

will present only a broad overview of the LOCSET phase locking technique and refer the

reader to Chapter 3 where LOCSET is described in much greater detail.
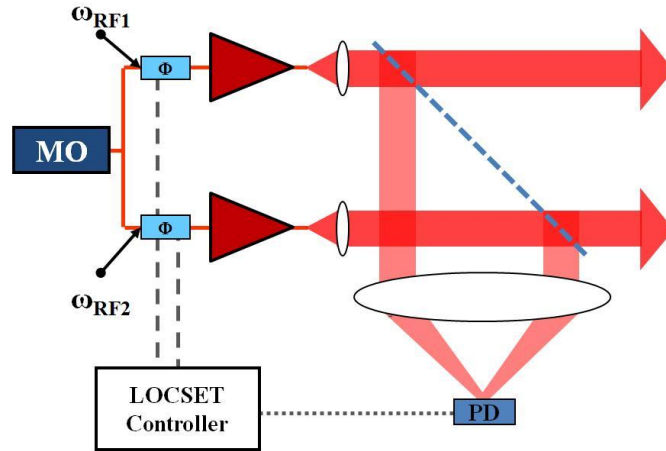
Figure 8: Locking of Optical Coherence via Single-detector Electronic-frequency Tagging (LOCSET) method of coherent beam combination. LOCSET is capable of determining the optical phase difference of a single beam as measured with respect to rest of the beams in the coherent beam combination system

The LOCSET phase locking technique, shown in Figure 8, on the surface looks

much like the SPGD technique described earlier. The system begins with a shared master

oscillator (MO), the output of which is split N ways (as shown in Figure 8: N = 2). Each

of the N beams passes through a phase modulator affording the LOCSET control

electronics the ability to apply piston phase corrections to each beam in the system in an

effort to coherently combine said beams at the photodetector. Each of the N beams is then

amplified, collimated, and launched from the exit aperture of the system (as shown in

Figure 8 the exit aperture is just after the partial reflector). The sampled light from the

partial reflector is then overlapped and interfered on a single photodetector that feeds into

the LOCSET control electronics. To achieve optimal beam combination each of the N

beams is 'tagged' with a small amplitude phase dither of some unique RF frequency. Said

phase dithers are then measured at the photodetector as an intensity interference beat note

that contains the phase information needed for coherent beam combination

[33,34,35,36,37,38,39,40,41,42,43].

There are two configurations of the LOCSET phase locking technique: Self-Referenced [35,37,41,42] and Self-Synchronous [33,34,43]. The reader is referred to Chapter 3 for the full derivation but the self-referenced error signal expression for a single channel (x^{th} channel), S_{SRX}, that governs LOCSET's decision making process is written as follows,

$$S_{SRx} = R_{PD} \cdot P_x^{\frac{1}{2}} \cdot J_1(\beta_x) \left(P_u^{\frac{1}{2}} \sin(\phi_u - \phi_x) + \frac{1}{2} \sum_{\substack{j=1 \\ j \neq x}}^{N-1} P_j^{\frac{1}{2}} \cdot J_o(\beta_j) \cdot \sin(\phi_j - \phi_x) \right). \qquad 2.9$$

Here S_{SRX} is the self referenced electronic error signal for the xth phase modulated channel, R_{PD} is the responsivity of the photodetector, P_x, is the optical power of the xth phase modulated channel of interest (the channel the system is working to correct), and β_x is the amplitude of the unique RF phase modulation applied to the xth channel. Other important parameters in equation 2.9 are P_u, the optical power in the un-modulated reference beam (if one is present), P_j, the optical power in the jth phase modulated beam were $j \neq x$, and ϕ_u, ϕ_x and ϕ_j are the optical phase states of the un-modulated reference beam, the xth phase modulated beam, and the jth phase modulated beams respectively (again: $j \neq x$). Notice that the error signal is proportional to the sine of the phase difference between the un-modulated reference beam and the xth phase modulated beam of interest $\left(\sin(\phi_u - \phi_x) \right)$ as well as the sum of the sine of the phase differences between the xth phase modulated beam of interests and the remaining j phase modulated beams

23

$$\left(\sum_{\substack{j=1 \\ j \neq x}}^{N-1} P_j^{\frac{1}{2}} \cdot J_o\left(\beta_j\right) \cdot \sin\left(\phi_j - \phi_x\right) \right).$$ This indicates that the independently generated LOCSET

error signals for each of the phase modulated channels is proportional to the optical phase

difference between each individual channel measured with respect all other beams in the

coherent beam combination system.

Because the phase behavior of each beam is known with respect to all other

beams in the system an un-modulated reference beam is no longer needed. This is

evidenced by setting the optical power in of the un-modulated reference beam in equation

2.9 to zero and obtaining an expression for the self-synchronous LOCSET error signal,

S_{SSx}, shown below [33,34,43],

$$S_{SSx} = R_{PD} \cdot P_x^{\frac{1}{2}} \cdot J_1\left(\beta_x\right) \frac{1}{2} \sum_{\substack{j=1 \\ j \neq x}}^{N-1} P_j^{\frac{1}{2}} \cdot J_o\left(\beta_j\right) \cdot \sin\left(\phi_j - \phi_x\right). \qquad 2.10$$

The reason LOCSET is capable of operating without a reference beam is because it

measures the relative phase error of a single beam with respect to every other beam in the

system. Because the phase information of a given beam is known with respect to all

others the reference beam is no longer needed, as it is only a single element of the

broader coherently combined beam.

The inherent benefits of LOCSET, when compared to the heterodyne and SPGD

phase locking techniques described above are its single detector operation and, since each

control loop channel operates independently of the rest, the control loop bandwidth is

independent of the number of phase controllable channels in the system [33]. Primarily

due to LOCSET's bandwidth independence from the number of phase controllable

channels in the broader beam combination system it was determined to be the best choice

for the research described in this dissertation as this author aimed, and accomplished, to

demonstrate LOCSET phase locking for 32 coherently combined beams, twice the

previous LOCSET record of 16, with excellent beam combination performance ($\sim\lambda/71$

RMS for 32 channels, also a LOCSET record).

2.3.4 Summary of Active Phase Locking Techniques

	Heterodyne	SPGD	LOCSET
Error Metric:	Phase	Intensity	Phase
# Photodetectors:	Multiple (1 for each beam)	1 (or) Multiple	1
# Chls. Demonstrated:	7	8 – (single det.) 48 – (multi det.)	32
RMS Phase Error Performance:	$\lambda/80$ (2 chl.)	$\lambda/30$ (2 chl.)	$\lambda/83$ (2 chl. – best) $\lambda/66$ (2 chl. – typ.) $\lambda/71$ (32 chl. – best) $\lambda/50$ (32 chl. – typ.)
Scalable to High Chl. Counts?	NO	YES	YES
Limited to Piston Phase Corrections?	YES	NO	YES

Table 1: Comparison between Heterodyne, SPGD, and LOCSET phase locking techniques.

Shown in

Table 1 is a comparison between the three methods of optical phase locking described

above. It is impossible to declare one method superior to the others as each technique has

its own strengths and weaknesses. If phase corrections beyond piston phase are desired

then SPGD is likely the method of choice. If scaling to large channel counts, with low

RMS phase errors in the combined beam, is the goal then the LOCSET technique is

probably the best option. When an application only involves a few beams and overall

system simplicity is the dominating decision point then the Heterodyne phase locking

technique is probably the best option. For the purposes of this dissertation the LOCSET

phase locking technique was chosen for its superior capability of demonstrating high

channel counts with excellent beam combination performance.

2.4. Prominent Methods of Beam Combination

Establishing methods of controlling and optimizing the optical phase state of a

combined beam is just part of the broader beam combination story. Another important

consideration is how the multiple beams of the beam combination system are going to be

overlapped, or combined. There are many established methods of beam combining

reported in the literature but there are three that stand out when considering high power

applications: tiled arrays, polarization beam combination, and the utilization of diffractive

optical elements (DOE) to co-propagate multiple beams.

2.4.1 Tiled Array Beam Combination
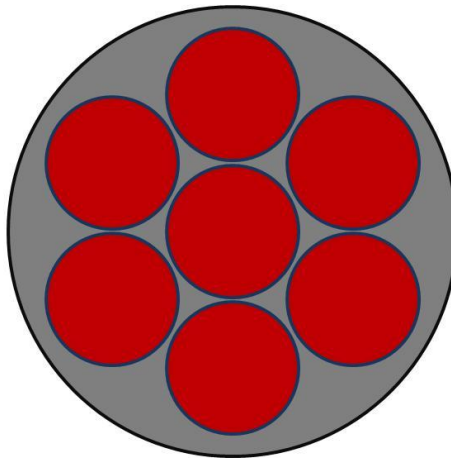
Figure 9: Seven element, hexagonal close packed, tiled array.

The general method of tiled array beam combination makes no effort to perfectly

overlap and co-propagate multiple beams in a broader beam combination system

[44,45,46]. Instead, tiled arrays consist of multiple optical beams exiting spatially

separate array sub-apertures that typically only combine on an object a great distance

away. Assuming that each beam in the tiled array is optically identical, and therefore

mutually coherent, the pattern formed in the far field is not that of a single uniform spot

but instead a complex pattern of bright and dark fringes. The pattern and relative intensity

of each fringe in the far field is dictated primarily by the array arrangement and optical

illumination of each sub-aperture [44,45,46]. To date tiled arrays have been demonstrated

with up to 48beams in coherent beam combination systems [32].
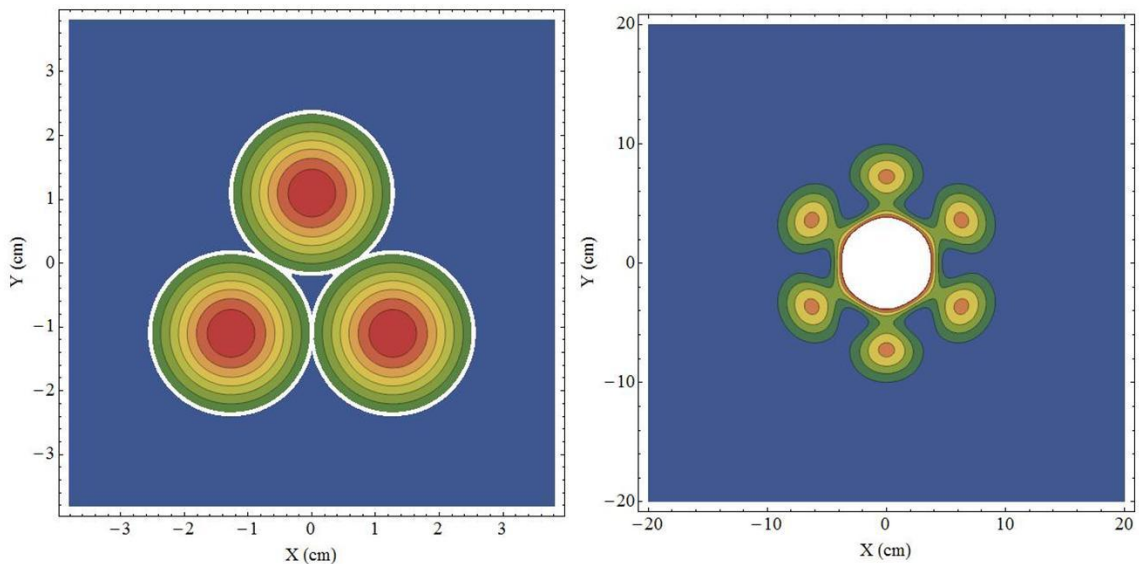
Figure 10: Left: Close packed triangle array of sub-apertures optically illuminated with Gaussian profile beams. Right: Resulting ideal far field diffraction pattern at a distance of 2km.

Shown in Figure 10 are the results of a Fraunhofer beam propagation simulation

written by this author. To the left of Figure 10 is a simple three element, triangle packed,

array of Gaussian illuminated circular sub-apertures. If the output of said array is allowed

to propagate a distance of 2km in a turbulence free environment the interference pattern

seen at said distance will look like that shown to the right of Figure 10. Notice that, as

mentioned above, the resulting beam spot from the tiled array is an interference pattern of

bright and dark fringes with approximately 61% of the total optical power found in the

central lobe (the remaining light is lost to the side lobes).

Due to the inefficiency of the resulting combined beam it quickly becomes clear

that tiled arrays may not necessarily be the best choice for coherent beam combination.

However, said inefficiencies must be weighed against the advantages of such a system.

First, and probably the most important for high power applications, is that the full optical

power of the system is distributed over multiple array sub-apertures and therefore lowers

the thermal load on any single optical component. Often, when working with high power

laser systems, the thermal load on the final optical component(s) is a little closer to its

damage threshold than one would like. It is also worth noting that such an advantage

lowers the chances that the entire system will fail if a single component fails due to

optical damage (i.e. it is common knowledge that a speck of dust in a high power beam

can wreck havoc on a laser system). If one of N beams in the tiled array fail, N-1 beams

still remain and can perform their intended function. If multiple beams are somehow

combined into a single beam, or said system is simply a single high power laser or

amplifier, and the final optic of said system were to fail the entire system would also fail.

Another important advantage of a tiled array over a single beam output is its ability to

perform non-mechanical beam steering. By appropriately adjusting the piston phase

states of each individual array element, effectively phase blazing the full tiled array

output, it is possible to steer the far field diffraction pattern within the broader limits of

the envelope defined by far field diffraction of a single sub-aperture output. Such an

advantage may not allow the system to steer the combined beam over a large solid angle

but it does present the possibility of correcting for small angle inertial jitter in a mechanical beam director.

When considering tiled array beam combination the power in the bucket inefficiencies must be weighed against the thermal and pointing advantages described above. If a user requires efficiency over all else then the beam combination techniques to be described below may be a better fit. If fine pointing and/or lower thermal risk is the governing feature of a specific application than tiled arrays may be the way to go.

The reader might be asking his or herself if such stand alone tiled arrays function well when propagating through turbulent conditions. The simple answer to this question is that they can function well but only if some form of remote sensing is employed to measure and correct for said atmospheric turbulence. This can be done simply by utilizing the light scattered from the illuminated object as an error signal for the phase control electronics. Such techniques will be introduced in a later section of this chapter.

2.4.2 Polarization Beam Combination
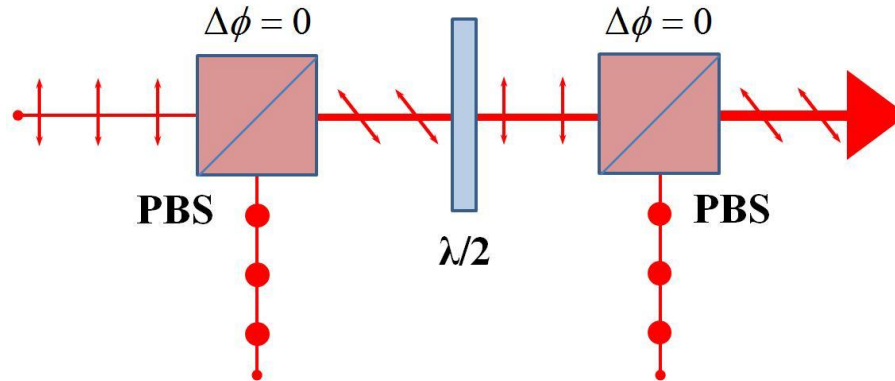
Figure 11: Basic polarization beam combination setup employed by R. Uberna and team [47,48]. If the difference in optical phase between each of the two beams, incident at each polarizing beam splitter (PBS), is held at zero then the system will produce a single higher power beam at the exit port of the final PBS in the system.

The polarization beam combination system shown in Figure 11 is a very elegant method of overlapping multiple linearly polarized beams sharing common wavelength and optical linewidths [47,48 ,49]. The polarization beam combination method begins by overlapping two orthogonal, linearly polarized beams, via a single polarizing beam splitter (PBS). Regardless of the relative phase states between the two beams incident on said PBS a single beam will result at the output. Unfortunately, without some form of piston phase control on the two beams, the combined output beam will maintain a randomly polarization state that varies as a function of time. This is fine if a particular application requires only 2 beams to be combined and isn't concerned about the polarization state of the combined output. If however the application requires more beams to be combined together, or simply a stable linear polarization state, some method of piston phase control must be applied to each beam in the system (i.e. via SPDG or LOCSET described above) [47,48 ,49].

For the sake of argument let's say some ideal method of phase control is applied to each beam in the polarization beam combination system shown in Figure 11. Assume than that said phase controller is utilized to keep the relative phase difference between each of the two beams incident on the left most PBS in Figure 11 at zero for all time. The resulting combined beam will maintain a stable linear polarization state with an orientation dictated by the relative intensities of the beams combined together [47,48,49]. Regardless of how the combined beam's linear polarization is oriented, as long as it is stable in time, it can be re-oriented along the transmission axis of the next PBS via a half wave plate. Then, at the second PBS, shown in Figure 11, the previously combined beam is mixed again with another orthogonally linear polarized beam. If the phase state between these two beams is also held constant at zero, at the second PBS, the resulting combined beam (now consisting of 3 independent beams) will maintain a new stable linear polarization state [47,48,49]. It quickly becomes clear that if the piston phase state of each beam to be combined can be set such that the relative phase difference between each pair of beams, at each PBS, is equal to zero then the system will output a single, higher power, linear polarized beam from the exit port of the final PBS.

With its relative simplicity it is tempting to think of the polarization beam combination method described above as a magic bullet of sorts for overlapping multiple, coherently combinable, optical beams. This however is not necessarily the case, especially for high power applications. As one might expect the polarization beam combination method is very sensitive to the input polarization of each beam to be combined. Polarizing optics typically respond very deliberately to an optical input depending on its polarization state. For instance, PBS's are often designed to reflect

either the s or p polarization while transmitting the other. If a beam incident on a PBS has polarization components in both the s and p directions, possibly because of an elliptical polarization state or a linear polarization state that isn't oriented exactly horizontal or vertical to the axis of the PBS, the beam will be divided into two spatially separate beams, one reflecting and the other transmitting, according to the proportions of the light with s and p polarization components. Such losses will lower the overall efficiency of the coherent beam combination system and therefore need to be minimized via very careful alignment and control of individual amplifier output polarization states.

One other consideration to be made is that of the losses of each individual PBS optic in the broader beam combination system. PBS optics designed for high power applications often lose about 5% of the input light due to unwanted reflections and/or absorption. Considering that the first two beams, to the far left in Figure 11, must pass through every PBS in the coherent beam combination system before exiting the output aperture the losses on said beams can quickly add up. For example, if the polarization beam combination system contains 7 beams, and therefore six PBS's, the first two beams will be reduced in total power by approximately 25% (assuming 5% loss at each PBS) before exiting the beam combination system. One way or another, either via absorption or collection at a beam dump, this loss will likely turn into unwanted heat. For high power systems this heat load could be very significant.

In summary, when pondering a polarization beam combiner for use in a broader coherent beam combination system, it is important to consider which PBS optics to use as well as the stringent polarization requirements on each of the beams to be coherently combined. As a general rule the relationship between power handling capabilities of

PBS's is directly proportional to said optic's overall optical loss. For example, for lower power applications it's often possible to purchase a low loss, though low damage threshold, thin film polarizer. For much higher power applications one is often limited to more lossy birefringent polarization beam splitting cubes, or similar optics.

2.4.3 DOE Beam Combination

To understand the basic operation of a Diffractive Optical Element (DOE) beam combiner one simply has to consider the basic principles of a transmission grating. When a single beam is incident on the surface of a transmission grating multiple beams, or orders, will emerge from the other side, the separation and relative strength of which is dictated primarily by the number of blazes or etches per unit length written into the gratings surface. It is important to realize that, because each of the resulting beams transmitted from the grating originated from a common beam, the relative phase difference between each transmitted beam is zero just after the exit surface of the grating.

Let's now reverse the process of said transmission grating in the previous example. Assume now that, instead of just a single beam, multiple beams are incident on the surface of same transmission grating via the same optical paths defined by the multiple orders created in the previous example. Assuming that each beam is nearly identical to the others, and that the relative phase difference between each beam is zero at the grating surface, the resulting combined beam, shown in Figure 12, will be that of a single beam containing nearly the full optical power of all beams in the beam combination system.
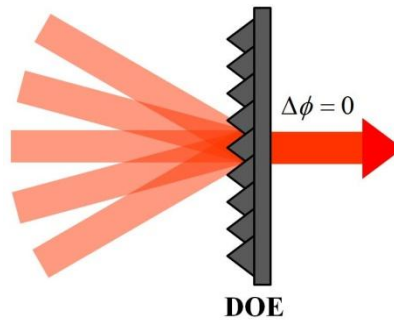
Figure 12: General representation of a Diffractive Optical Element (DOE) beam combiner. When the relative phase difference between each beam incident on the DOE is zero a single output beam will emerge.

Possibly the most dominate endorsers of the DOE beam combination technique are a high power fiber team with Northrop Grumman [22,23,50]. In 2008 said team published the results of a low power beam combination demonstration that coherently combined five spatially separate milli-watt class beams, via a DOE of their design, into a single beam with 91% efficiency [22]. The authors of said demonstration had theoretically predicted a slightly more efficient result, approximately 96%, and were able to determine the sources responsible for the ~5% reduction in efficiency [22]. As it turns out ~2% of said reduction is due to phase control (~λ/30 RMS), beam size (6 - 9% mismatch in beam waists), and alignment errors with the remaining ~3% originating from imperfect beam qualities, when compared to the diffraction limit, of the individual input beams [22]. Regardless of the reasons, 91% efficiency is an excellent result and should in no way be disregarded. The question that still needs to be answered is how well said beam combiner behaves when operated at much higher powers and is the topic of currently ongoing research.

2.4.4 Summary of Beam Combination Techniques

	Tiled Arrays	Polarization Beam Combiner	Diffractive Optical Element Beam
Output:	Multiple Beams	Single Beam	Single Beam
Method of Combination:	Beam overlap in Far Field	Overlapping beams with orthogonal polarizations	Overlapping/Interfering beams with common polarizations
# Beams Combined:	48	7	5
Scalable to High Chl. Counts?	YES	NO (can be very lossy)	YES
Thermal Load On Final Optic(s) (For high power apps)	LOW	HIGH	HIGH

Table 2: Comparison of Tiled Arrays, Polarization, and Diffractive Optical Element methods of beam combination.

Shown in

Table 2 is a comparison between the three methods of optical beam combination described above. Again, it is impossible to declare one method superior to the others as each technique has its own strengths and weaknesses. If the biggest concern is keeping the thermal load on the final optic(s) low then tiled arrays may be the way to go as the full power of the system is distributed over may array sub-apertures. If an application requires only a few beams to be combined into a single beam then the polarization beam combination technique might be the easiest to implement though the user will have to consider Fresnel and absorption losses in the polarizing optics. When trying to efficiently combine a large number of high power beams into a single output the diffractive optical element shows the most promise but the thermal load on the final optic (the DOE) may be an issue.

2.5. Including a Remote Object in the Feedback Loop
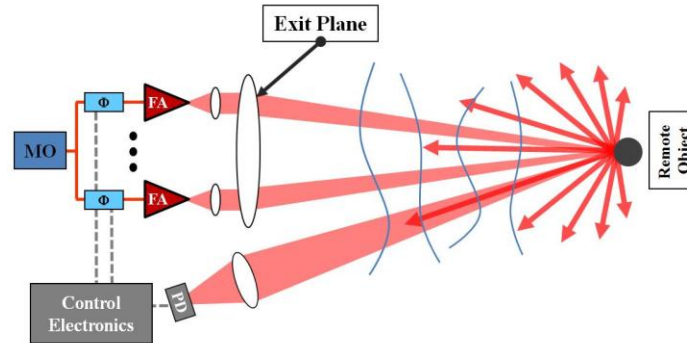
Figure 13: General Object In the Loop (OIL), tiled array, beam combination setup. Light scattered off of the illuminated object utilized as the return signal feeding the phase locking control electronics.

Each beam combination method discussed thus far has been confined to beam optimization at the exit aperture of the coherent beam combination system, *known as local loop phase locking*, with the unspoken assumption that the output would remain optimized for combination at some other remote point in space. This assumption holds true for methods that combine multiple beams into a single output, assuming said combined beam does not experience any higher order spatial phase aberrations across the profile of the combined output, or for tiled arrays operating in turbulence free conditions. In practice it is usually unreasonable to assume, even under calm laboratory conditions, that there will be no spatial phase disturbances acting on a tiled array of propagating beams before combination in the far field. This is due to the fact that each beam will individually experience unique low order phase aberrations (predominantly piston phase changes) when propagating in spatially different atmosphere than the other beams in the system (i.e. not following a common path to the remote object). Such piston phase aberrations will affect the beam in a similar manner as heat or mechanical disturbances affect a beams phase state when guided in a fiber, via a uniform phase retardation relative

to all other beams in the array. Therefore, when the output of a tiled array is optimized at the exit plane, in a local loop configuration, there are no guarantees that the combined beam will be, or remain, optimized on the remote object in the far field in the presence of atmospheric turbulence. We must therefore employ a technique for correcting for such disturbances.

Enter the *Object In the Loop (OIL)* phase locking configuration, shown in Figure 13, which, instead of locally sampling the beams to be combined, utilizes light scattered off of an illuminated object as the optical return signal needed for phase locking [27,45,51,52,53,54,55,56]. In general, single detector phase locking systems such as SPGD [27,45] and LOCSET [51,52,53,54,55,56], described above, are capable of operating in an OIL configuration as their basic operation, error metric optimizations previously discussed, is unaffected by the configuration change for reasons discussed in the following text.

In general, OIL beam combination configurations, shown in Figure 13, start with a single master oscillator (MO), the output of which is coupled into a single fiber patch cable and then split into N individual fiber channels for later combination in the far field. The light in each fiber channel is phase controlled via phase modulators providing the control electronics piston phase control of each of the N beams. The light in each of the N channels is then optically amplified and launched from a tiled array of individual, spatially separate, array sub-apertures. Unlike the previous discussion on tiled arrays the light from the array is not sampled via a partial reflector before propagating to the far field. Instead the light is simply allowed to propagate to the remote object with each beam in the array output experiencing unique optical phase disturbances due to

atmospheric effects. Each beam is then incident on a remote object in the far field where a percentage of the light, that which is not absorbed or misses that remote object all together, is scattered in many directions, some of which is directed back in the general direction of the array launch optics. In the same plane as the array launch optics is a spatially separate collection aperture consisting of a single lens and photodetector, drawn just below the launch optics in Figure 13. Said collection aperture collects a fraction of the light scattered from the remote object and focuses it onto a photodetector. The signal from the photodetector is then utilized by the LOCSET control electronics to apply the appropriate piston phase corrections to each array sub-aperture to minimize the optical phase difference between all beams in the array at the photodetector. Because the light from each array sub-aperture, scattering off of the remote object and collected at the collection aperture, follows a common 'return' path (i.e. perfectly overlapped) any phase disturbances introduced to the collected light while propagating along the return path will be common and therefore not change the difference in phase between each beam as measured at the remote object. Therefore, by minimizing the optical phase difference between each beam in the system at the collection aperture in the plane of the tiled array the beams will be coherently optimized at the remote object [27,45,51,52,53,54,55,56]!

2.5.1 Common Launch and Collection Path OIL Phase Locking
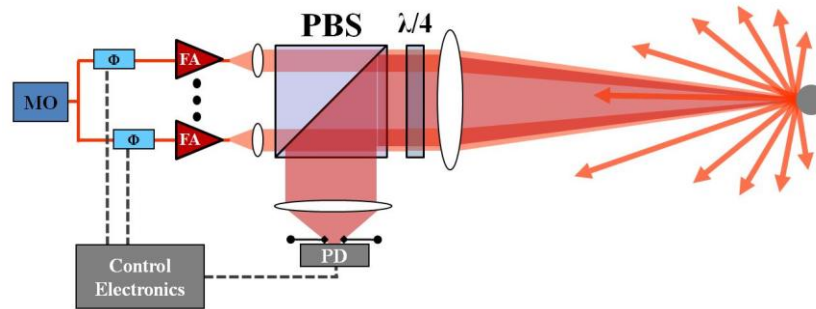
Figure 14: Shared launch and return path collection aperture Object In the Loop (OIL) phase locking [54,55,56].

Utilizing a spatially separate return path for OIL phase locking is not a necessary requirement but it does reduce system complexity and mitigate unwanted problems. In 2008 Dr. Pierre Bourdon and team demonstrated OIL phase locking in a configuration that dual purposed the array launch aperture as a return light collection aperture as shown in Figure 14 [54,55,56]. Said system begins with a single master oscillator (MO), the output of which is split into N piston phase controllable beams. Said beams are then amplified, collimated, and launched though a polarization beam splitting optic. Each linear polarized beam is then converted into a circular polarized beam via a quarter wave plate (λ/4) and allowed to propagate, through atmospheric turbulence, to a remote object in the far field [54,55,56]. A fraction of the light incident on the remote object is then scattered into a large solid angle, a portion of which will propagate along the same path(s) as the launch beams. The optical return light, still circularly polarized though now in the opposite handedness as originally launched, is again incident on the quarter wave plate. Upon passing through the quarter wave plate the return light is converted back to a linear polarization but is now orthogonal to the light originally launched through the polarization beam splitting optic [54,55,56]. Because of its new polarization the return

light, when incident on the polarization beam splitting optic, is then reflected and focused onto a photodetector. The photodetector then feeds the control electronics where an error signal is generated via the LOCSET technique described above. Said error signal is then used to apply the appropriate phase corrections to minimize the optical phase difference between each beam in the tiled array as measured at the photodetector. Via the relationship previously discussed, because the array is phase locked at the photodetector it is also phase locked and optimized on the remote object.

Much credit is due to Dr. Veronique Jolivet and team for such an elegant and compact approach to tiled array Object In the Loop (OIL) beam combination [54,55,56] but said technique runs into one very important problem, at least when considered for high power applications. When utilizing a high power laser system it is generally assumed that the high power propagating beam(s) will generate a significant amount of back scatter due to the presence of aerosols and other particulates in the air. A very large fraction of such backscatter will follow back along the same path as the outgoing beam(s) and, to first order, maintain a common circular polarization state (though with a change in handedness due to the change in direction). Said back scatter will then be collected by the launch/return optics and end up incident on the photodetector feeding the phase control electronics. Also incident on the photodetector will be the desired return light scattered off of the remote object, the object the system is trying to phase lock to. It is therefore very likely that the photodetector will become saturated due to too much light or that the desired phase error signals will become lost in all the optical noise due to the interaction of the wanted and unwanted optical returns.

2.5.2 Separate Return Path OIL Phase Locking

As will be further discussed in Chapter 7 of this dissertation, this problem was easily overcome, with no loss in system performance, via this authors patent pending [51] invention of an OIL beam combination system that utilizes a separate return path for the scattered return light. Because the optical path of the return light is spatially separated from the high power launch beams its relatively insensitive to aerosol or particulate back scatter. Just how insensitive the system is to backscatter simply depends on how far removed the return light collection aperture is from the array launch optics.

2.6. Chapter Summary:

The intent of this chapter is to provide the reader with a general knowledge base regarding methods of active phase locking and coherent beam combination. This text began with a discussion on high power solid state slab lasers showing that, even though they currently reign supreme in total output power (for solid state beam combination systems), they may not be the best choice for many high power laser applications, especially when considering mobile platforms. The reader was then introduced to rare-earth doped fiber lasers/amplifiers with their relative simplicity and superior beam quality. Unfortunately fiber lasers face some difficult hurdles when operating at high powers, especially single mode amplifiers that currently max out around 500W, such as non-linear effects in the gain media. To overcome such power limitations methods of active phase locking and coherent beam combination are often employed and were introduced to the reader in the text above.

Chapter 3.   Theory and Operation of LOCSET

The previous chapters provided an overview of high power fiber laser technology, made the case for coherent combination of multiple fiber sources, and reviewed different methods of coherent beam combination. This chapter is intended to provide an overview and theoretical basis of the Air Force's **Locking of Optical Coherence via Single-detector Electronic-frequency Tagging (LOCSET)** technique of active phase locking of multiple fiber amplifier sources [33,34,35,36,37,38,39,40]. This technique was originally pioneered by Dr. Thomas Shay [41,42,43] and Mr. Jeff Baker and has been built upon and extended by this author to include the optical return signal from a remote object of interest in the control loop. Said technique is known as Object In the Loop (OIL) phase locking and, in turbulent scenarios, corrects for low order atmospheric distortions and optimizes a tiled array of beams onto the remote object of interest [51,52,53,57] and will be discussed in further detail in a later chapter. The focus of the text below is to provide a theoretical description, and discuss the practical implementation, of the LOCSET technique of active phase locking.

3.1. Fundamental LOCSET operation:

To make optimal use of the previously described methods of beam combination (tiled arrays, diffractive optical elements, and polarization beam combination techniques) a method of controlling the optical phase of multiple beams must be established. Without control of optical phase of individual beams beam combination performance is left to the erratic whims of potential phase disturbances such as thermal drift, optical path length differences, and mechanical vibrations acting, potentially independently, on each beam in

the system. This section will provide a general overview of how the LOCSET active

phase locking technique corrects for these phase disturbances.
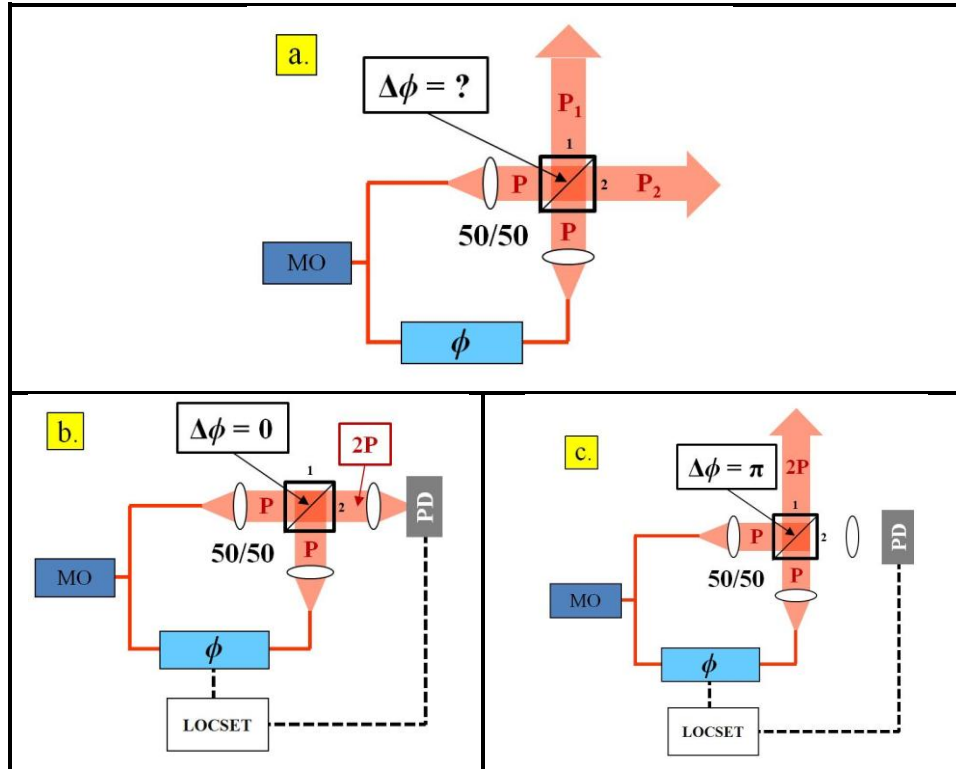
Figure 15: Basic 2 element coherent beam combination setup. a. No phase control. Phase of each beam left to drift in as dictated by their respective environments. b. Actively set phase difference, $\Delta\phi$, between the two beams to 0 at the beam splitter/combiner to establish constructive interference at photodetector. c. Actively set phase difference, $\Delta\phi$, to π at the beam splitter to establish destructive interference at photodetector.

3.1.1 Two Beam Combination: No Phase Control

Let's begin with the simplest case of 2 beam combination without a phase control

feedback system as shown in Figure 15a. Imagine that the system begins with a single

wavelength, infinitely narrow linewidth, master oscillator (MO). The output of the MO is

then split into two spatially separate beams. As drawn in Figure 15, splitting occurs

entirely in fiber. One beam has a phase controller/modulator that can be adjusted

arbitrarily. The other beam is allowed to drift in phase as its environment dictates. Each

beam is then collimated and incident on a 50/50 beam splitter/combiner where the beams

interfere with each other. Assuming both beams are identical in size, shape, optical power, polarization, and wavefront, they will interfere at the common surface of the beam splitter as is described by equation 3.1,

$$\frac{Int(\Delta\phi)}{Int_o} = 2(1+\cos(\Delta\phi)).$$

3.1

Here $Int(\Delta\phi)$ is the peak intensity of the combined beam, Int_o is the peak intensity of a single beam, and $\Delta\phi$ is the phase difference between the 2 beams. It is important to note that in this scenario equation 3.1 describes only the behavior at port 2 of the beam combiner shown in Figure 15 (to understand the behavior at port 1 simply add a $\pi/2$ phase shift to the cosine argument). Depending on the difference in phase, $\Delta\phi$, between the two beams at the beam splitter interface, the resulting combined output will either exit port 2 to the photodetector ($\Delta\phi = 0$), port 1 adjacent to the photodetector ($\Delta\phi = \pi$), or simply divide the power of the combined beam between port 1 and port 2 ($\Delta\phi \neq N\cdot\pi$, where N is an integer including 0). The system just described is essentially Mach-Zehnder interferometer found in virtually every fundamental principles of optics textbook such as *Optics* by Eugene Hecht [58] or *Optics* by Klein and Furtak [59].

Even though the setup shown in Figure 15a, and described above, is an interesting demonstration of 2 beam interference it isn't a very efficient or useful beam combination setup. This is primarily because the phase of each beam is essentially uncorrelated with the other (except for originating from a common source). An external phase disturbance acting on beam 1 won't necessarily act on beam 2 leading to an unknown distribution of the combined intensity between output beam 1 and 2 as is dictated by equation 3.1. This can be addressed using any of the active feedback loops described in Chapter 2, with

varying degrees of performance, but for the purposes of this discussion we will focus on the LOCSET phase locking technique [41,42,43].

3.1.2 Two Beam Combination: with LOCSET Active Phase Control

Now take a look at the same experimental setup but this time with the inclusion of a LOCSET active feedback loop to control the optical phase of just one beam, see Figure 15b and Figure 15c, leaving the other beam to drift in phase as dictated by environmental influences. Here the light from port 2 passes through a focusing lens and is incident on a photodetector. The electrical current from the photodetector is then processed by the LOCSET phase control electronics where an appropriate error signal is generated and applied to the phase modulator for final phase optimization. With the ability to control the optical phase difference at the surface of the beam splitter/combiner it is possible to force the two beams to interfere such that virtually all light will exit either port one or port two of the beam splitter/combiner simply by setting the phase condition, $\Delta\phi$, to 0 or π for constructive (Figure 15b) or destructive (Figure 15c) interference respectively (as measured with respect to the photodetector). With such a phase controller one now has the ability increase the total intensity delivered by the laser system by a factor of 2, for the setup described above, by coherently combining 2 light sources that share common optical properties.

Even though the discussion above was limited to 2 beams it isn't a difficult leap to think that combining many more beams together in a similar manner is possible. The following section will describe in detail how LOCSET generates an error signal when combining N coherent beams for the general case of $N \geq 2$.

3.2. Mathematical Description of LOCSET Operation
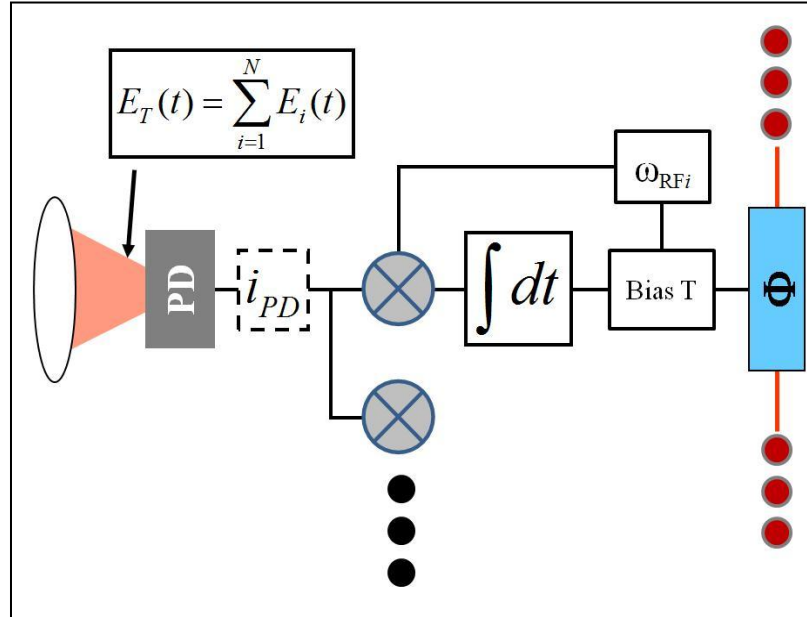
Figure 16: Basic LOCSET error signal processing diagram. System works from left to right. The phase modulated beams are combined and incident on the photodetector. The photocurrent is then mixed with a unique RF frequency and a phase error signal is generated via integration. The error signal and, RF phase dither, are then applied to a phase modulator keeping the ith beam in phase with all other beams. An identical control loop is applied to all N, or N-1, channels.

There are two operational configurations of LOCSET: self-referenced [37,38,40,41,42] and self-synchronous phase locking [33,34,35,36,39,43]. In self-referenced phase locking N-1 beams are tagged with a unique RF phase dither which is used to demodulate the phase difference of a single beam with respect to all other beams in the system. The remaining un-modulated beam's phase state is used as a reference for each of the RF phase modulated beams to 'track' and coherently combine to by minimizing the phase difference between each phase modulated beam and the un-modulated reference beam. It is important to note however that this reference beam is not required for successful LOCSET operation [33,34,35,36,39,43]. As will be shown below, if we set the amplitude of the un-modulated reference beam to zero (thereby removing it from the system) the error single equation still holds and actually simplifies. This

technique is known as self-synchronous LOCSET [33,34,35,36,39,43] and works just as the name implies. Each channel of LOCSET determines the phase difference between itself and all other channels and applies the appropriate phase correction. Because each channel is working towards minimizing the phase difference between itself and all other beams the phase difference between the beams will converge to 0, and establish optimal beam combination, as will be shown in the sections to follow.

The following text will walk through each fundamental step in the error signal process from the optical beams interfering at the photodetector to the final error signal applied to each of the N beams. Portions of the following derivations for the LOCSET error signals can also be found in the following references: 33, 34, 35, 36, 37, 38, 39, and 40.This is only intended to provide the reader with an understanding of LOCSET operation. What will not be revealed in the mathematics, and will be discussed in the final sections of this chapter, is how to implement the LOCSET error signal in a real world beam combination system.

3.2.1 Field Equations

To begin our analysis of LOCSET operation we first need to define the electric field of each of the N beams, shown to the left in Figure 16, incident on a photodetector. As discussed above, in the self-referenced LOCSET configuration, there are N-1 phase modulated beams, $E_i(t)$, in the beam combination system and a single un-modulated reference beam, $E_u(t)$ described by equations 3.2 and 3.3 respectively,

$$E_u(t) = E_{uo} \cos\left(\omega_L t + \phi_u(t)\right),$$

3.2

$$E_i(t) = E_{io} \cos\left(\omega_L t + \phi_i(t) + \beta_i \sin(\omega_i t)\right).$$

3.3

Here E_{uo} and E_{io} are the field amplitudes of the un-modulated and phase modulated beams, ω_L is proportional to the shared frequency of the optical beams, t represents time, and $\phi_u(t)$ and $\phi_i(t)$ are the slowly time varying phase states of the un-modulated and phase modulated beams respectively. *Because $\phi_u(t)$ and $\phi_i(t)$ vary much more slowly than the optical frequency, and RF phase modulation frequencies to be defined momentarily, we will treat them as constants and remove their time dependence from future analysis.* For the phase modulated beams, $E_i(t)$, $\left(\beta_i \sin(\omega_i t)\right)$ represents an applied sinusoidal phase modulation, or phase dither, with amplitude β_i and unique RF frequency ω_i. It is this unique RF frequency phase modulation that will later allow us to demodulate the phase error of the ith beam with respect to all other beams in the array.

Given that this is a beam combination effort the beams must somehow overlap at the photodetector shown in Figure 16. For simplicity we will assume all beams have common optical properties (i.e. frequency, linewidth, polarization state, etc.) and propagate along a common spatial path to the photodetector (i.e. perfect overlap). This

removes any angular and/or spatial separation between the individual beams and simplifies the math greatly. It is also important to note that the beam combination experiments discussed in later chapters of this dissertation operate in excellent agreement with these mathematical constraints. We can then write an expression for the combined electric field, $E_T(t)$ as shown in equation 3.4,

$$E_T(t) = E_u(t) + \sum_{i=1}^{N-1} E_i(t),$$
3.4

with the individual fields represented by equations 3.2 and 3.3 respectively.

3.2.2 Photocurrent

Now that we have an expression for the combined electric field we can proceed in defining the photocurrent $(i_{PD}(t))$, generated at the photodetector shown in Figure 16, that will be processed by the LOCSET electronics. Let's begin with the basic photocurrent equation 3.5 where R_{PD} is the responsivity of the photodetector, A is the active area of the photodetector, and *Int*(t) is the time varying intensity of the combined beams,

$$i_{PD}(t) = R_{PD} \cdot A \cdot Int(t).$$
3.5

We must next relate the combed electrical field to its measurable intensity which is proportional to the root of the ratio of the permittivity and permeability of free space multiplied by the square of the combined electric field,

$$Int(t) = \frac{1}{2} \cdot \left(\frac{\varepsilon_o}{\mu_o} \right)^{\frac{1}{2}} \cdot E_T^2(t).$$
3.6

Substituting equation 3.6 into equation 3.5 we get,

$$i_{PD}(t) = R_{PD} \cdot A \cdot \frac{1}{2} \cdot \left(\frac{\varepsilon_o}{\mu_o}\right)^{1/2} \cdot E_T^2(t).$$

3.7

Now that we have an expression relating the photodetector current to the combined electric field we can write a more complete expression of the photocurrent as shown in equation 3.8 where j and k are arbitrarily chosen summation indices,

$$i_{PD}(t) = R_{PD} \cdot A \cdot \frac{1}{2} \cdot \left(\frac{\varepsilon_o}{\mu_o}\right)^{1/2} \cdot \left(\begin{array}{c} E_u^2(t) + 2 \cdot E_u(t) \cdot \sum_{j=1}^{N-1} E_j(t) \\ + \left(\sum_{j=1}^{N-1} E_j(t)\right)\left(\sum_{k=1}^{N-1} E_k(t)\right) \end{array} \right).$$

3.8

It is informative to separate the photodetector current into 3 separate components: the photocurrent due to the presence of un-modulated reference beam, $i_u(t)$, the photocurrent due to the un-modulated reference beam interfering with each of the phase modulated beams, $i_{uj}(t)$, and the photocurrent due to the interference of each of the phase modulated beams with all remaining phase modulated beams $i_{jk}(t)$, as shown in equation 3.9,

$$i_{PD}(t) = i_u(t) + i_{uj}(t) + i_{jk}(t).$$

3.9

Each of these terms will be further defined in the following subsections.

3.2.2.1 Photocurrent: $i_u(t)$

$i_u(t)$ represents the component of the total photocurrent, $i_{PD}(t)$, that is influenced solely by presence of the un-modulated reference field, $E_u(t)$, and is shown below,

$$i_u(t) = R_{PD} \cdot A \cdot \frac{1}{2} \cdot \left(\frac{\varepsilon_o}{\mu_o}\right)^{\frac{1}{2}} \cdot E_u^2(t).$$

$$3.10$$

If we plug in the expression for the un-modulated field, equation 3.2, into equation 3.10 it becomes clear that the only time varying component of $i_u(t)$ are the oscillations governed by the frequency of the laser, as seen in equation 3.11,

$$i_u(t) = \frac{R_{PD} \cdot P_u}{2}\left(1 + \cos\left(2\omega_L t + 2\phi_u\right)\right).$$

$$3.11$$

Because the photodetector cannot follow optical frequency oscillations ($\sim 10^{14}$ Hz) it integrates, or time averages, those terms to zero $\left(\overline{\langle \cos(\omega_L \cdot t)\rangle}_t = 0\right)$ allowing us to neglect those terms and equation 3.11 simplifies to,

$$i_u(t) = \frac{R_{PD} \cdot P_u}{2}.$$

$$3.12$$

We find that the photocurrent, $i_u(t)$, is constant in time and proportional to the responsivity of the photodetector, R_{PD}, and the optical power of the un-modulated beam,

$$P_u = \frac{A \cdot E_{uo}^2}{2} \cdot \left(\frac{\varepsilon_o}{\mu_o}\right)^{\frac{1}{2}},$$

$$3.13$$

and therefore contributes only a DC bias to the total photocurrent.

3.2.2.2 Photocurrent Due to the Un-modulated Beam Interfering with each Phase Modulated Beam: $i_{uj}(t)$

$i_{uj}(t)$ represents the component of the total photocurrent, $i_{PD}(t)$, influenced only by the interference of the un-modulated reference beam with each of the RF phase modulated beams in the system and can be written as shown in equation 3.14,

$$i_{uj}(t) = \frac{R_{PD} \cdot A}{2} \cdot \left(\frac{\varepsilon_o}{\mu_o} \right)^{\frac{1}{2}} \cdot \left(2E_u(t) \cdot \sum_{j=1}^{N-1} E_j(t) \right). \qquad 3.14$$

If we plug in the expressions for the un-modulated, equation 3.2, and modulated electric fields, equation 3.3, into equation 3.14, utilize several trigonometric identities, and neglect the terms oscillating at the laser frequency we obtain equation 3.15,

$$i_{uj}(t) = R_{PD} \cdot P_u^{\frac{1}{2}} \sum_{j=1}^{N-1} P_j^{\frac{1}{2}} \cdot \left(\begin{array}{c} \cos(\phi_u - \phi_j)\cos(\beta_j \sin(\omega_j t)) \\ + \sin(\phi_u - \phi_j)\sin(\beta_j \sin(\omega_j t)) \end{array} \right). \qquad 3.15$$

It is informative to write equation 3.15 in a different form utilizing Fourier series expansions for the cosine, equation 3.16, and sine, equation 3.17, of $\left(\beta_j \sin(\omega_j t) \right)$ terms as shown in equation 3.18,

$$\cos(\beta_x \sin(\omega_x t)) = J_o(\beta_x) + 2\sum_{n=1}^{\infty} J_{2n}(\beta_x) \cdot \cos(2n \cdot \omega_x t), \qquad 3.16$$

$$\sin(\beta_x \sin(\omega_x t)) = 2\sum_{n=1}^{\infty} J_{2n-1}(\beta_x) \cdot \sin((2n-1) \cdot \omega_x t), \qquad 3.17$$

$$i_{uj}(t) = R_{PD} \cdot P_u^{\frac{1}{2}} \sum_{j=1}^{N-1} P_j^{\frac{1}{2}} \left(\begin{array}{c} \cos(\phi_u - \phi_j)\left(J_o(\beta_j) + 2\sum_{n=1}^{\infty} J_{2n}(\beta_j) \cdot \cos(2n \cdot \omega_j t) \right) \\ + \sin(\phi_u - \phi_j)\left(2\sum_{n=1}^{\infty} J_{2n-1}(\beta_j) \cdot \sin((2n-1) \cdot \omega_j t) \right) \end{array} \right). \qquad 3.18$$

Notice that the second term of the sum in equation 3.18, is proportional to the sine of the

phase difference between the un-modulated beam and the jth phase modulated beam,

$\left(\sin\left(\phi_u - \phi_j\right)\right)$, which has the proper characteristics of an error signal. When the phase

difference between the un-modulated beam and the jth modulated beam is zero the sine of

the phase difference, $\left(\sin\left(\phi_u - \phi_j\right)\right)$, is also zero and combination of the two beams is

optimized. When the phase difference does not equal zero, and changes sign (varies about

0), the $\left(\sin\left(\phi_u - \phi_j\right)\right)$ term will also change sign and is therefore a convenient error signal

for the LOCSET control circuit.

3.2.2.3 Photocurrent Due To All Phase Modulated Beams Interfering with Each Other: $i_{jk}(t)$

$i_{jk}(t)$ represents the component of the total photocurrent, $i_{PD}(t)$, governed by the

interference of each phase modulated beam with all other phase modulated beams in the

system and can be written as seen in equation 3.19,

$$i_{jk}\left(t\right) = \frac{R_{PD} \cdot A}{2} \cdot \left(\frac{\varepsilon_o}{\mu_o}\right)^{1/2} \cdot \left(\sum_{\substack{j=1 \\ j \neq k}}^{N-1} E_j\left(t\right)\right)\left(\sum_{\substack{k=1 \\ k \neq j}}^{N-1} E_k\left(t\right)\right). \qquad 3.19$$

If we plug in the expression for the phase modulated electric fields, equation 3.3, into

equation 3.19, again utilizing several trigonometric identities, and neglecting the terms

influenced by laser frequency oscillations we obtain equation 3.20,

$$i_{jk}(t) = \frac{R_{PD}}{2} \sum_{k=1}^{N-1} P_k^{1/2} \sum_{j=1}^{N-1} P_j^{1/2} \begin{pmatrix} \left(\cos\left(\phi_k - \phi_j\right)\cos\left(\beta_k \sin\left(\omega_k t\right)\right)\cos\left(\beta_j \sin\left(\omega_j t\right)\right) \right) \\ -\left(\sin\left(\phi_k - \phi_j\right)\sin\left(\beta_k \sin\left(\omega_k t\right)\right)\cos\left(\beta_j \sin\left(\omega_j t\right)\right) \right) \\ +\left(\sin\left(\phi_k - \phi_j\right)\cos\left(\beta_k \sin\left(\omega_k t\right)\right)\sin\left(\beta_j \sin\left(\omega_j t\right)\right) \right) \\ +\left(\cos\left(\phi_k - \phi_j\right)\sin\left(\beta_k \sin\left(\omega_k t\right)\right)\sin\left(\beta_j \sin\left(\omega_j t\right)\right) \right) \end{pmatrix}. \qquad 3.20$$

Just as before, it is informative to write equation 3.20 utilizing Fourier series expansions

for the cosine and sine of $\left(\beta_j \sin\left(\omega_j t\right)\right)$ terms as shown in equation 3.21,

$$i_{jk}(t) = \frac{R_{PD}}{2} \sum_{k=1}^{N-1} P_k^{1/2} \sum_{j=1}^{N-1} P_j^{1/2} \begin{pmatrix} \begin{pmatrix} \left(\cos\left(\phi_k - \phi_j\right)\left(J_o\left(\beta_k\right) + 2\sum_{n_k=1}^{\infty} J_{2n_k}\left(\beta_k\right)\cdot\cos\left(2n_k \cdot \omega_k t\right) \right) \right) \\ \cdot\left(J_o\left(\beta_j\right) + 2\sum_{n_j=1}^{\infty} J_{2n_j}\left(\beta_j\right)\cdot\cos\left(2n_j \cdot \omega_j t\right) \right) \end{pmatrix} \\ -\begin{pmatrix} \left(\sin\left(\phi_k - \phi_j\right)\left(2\sum_{n_k=1}^{\infty} J_{2n_k-1}\left(\beta_k\right)\cdot\sin\left((2n_k-1)\cdot \omega_k t\right) \right) \right) \\ \cdot\left(J_o\left(\beta_j\right) + 2\sum_{n_j=1}^{\infty} J_{2n_j}\left(\beta_j\right)\cdot\cos\left(2n_j \cdot \omega_j t\right) \right) \end{pmatrix} \\ +\begin{pmatrix} \left(\sin\left(\phi_k - \phi_j\right)\left(J_o\left(\beta_k\right) + 2\sum_{n_k=1}^{\infty} J_{2n_k}\left(\beta_k\right)\cdot\cos\left(2n_k \cdot \omega_k t\right) \right) \right) \\ \cdot\left(2\sum_{n_j=1}^{\infty} J_{2n_j-1}\left(\beta_j\right)\cdot\sin\left((2n_j-1)\cdot \omega_j t\right) \right) \end{pmatrix} \\ +\begin{pmatrix} \left(\cos\left(\phi_k - \phi_j\right)\left(2\sum_{n_k=1}^{\infty} J_{2n_k-1}\left(\beta_k\right)\cdot\sin\left((2n_k-1)\cdot \omega_k t\right) \right) \right) \\ \cdot\left(2\sum_{n_j=1}^{\infty} J_{2n_j-1}\left(\beta_j\right)\cdot\sin\left((2n_j-1)\cdot \omega_j t\right) \right) \end{pmatrix} \end{pmatrix}. \qquad 3.21$$

Notice that two of the four terms in the double sum found in equation 3.21 are

proportional to the sine of the phase difference between the kth and the jth beams of the

system, $\left(\sin\left(\phi_k - \phi_j\right) \right)$. Just as before these terms have the properties for creating an error

signal in that they equal zero when the system is optimized and change sign as the sign of the phase difference changes.

3.2.3 Phase Error Demodulation

If we look back to Figure 16 we'll see that up to this point we have only defined the photocurrent output from the photodetector, $i_{PD}(t)$. The next step in the process is to demodulate the phase error signal for each of the N-1 phase modulated beams from the photodetector current, $i_{PD}(t)$. Schematically this is done via individual and independent control loops acting on each of the phase modulated channels. This discussion will focus only on a single LOCSET control channel with the expectation that each control loop is performing the same operations. The only difference between the LOCSET control channels are the unique demodulation frequencies used in generating their respective phase error signals.

As you will recall, each of the N-1 phase modulated beams is tagged with a RF phase dither of fixed amplitude, β_j, and unique RF frequency, ω_j. It is this final condition, that ω_j is unique, that makes it possible to isolate the phase error of a given beam (x) with respect to all others (j) via coherent demodulation in the RF domain. As shown in Figure 16 the sampled photocurrent is first multiplied by, or mixed with, an RF demodulation signal, $\left(\sin\left(\omega_c t\right)\right)$, and integrated over some time τ, shown in equation 3.22,

$$ S_x = \frac{1}{\tau}\int_0^\tau i_{PD}(t)\cdot\sin\left(\omega_c \cdot t\right)dt. \tag{3.22} $$

Here ω_c represents the control loop demodulation frequency of the xth LOCSET channel and S_x represents the phase error correction signal for the xth phase modulated beam. ω_c is

chosen to equal the frequency of the RF phase dither previously applied to the xth phase

modulated beam $\left(\beta_x \sin\left(\omega_x t\right) \right)$; therefore $\left(\omega_c = \omega_x \right)$. The integration time τ is chosen

such that the LOCSET control loop will successfully isolate the phase error of the xth

beam in the system, $\left(\tau \gg \dfrac{2\pi}{\left| \omega_j - \omega_k \right|} \right)$ for all j and k, as well as remain short enough for

the control loop to effectively cancel the phase disturbances of the system. The reasons

for the above choices will become clear in the analysis to follow.

To generate a final expression for the phase error signal of the LOCSET

electronics we must plug equation 3.9 into equation 3.22. In doing this it is useful to

separate the total phase error signal for the xth channel, S_x, into three components (S_u, S_{xu},

S_{xj}) relative to the three components of the photocurrent defined above (i_u, i_{uj}, i_{jk}), shown

in the following equation,

$$S_x = S_u + S_{xu} + S_{xj}.$$

<div align="right">3.23</div>

Here S_u is the component of the total phase error signal of the xth channel, S_x, governed

solely by the presence of the un-modulated beam at the photodetector. S_{xu} is the

component of the total phase error signal of the xth channel, S_x, governed entirely by the

interaction of the xth phase modulated beam with the un-modulated reference beam. S_{xj} is

the final component of the total phase error signal of the xth channel, S_x, governed by the

interaction of the xth phase modulated beam with all other phase modulated beams in the

beam combination system.

3.2.3.1 Phase Error Signal Component Due Solely to the Presence of the Un-modulated Beam: S_u

S_u , shown in equation 3.24, is the component of the total phase error signal introduced solely by the presence of the un-modulated reference beam at the photodetector and can be written as,

$$S_u = \frac{1}{\tau}\int_0^\tau i_u(t)\cdot\sin\left(\omega_x\cdot t\right)dt. \qquad 3.24$$

If we plug in the expression for the un-modulated photocurrent, equation 3.12, into equation 3.24 and perform the integration we find that, because there are no interference terms in i_u (t), S_u evaluates to near zero, as shown in the following equation,

$$S_u = \frac{R_{PD}\cdot P_u}{2\cdot\tau}\int_0^\tau \sin\left(\omega_x\cdot t\right)dt = \frac{R_{PD}\cdot P_u}{2}\left(\frac{1}{\omega_x\cdot\tau}-\frac{\cos\left(\omega_x\tau\right)}{\omega_x\cdot\tau}\right)\approx 0. \qquad 3.25$$

The result shown in equation 3.25 assumes of course that a suitable integration time is chosen, $\left(\tau\gg\dfrac{2\pi}{\left|\omega_j-\omega_k\right|}\right)$, insuring that the error signal component S_u does not significantly contribute to the overall phase error signal, S_x. Even if the stated condition on the integration time is not met, in practice, the LOCSET electronics are AC coupled and would filter out S_u as it is only a DC contribution to the total error, S_x. Said result follows our intuition that there should be no time varying contributions to the total phase error signal, S_x, due solely to the presences of a non-phase modulated beam as there are no differences in phase to be detected.

3.2.3.2 Phase Error Signal Component Due to the Interference of the xth Phase Modulated Beam with the Un-modulated Reference Beam: S$_{xu}$

Before we proceed with establishing an expression for the phase error signal due to the interaction of the xth phase modulated beam with the un-modulated reference beam, S$_{xu}$, we need to set an important operating condition. To minimize phase errors of the combined beam resulting from the RF phase dithers applied to each of the modulated beams we need to keep the amplitude of said dithers low. For the remainder of this discussion we will assume that the RF phase modulation amplitude for all beams, β_j, is on the order of 1/10th of a radian or approximately 1/60th of the wavelength of an optical beam $(\lambda/60)$. This isn't to imply that all β_j's are the same, just that they are all small valued and constant. It is also worth mentioning that said constraint on the RF phase dither amplitude, β, isn't implemented just to simplify the calculations to follow. When performing the experiments described in later chapters the RF phase dither amplitudes were kept at or near $\lambda/60$ peak to peak for every LOCSET channel.

To obtain an expression for S$_{xu}$ we begin by inserting the expression for i_{uj}(t), equation 3.18, into equation 3.26,

$$S_{xu} = \frac{1}{\tau} \int_{t}^{t+\tau} i_{uj}(t) \cdot \sin(\omega_x \cdot t) dt. \tag{3.26}$$

We will neglect Bessel Functions beyond the second order as they evaluate to near zero when β is small and can write equation 3.26 as shown in equation 3.27,

$$S_{xu} = \frac{R_{PD} \cdot P_u^{\frac{1}{2}}}{\tau} \sum_{j=1}^{N-1} P_j^{\frac{1}{2}} \left(\begin{array}{c} \cos(\phi_u - \phi_j) \cdot (\eta_1 + \eta_2) \\ + \sin(\phi_u - \phi_j) \cdot \eta_3 \end{array} \right). \tag{3.27}$$

where η_1, η_2, and η_3 are defined as follows,

$$\eta_1 = J_o\left(\beta_j\right) \cdot \int_0^\tau \sin\left(\omega_x t\right) dt \tag{3.28}$$

$$\eta_2 = 2 \cdot J_2\left(\beta_j\right) \cdot \int_0^\tau \cos\left(2 \cdot \omega_j t\right) \sin\left(\omega_x t\right) dt \tag{3.29}$$

$$\eta_3 = 2 \cdot J_1\left(\beta_j\right) \cdot \int_0^\tau \sin\left(\omega_j t\right) \sin\left(\omega_x t\right) dt \tag{3.30}$$

We will proceed to solve for S_{xu} by evaluating the integrals η_1, η_2, and η_3 of equation 3.27. As mentioned previously, for a viable phase error signal to emerge from S_{xu}, the demodulation frequency of the control loop, ω_c, is chosen to equal the unique RF phase dither frequency, ω_x, applied to the xth unique channel of the beam combination system. Regardless of what we choose the control loop demodulation frequency to be we must consider two separate cases when solving the integrals in equation 3.27: first, the error signal when the demodulation frequency is equal to the RF phase dither frequency of the channel in question, $\left(S_{xu}\big|_{\omega_x=\omega_j}\right)$, and second, the error signal when the demodulation frequency is not equal to the RF phase dither of the channel in question, $\left(S_{xu}\big|_{\omega_x\neq\omega_j}\right)$. The two cases then sum together to form the final error signal pertaining to the interaction of the xth phase modulated beam interacting with the un-modulated reference beam as shown in the following equation,

$$S_{xu} = S_{xu}\big|_{\omega_x=\omega_j} + S_{xu}\big|_{\omega_x\neq\omega_j} \tag{3.31}$$

The goal here is to show that the value of S_{xu} increases as the integration time τ increases only when $\omega_x = \omega_j$, $\left(S_{xu}\big|_{\omega_x=\omega_j}\right)$, and remains significantly lower when $\omega_x \neq \omega_j$, $\left(S_{xu}\big|_{\omega_x\neq\omega_j}\right)$.

Determine: $S_{xu}\big|_{\omega_x=\omega_j}$

To begin let's first solve for η_1 of equation 3.27 for the case where $\omega_x = \omega_j$,

$$\eta_1\big|_{\omega_x=\omega_j} = J_o(\beta_j)\cdot\left(\frac{1}{\omega_x} - \frac{\cos(\omega_x\tau)}{\omega_x}\right). \qquad 3.32$$

Notice that equation 3.32 is simply the component of the error signal $S_{xu}\big|_{\omega_x=\omega_j}$ due solely

to the interaction of the demodulation signal with the slowly varying optical phase

difference between the un-modulated beam and the xth phase modulated beam (remember

that the solution in equation 3.32 is multiplied by $\cos(\phi_u - \phi_x)$ in our original expression

for $S_{xu}\big|_{\omega_x=\omega_j}$, equation 3.27). For large ω_x, $\left(\frac{1}{\omega_x} \approx 10^{-8}\,s\right)$, both terms to the right in

equation 3.32 will remain quite small regardless of the chosen integration time τ.

Next let's solve for η_2 in equation 3.27, for the case where $\omega_x = \omega_j$. The solution

to the integral found in equation 3.29 can be found in most any table of integrals [60] and

is shown in the following equation,

$$\eta_2\big|_{\omega_x=\omega_j} = 2\cdot J_2(\beta_j)\cdot\left(\frac{3\cdot\cos(\omega_x\tau)}{6\omega_x} - \frac{\cos(3\omega_x\tau)}{6\omega_x} - \frac{2}{6\omega_x}\right). \qquad 3.33$$

Notice that each of the 3 terms in equation 3.33, is proportional to $\left(\frac{1}{\omega_x}\right)$ and therefore

remains small $\left(\frac{1}{\omega_x} \approx 10^{-8}\,s\right)$ for RF frequencies regardless of the integration time as τ is

nestled inside cosine functions with maximum values of 1. The significance of this

determination will become evident later in this text.

Next we'll solve for η_3 of equation 3.27, as shown below, for the chase where $\omega_x = \omega_j$. The solution to the integral in η_3 is obtained by applying a standard trigonometric identity to the square of the sine term and performing the final integrations as outlined below,

$$\eta_3\big|_{\omega_x=\omega_j} = 2 \cdot J_1(\beta_j) \cdot \int_0^\tau \sin^2(\omega_x t) \, dt,$$

$$\int_0^\tau \sin^2(\omega_x t) \, dt = \frac{1}{2}\left(\int_0^\tau dt - \int_0^\tau \cos(2\omega_x t) \, dt \right), \qquad 3.34$$

$$\eta_3\big|_{\omega_x=\omega_j} = 2 \cdot J_1(\beta_j) \cdot \left(\frac{\tau}{2} - \frac{\sin(2\omega_x \tau)}{4\omega_x} \right).$$

Notice that the left most term in equation 3.34, highlighted in red, increases linearly as the integration time, τ, is increased and is independent of the RF demodulation frequency, ω_x, in stark contrast to the right most term that has an upper limit of $\left(\frac{1}{4\omega_x} \approx 2.5 \times 10^{-9} s \right)$ for a 100MHz demodulation frequency. For significantly long integration times, $\left(\tau \gg \frac{2\pi}{\omega_x} \right)$, the $\left(\frac{\tau}{2} \right)$ term easily dominates the right most term found in equations 3.34. The significance of this will also become evident later in this text.

Let's now plug the solutions for $\eta_1\big|_{\omega_x=\omega_j}$, $\eta_2\big|_{\omega_x=\omega_j}$, and $\eta_3\big|_{\omega_x=\omega_j}$ into our expression for the S_{xu} in equation 3.27,

$$S_{xu}\big|_{\omega_x=\omega_j} = \frac{R_{PD}\cdot P_u^{\frac{1}{2}}}{\tau}\cdot P_x^{\frac{1}{2}}\left(\begin{array}{c}\cos\left(\phi_u-\phi_x\right)\cdot J_o\left(\beta_x\right)\cdot\left(\dfrac{1}{\omega_x}-\dfrac{\cos\left(\omega_x\tau\right)}{\omega_x}\right)\\[2em]+\cos\left(\phi_u-\phi_x\right)\cdot 2\cdot J_2\left(\beta_x\right)\cdot\left(\begin{array}{c}\dfrac{3\cdot\cos\left(\omega_x\tau\right)}{6\omega_x}\\[1em]-\dfrac{\cos\left(3\omega_x\tau\right)}{6\omega_x}-\dfrac{2}{6\omega_x}\end{array}\right)\\[2em]+\sin\left(\phi_u-\phi_x\right)\cdot 2\cdot J_1\left(\beta_x\right)\cdot\left(\dfrac{\tau}{2}-\dfrac{\sin\left(2\omega_x\tau\right)}{4\omega_x}\right)\end{array}\right). \quad 3.35$$

For the time being we are only interested in the situation were $\omega_x = \omega_j$, and j is single valued, and have therefore dropped the summation in equation 3.35. The remainder of the j terms will be addressed in the discussion to follow regarding the situation were $\omega_x \neq \omega_j$ for all remaining values of j. Notice again in equation 3.35 that all but one term in the large parenthesis to the right are proportional to $\left(\dfrac{1}{\omega_x}\right)$. As discussed above, when compared to the single linear term, $\left(\dfrac{\tau}{2}\right)$, we realize that for significantly long integration times, $\left(\tau \gg \dfrac{2\pi}{\omega_x}\right)$, the $\left(\dfrac{\tau}{2}\right)$ term will be significantly greater valued than the rest, allowing us to eventually neglect terms proportional to $\left(\dfrac{1}{\omega_x}\right)$.

Determine: $S_{xu}\big|_{\omega_x \neq \omega_j}$

Just as for the special case of $\omega_x = \omega_j$ we must also solve the integrals in equation 3.27 for the case where $\omega_x \neq \omega_j$ for all remaining values of j, $\left(S_{xu}\big|_{\omega_x \neq \omega_j}\right)$. We'll begin by solving for η_1 in equation 3.27,

$$\eta_1\big|_{\omega_x \neq \omega_j} = J_o\left(\beta_j\right) \cdot \left(\frac{1}{\omega_x} - \frac{\cos\left(\omega_x \tau\right)}{\omega_x}\right). \qquad 3.36$$

Notice that the solution remained the same, as compared to in equation 3.32 for $\omega_x = \omega_j$, despite the new condition for ω_x. This is because equation 3.36 is in no way dependant on an RF optical phase change and is governed only by the interaction of the slowly varying phase difference between the jth phase modulated beam and the un-modulated reference beam. Just as before, for RF demodulation frequencies, both terms in equation 3.36 remain quite small regardless of the integration time τ.

Continuing on, we must next solve for η_2 of equation 3.27 for the case where $\omega_x \neq \omega_j$. Just as before, the solution to the integral in η_2 can be found in most any table of integrals [60] though this time the final result doesn't simplify as nicely as in equation 3.33,

$$\eta_2\big|_{\omega_x \neq \omega_j} = 2 \cdot J_2\left(\beta_j\right) \cdot \left(\begin{array}{c} \dfrac{\omega_x}{\omega_x^2 - 4\omega_j^2} \\[2ex] -\dfrac{\omega_x \cos\left(2\omega_j \tau\right)\cos\left(\omega_x \tau\right)}{\omega_x^2 - 4\omega_j^2} \\[2ex] -\dfrac{2\omega_j \sin\left(2\omega_j \tau\right)\sin\left(\omega_x \tau\right)}{\omega_x^2 - 4\omega_j^2} \end{array} \right). \qquad 3.37$$

Just as seen in the special case of $\omega_x = \omega_j$, each term in η_2 remains quite small for all values of integration time, τ, indicating that these terms will likely not play a significant role in the final error signal $S_{xu}\big|_{\omega_x \neq \omega_j}$.

The solution to the remaining integral found in η_3, for the case where $\omega_x \neq \omega_j$, can also be found in reference [60] and is provided below,

$$\eta_3\big|_{\omega_x \neq \omega_j} = 2 \cdot J_1(\beta_j) \cdot \left(\begin{array}{c} \dfrac{\omega_x \cos(\omega_x \tau) \sin(\omega_j \tau)}{\omega_j^2 - \omega_x^2} \\ - \dfrac{\omega_j \cos(\omega_j \tau) \sin(\omega_x \tau)}{\omega_j^2 - \omega_x^2} \end{array} \right). \qquad 3.38$$

It is important to note that the solution shown in equation 3.38 is only valid for $\omega_x \neq \omega_j$, and does not reduce to equation 3.34 when $\omega_x = \omega_j$. As ω_x approaches ω_j both denominators in equation 3.38 become very small and the result can approach infinity, depending on the integration time τ and just how close the two frequencies are. The result of equation 3.38 can be viewed as the most dominate LOCSET channel cross talk term and must be addressed. If the demodulation frequency of the xth LOCSET channel, ω_x, is too close in value to the RF phase dither frequency of another LOCSET channel, $(\omega_x \approx \omega_{j \neq x})$, then equation 3.38 will not necessary evaluate to near zero as required for the control loop to work. We must therefore set a new condition requiring the unique RF phase dither frequencies of each of the j channels of LOCSET control electronics be different enough so that the cross talk term in equation 3.38 will remain small regardless of the set integration time, τ, as shown below,

$$\tau \gg \frac{2\pi}{\left|\omega_x - \omega_{j \neq x}\right|},$$

3.39

where ω_x and $\omega_{j \neq x}$ are proportional to the two least separated RF phase dither frequencies used in the entire LOCSET coherent beam combination system. Equation 3.39 essentially dictates that the integration time of the xth LOCSET control loop be significantly longer than the period of the beat note between the two closest RF frequencies in the beam combination system.

Lets now plug the final solutions for $\eta_1\big|_{\omega_x \neq \omega_j}$, $\eta_2\big|_{\omega_x \neq \omega_j}$, and $\eta_3\big|_{\omega_x \neq \omega_j}$ into our error signal S_{xu}, equation 3.27, as shown in the following equation,

$$S_{xu}\big|_{\omega_x \neq \omega_j} = \frac{R_{PD} \cdot P_u^{1/2}}{\tau} \sum_{\substack{j=1 \\ j \neq x}}^{N-1} P_j^{1/2} \left(\begin{array}{l} \cos\left(\phi_u - \phi_j\right) \cdot J_o\left(\beta_j\right) \cdot \left(\dfrac{1}{\omega_x} - \dfrac{\cos\left(\omega_x \tau\right)}{\omega_x} \right) \\[2em] + \cos\left(\phi_u - \phi_j\right) \cdot 2 \cdot J_2\left(\beta_j\right) \cdot \left(\begin{array}{l} \dfrac{\omega_x}{\omega_x^2 - 4\omega_j^2} \\[1em] \dfrac{\omega_x \cos\left(2\omega_j \tau\right)\cos\left(\omega_x \tau\right)}{\omega_x^2 - 4\omega_j^2} \\[1em] - \dfrac{2\omega_j \sin\left(2\omega_j \tau\right)\sin\left(\omega_x \tau\right)}{\omega_x^2 - 4\omega_j^2} \end{array} \right) \\[4em] + \sin\left(\phi_u - \phi_j\right) \cdot 2 \cdot J_1\left(\beta_j\right) \cdot \left(\begin{array}{l} \dfrac{\omega_x \cos\left(\omega_x \tau\right)\sin\left(\omega_j \tau\right)}{\omega_j^2 - \omega_x^2} \\[1em] - \dfrac{\omega_j \cos\left(\omega_j \tau\right)\sin\left(\omega_x \tau\right)}{\omega_j^2 - \omega_x^2} \end{array} \right) \end{array} \right).$$

3.40

Notice, as discussed above, that each term in the sum proportional to $\left(\dfrac{1}{\omega_x}\right)$ or

$\left(\dfrac{\omega_{j,x}}{\omega_x^2 - 4\omega_j^2}\right)$ remains small regardless of the integration time as τ is nestled inside the

argument of sine or cosine functions with a maximum value of 1. If the integration time

condition stated in equation 3.39 is met the cross talk terms proportional to $\left(\dfrac{\omega_{j,x}}{\omega_j^2 - \omega_x^2}\right)$

will also remain quite small.

For completeness let's now write the entire expression for the phase error signal

dependant on the interaction of the xth phase modulated beam with the un-modulated

reference beam, S_{xu}, as shown below,

$$S_{xu} = S_{xu}\big|_{\omega_x = \omega_j} + S_{xu}\big|_{\omega_x \neq \omega_j} ,$$

$$S_{xu} = \frac{R_{PD} \cdot P_u^{1/2}}{\tau} \left| \begin{array}{c} P_x^{1/2} \left(\begin{array}{c} \cos(\phi_u - \phi_x) J_o(\beta_x) \cdot \left(\dfrac{1}{\omega_x} - \dfrac{\cos(\omega_x \tau)}{\omega_x} \right) \\[2ex] + \cos(\phi_u - \phi_x) 2 \cdot J_2(\beta_x) \cdot \left(\begin{array}{c} \dfrac{3 \cdot \cos(\omega_x \tau)}{6\omega_x} \\[2ex] -\dfrac{\cos(3\omega_x \tau)}{6\omega_x} - \dfrac{2}{6\omega_x} \end{array} \right) \\[3ex] + \sin(\phi_u - \phi_x) 2 \cdot J_1(\beta_x) \cdot \left(\dfrac{\tau}{2} - \dfrac{\sin(2\omega_x \tau)}{4\omega_x} \right) \end{array} \right) \\[10ex] + \sum_{\substack{j=1 \\ j \neq x}}^{N-1} P_j^{1/2} \left(\begin{array}{c} \cos(\phi_u - \phi_j) \cdot J_o(\beta_j) \cdot \left(\dfrac{1}{\omega_x} - \dfrac{\cos(\omega_x \tau)}{\omega_x} \right) \\[2ex] + \cos(\phi_u - \phi_j) \cdot 2 \cdot J_2(\beta_j) \cdot \left(\begin{array}{c} \dfrac{\omega_x}{\omega_x^2 - 4\omega_j^2} \\[2ex] -\dfrac{\omega_x \cos(2\omega_j \tau)\cos(\omega_x \tau)}{\omega_x^2 - 4\omega_j^2} \\[2ex] -\dfrac{2\omega_j \sin(2\omega_j \tau)\sin(\omega_x \tau)}{\omega_x^2 - 4\omega_j^2} \end{array} \right) \\[4ex] + \sin(\phi_u - \phi_j) \cdot 2 \cdot J_1(\beta_j) \cdot \left(\begin{array}{c} \dfrac{\omega_x \cos(\omega_x \tau)\sin(\omega_j \tau)}{\omega_j^2 - \omega_x^2} \\[2ex] -\dfrac{\omega_j \cos(\omega_j \tau)\sin(\omega_x \tau)}{\omega_j^2 - \omega_x^2} \end{array} \right) \end{array} \right) \end{array} \right| \qquad 3.41$$

As alluded to in previous sections of this chapter, the aim of this effort is to isolate the sine of the phase difference between the xth phase modulated beam and the un-modulated reference beam, $\left(\sin(\phi_u - \phi_j) \right)$, highlighted in orange in equation 3.41, as it maintains the proper characteristics of a control loop error signal. Notice that the un-highlighted terms to the right in equation 3.41 are proportional to either $\left(\dfrac{1}{\omega_x}, \dfrac{\omega_{j,x}}{\omega_j^2 - \omega_x^2}, or \dfrac{\omega_{j,x}}{\omega_x^2 - 4\omega_j^2} \right)$ and,

as discussed above, remain small valued regardless of the integration time, τ, assuming of course the condition stated in equation 3.39 is met. Now notice that the sole linear term in equation 3.41, highlighted in red, continually increases as the integration time is increased. Therefore, for significantly long integrations times, $\left(\tau \gg \dfrac{2\pi}{\left| \omega_x - \omega_{j \neq x} \right|} \right)$, the linear term highlighted in red in equation 3.41, will significantly dominate the un-highlighted terms, and equation 3.41 will simplify to,

$$S_{xu} = \frac{R_{PD} \cdot P_u^{\frac{1}{2}}}{\tau} P_x^{\frac{1}{2}} \cdot \left(2 \cdot J_1(\beta_x) \cdot \sin(\phi_u - \phi_x) \cdot \frac{\tau}{2} \right),$$

$$S_{xu} = R_{PD} \cdot P_u^{\frac{1}{2}} \cdot P_x^{\frac{1}{2}} \cdot J_1(\beta_x) \cdot \sin(\phi_u - \phi_x).$$

3.42

We see in equation 3.42, that our final expression for the error single, S_{xu}, is proportional to the sine of the phase difference between the un-modulated beam and the xth phase modulated beam. As stated before, the sine of the phase difference provides the LOCSET control electronics with an ideal error signal; when the phase difference between the two beams is zero, the error signal is also zero, and when the phase difference between the two beams is not equal to zero, and changes sign, the error signal also changes sign.

3.2.3.3 Phase Error Signal Component Due to the xth Phase Modulated Beam Interfering with All Other Phase Modulated Beams: S_{xj}

Our phase error analysis is not yet complete. There is still one phase error signal term that we have yet to account for; that of the interaction between the xth phase modulated beam with all other phase modulated beams $(j \neq x)$, S_{xj}. To begin our analysis we insert the expression for $i_{jk}(t)$ into the following equation for S_{xj}, and ignore Bessel functions beyond second order as they evaluate to near zero for small values of β,

$$S_{xj} = \frac{1}{\tau} \int_0^\tau i_{jk}(t) \cdot \sin(\omega_x \cdot t) dt,$$

$$S_{xj} = \frac{R_{PD}}{2\tau} \sum_{k=1}^{N-1} P_k^{1/2} \sum_{j=1}^{N-1} P_j^{1/2} \begin{pmatrix} \cos(\phi_k - \phi_j)(\gamma_1 + \gamma_2 + \gamma_3 + \gamma_4) \\ -\sin(\phi_k - \phi_j)(\gamma_5 + \gamma_6) \\ +\sin(\phi_k - \phi_j)(\gamma_7 + \gamma_8) \\ +\cos(\phi_k - \phi_j)(\gamma_9) \end{pmatrix}, \qquad 3.43$$

where $\gamma_1 - \gamma_9$ are defined as follows,

$$\gamma_1 = J_o(\beta_k) \cdot J_o(\beta_j) \int_0^\tau \sin(\omega_x t) dt, \qquad 3.44$$

$$\gamma_2 = 2 \cdot J_o(\beta_k) \cdot J_2(\beta_j) \int_0^\tau \cos(2\omega_j t) \sin(\omega_x t) dt, \qquad 3.45$$

$$\gamma_3 = 2 \cdot J_o(\beta_j) \cdot J_2(\beta_k) \int_0^\tau \cos(2\omega_k t) \sin(\omega_x t) dt, \qquad 3.46$$

$$\gamma_4 = 4 \cdot J_2(\beta_k) \cdot J_2(\beta_j) \int_0^\tau \cos(2\omega_j t) \cos(2\omega_k t) \sin(\omega_x t) dt, \qquad 3.47$$

$$\gamma_5 = 2 \cdot J_o(\beta_j) \cdot J_1(\beta_k) \int_0^\tau \sin(\omega_k t) \sin(\omega_x t) dt, \qquad 3.48$$

$$\gamma_6 = 4 \cdot J_1(\beta_k) \cdot J_2(\beta_j) \int_0^\tau \sin(\omega_k t) \cos(2\omega_j t) \sin(\omega_x t) dt, \qquad 3.49$$

$$\gamma_7 = 2 \cdot J_o(\beta_k) \cdot J_1(\beta_j) \int_0^\tau \sin(\omega_j t) \sin(\omega_x t) dt, \qquad 3.50$$

$$\gamma_8 = 4 \cdot J_1(\beta_j) \cdot J_2(\beta_k) \int_0^\tau \cos(2\omega_k t) \sin(\omega_j t) \sin(\omega_x t) dt, \qquad 3.51$$

$$\gamma_9 = 4 \cdot J_1(\beta_k) \cdot J_1(\beta_j) \int_0^\tau \sin(\omega_k t) \sin(\omega_j t) \sin(\omega_x t) dt. \qquad 3.52$$

It is clear that S_{xj} is a very complex function due to the matrix of optical beam interactions involved. In the text to follow we will isolate the expression for each γ term above and work to make some sense out of the apparent chaos. In the end, after the discussion to follow, this author will develop with a simple expression for the phase error term, S_{xj}, governed by the interactions of the xth phase modulated beam with all other phase modulated beams in the system.

$$\textbf{Determine: } S_{xj}\Big|_{\omega_x=\omega_j}$$

Let's now solve the integrals found in equations 3.44 through 3.52 for the demodulation condition: $\omega_x = \omega_j$. Initial examination of these integrals indicate that $\gamma_1\big|_{\omega_x=\omega_j}$ will be the most dominate term in the error signal, $S_{xj}\big|_{\omega_x=\omega_j}$, as the argument of the integral becomes $\left(\sin^2(\omega_x t)\right)$ and remains positive for all time indicating that for increasing integration times $\gamma_1\big|_{\omega_x=\omega_j}$ will also increase. Because the remaining γ terms listed above oscillate about zero when $\omega_x = \omega_j$ we expect those terms to remain small for increasing integration times. This is clearly shown by evaluating the integrals in each γ term defined above for $\omega_x = \omega_j$,

$$\gamma_1\big|_{\omega_x=\omega_j} = J_o(\beta_k) \cdot J_o(\beta_j)\left(\frac{1}{\omega_x} - \frac{\cos(\omega_x\tau)}{\omega_x}\right), \qquad\qquad 3.53$$

$$\gamma_2\big|_{\omega_x=\omega_j} = 2 \cdot J_o(\beta_k) \cdot J_2(\beta_x)\left(\frac{3\cos(\omega_x\tau)}{6\omega_x} - \frac{\cos(3\omega_x\tau)}{6\omega_x} - \frac{2}{6\omega_x}\right), \qquad\qquad 3.54$$

$$\gamma_3\big|_{\omega_x=\omega_j} = 2\cdot J_o(\beta_x)\cdot J_2(\beta_k)\left(\begin{array}{c} \dfrac{\omega_x}{\omega_x^2-4\omega_k^2} \\[3mm] -\dfrac{\omega_x\cos(2\omega_k\tau)\cos(\omega_x\tau)}{\omega_x^2-4\omega_k^2} \\[3mm] -\dfrac{2\omega_k\sin(2\omega_k\tau)\sin(\omega_x\tau)}{\omega_x^2-4\omega_k^2} \end{array}\right), \qquad 3.55$$

$$\gamma_4\big|_{\omega_x=\omega_j} = J_2(\beta_k)\cdot J_2(\beta_x)\left(\begin{array}{c} \dfrac{1}{2\omega_k-\omega_x}-\dfrac{1}{2\omega_k+\omega_x}-\dfrac{1}{2\omega_k-3\omega_x}+\dfrac{1}{2\omega_k+3\omega_x} \\[3mm] +\dfrac{\cos((2\omega_k-3\omega_x)\tau)}{2\omega_k-3\omega_x}-\dfrac{\cos((2\omega_k-\omega_x)\tau)}{2\omega_k-\omega_x} \\[3mm] +\dfrac{\cos((2\omega_k+\omega_x)\tau)}{2\omega_k+\omega_x}-\dfrac{\cos((2\omega_k+3\omega_x)\tau)}{2\omega_k+3\omega_x} \end{array}\right), \qquad 3.56$$

$$\gamma_5\big|_{\omega_x=\omega_j} = 2\cdot J_o(\beta_x)\cdot J_1(\beta_k)\left(\dfrac{\omega_x\cos(\omega_x\tau)\sin(\omega_k\tau)}{\omega_k^2-\omega_x^2}-\dfrac{\omega_k\cos(\omega_k\tau)\sin(\omega_x\tau)}{\omega_k^2-\omega_x^2}\right), \qquad 3.57$$

$$\gamma_6\big|_{\omega_x=\omega_j} = J_1(\beta_k)\cdot J_2(\beta_x)\left(\begin{array}{c} \dfrac{\sin((\omega_k-3\omega_x)\tau)}{\omega_k-3\omega_x}-\dfrac{\sin((\omega_k-\omega_x)\tau)}{\omega_k-\omega_x} \\[3mm] +\dfrac{\sin((\omega_k+\omega_x)\tau)}{\omega_k+\omega_x}-\dfrac{\sin((\omega_k+3\omega_x)\tau)}{\omega_k+3\omega_x} \end{array}\right), \qquad 3.58$$

$$\gamma_7\big|_{\omega_x=\omega_j} = 2\cdot J_o(\beta_k)\cdot J_1(\beta_x)\left(\dfrac{\tau}{2}-\dfrac{\sin(2\omega_x\tau)}{4\omega_x}\right), \qquad 3.59$$

$$\gamma_8\big|_{\omega_x=\omega_j} = \dfrac{1}{2}\cdot J_1(\beta_x)\cdot J_2(\beta_k)\left(\begin{array}{c} \dfrac{2\sin(2\omega_k\tau)}{\omega_k} \\[3mm] -\dfrac{\sin(2(\omega_k-\omega_x)\tau)}{\omega_k-\omega_x} \\[3mm] -\dfrac{\sin(2(\omega_k+\omega_x)\tau)}{\omega_k+\omega_x} \end{array}\right), \qquad 3.60$$

71

$$\gamma_9\big|_{\omega_x=\omega_j} = 4 \cdot J_1(\beta_k) \cdot J_1(\beta_x) \left(\begin{array}{c} \dfrac{\cos(\omega_k\tau)\left(4\omega_x^2 - \omega_k^2 + \omega_k^2\cos(2\omega_x\tau)\right)}{2\left(\omega_k^3 - 4\omega_k\omega_x^2\right)} \\ + \dfrac{2\omega_x\left(\omega_k\sin(\omega_k\tau)\sin(2\omega_x\tau) - 2\omega_x\right)}{2\left(\omega_k^3 - 4\omega_k\omega_x^2\right)} \end{array} \right).$$

3.61

Assuming that ω_x is significantly different than ω_k in the expressions above, or that the

integration time is significantly longer than $\left(\dfrac{2\pi}{|\omega_x - \omega_k|}\right)$, for the condition of $\omega_x = \omega_j$,

there is only one term that continually increases for increasing integration times τ, the left

most term in γ_7, highlighted in red. Therefore, for significantly large integration times the

left most term in γ_7 dominates all other terms above and equation 3.43, for $\omega_x = \omega_j$,

simplifies to,

$$S_{xj}\big|_{\omega_x=\omega_j} = \frac{R_{PD}}{2} P_x^{1/2} \cdot J_1(\beta_x) \cdot \sum_{\substack{j=1 \\ j \neq x}}^{N-1} P_j^{1/2} J_o(\beta_j) \cdot \sin(\phi_j - \phi_x).$$

3.62

(Note that the summation index in equation 3.62 was reverted from k back to j) Here we

see that the phase error signal $\left(S_{xj}\big|_{\omega_x=\omega_j}\right)$ is proportional to the sum of the sine of the phase

difference between x^{th} phase modulated beam and the jth phase modulated beams for all

values of k and, just as before, has the proper form of an electronic control loop error

signal.

Determine: $S_{xj}\big|_{\omega_x \neq \omega_j}$

We must consider one final case in obtaining the value of the error signal, S_{xj}, that

when $\omega_x \neq \omega_j$, $\left(S_{xj}\big|_{\omega_x \neq \omega_j}\right)$. The initial expression for $\left(S_{xj}\big|_{\omega_x \neq \omega_j}\right)$ remains the same as seen

in equation 3.43, including all integrals defined in equations 3.44 through 3.52. Let's now

solve the integrals found in equations 3.44 through 3.52 for the case where $\omega_x \neq \omega_j$. The

solutions to these expressions are shown below,

$$\gamma_1\big|_{\omega_x \neq \omega_j} = J_o(\beta_k) \cdot J_o(\beta_j) \left(\frac{1}{\omega_x} - \frac{\cos(\omega_x \tau)}{\omega_x} \right), \tag{3.63}$$

$$\gamma_2\big|_{\omega_x \neq \omega_j} = 2 \cdot J_o(\beta_k) \cdot J_2(\beta_j) \left(\begin{array}{c} \dfrac{\omega_x}{\omega_x^2 - 4\omega_j^2} \\[3mm] -\dfrac{\omega_x \cos(2\omega_j \tau)\cos(\omega_x \tau)}{\omega_x^2 - 4\omega_j^2} \\[3mm] -\dfrac{2\omega_j \sin(2\omega_j \tau)\sin(\omega_x \tau)}{\omega_x^2 - 4\omega_j^2} \end{array} \right), \tag{3.64}$$

$$\gamma_3\big|_{\omega_x \neq \omega_j} = 2 \cdot J_o(\beta_j) \cdot J_2(\beta_k) \left(\begin{array}{c} \dfrac{\omega_x}{\omega_x^2 - 4\omega_k^2} \\[3mm] -\dfrac{\omega_x \cos(2\omega_k \tau)\cos(\omega_x \tau)}{\omega_x^2 - 4\omega_j^2} \\[3mm] -\dfrac{2\omega_k \sin(2\omega_k \tau)\sin(\omega_x \tau)}{\omega_x^2 - 4\omega_j^2} \end{array} \right), \tag{3.65}$$

$$\gamma_4\big|_{\omega_x \neq \omega_j} = J_2(\beta_k) \cdot J_2(\beta_j) \begin{pmatrix} -\dfrac{1}{2\omega_j + 2\omega_k - \omega_x} \\[2mm] +\dfrac{1}{2\omega_j - 2\omega_k + \omega_x} \\[2mm] -\dfrac{1}{2\omega_j - 2\omega_k - \omega_x} \\[2mm] +\dfrac{1}{2\omega_j + 2\omega_k + \omega_x} \\[2mm] +\dfrac{\cos\big((2\omega_j + 2\omega_k - \omega_x)\tau\big)}{2\omega_j + 2\omega_k - \omega_x} \\[2mm] -\dfrac{\cos\big((2\omega_j - 2\omega_k + \omega_x)\tau\big)}{2\omega_j - 2\omega_k + \omega_x} \\[2mm] +\dfrac{\cos\big((2\omega_j - 2\omega_k - \omega_x)\tau\big)}{2\omega_j - 2\omega_k - \omega_x} \\[2mm] -\dfrac{\cos\big((2\omega_j + 2\omega_k + \omega_x)\tau\big)}{2\omega_j + 2\omega_k + \omega_x} \end{pmatrix}, \qquad 3.66$$

$$\gamma_5\big|_{\omega_x \neq \omega_j} = 2 \cdot J_o(\beta_j) \cdot J_1(\beta_k) \begin{pmatrix} \dfrac{\omega_x \cos(\omega_x\tau)\sin(\omega_k\tau)}{\omega_k^2 - \omega_x^2} \\[3mm] -\dfrac{\omega_k \cos(\omega_k\tau)\sin(\omega_x\tau)}{\omega_k^2 - \omega_x^2} \end{pmatrix}, \qquad 3.67$$

$$\gamma_6\big|_{\omega_x \neq \omega_j} = J_1(\beta_k) \cdot J_2(\beta_j) \begin{pmatrix} \dfrac{\sin\big((2\omega_j - \omega_k - \omega_x)\tau\big)}{-2\omega_j + \omega_k + \omega_x} \\[2mm] +\dfrac{\sin\big((2\omega_j + \omega_k - \omega_x)\tau\big)}{2\omega_j + \omega_k - \omega_x} \\[2mm] +\dfrac{\sin\big((2\omega_j - \omega_k + \omega_x)\tau\big)}{2\omega_j - \omega_k + \omega_x} \\[2mm] -\dfrac{\sin\big((2\omega_j + \omega_k + \omega_x)\tau\big)}{2\omega_j + \omega_k + \omega_x} \end{pmatrix}, \qquad 3.68$$

74

$$\gamma_7\big|_{\omega_x \neq \omega_j} = 2 \cdot J_o\left(\beta_k\right) \cdot J_1\left(\beta_j\right)\left(\begin{array}{c} \dfrac{\omega_x \cos\left(\omega_x \tau\right) \sin\left(\omega_j \tau\right)}{\omega_j^2 - \omega_x^2} \\[3mm] -\dfrac{\omega_j \cos\left(\omega_j \tau\right) \sin\left(\omega_x \tau\right)}{\omega_j^2 - \omega_x^2} \end{array} \right), \qquad 3.69$$

$$\gamma_8\big|_{\omega_x \neq \omega_j} = J_1\left(\beta_j\right) \cdot J_2\left(\beta_k\right)\left(\begin{array}{c} \dfrac{\sin\left(\left(\omega_j - 2\omega_k - \omega_x\right)\tau\right)}{\omega_j - 2\omega_k - \omega_x} \\[3mm] +\dfrac{\left(\sin\left(\omega_j + 2\omega_k - \omega_x\right)\tau\right)}{\omega_j + 2\omega_k - \omega_x} \\[3mm] -\dfrac{\sin\left(\left(\omega_j - 2\omega_k + \omega_x\right)\tau\right)}{\omega_j - 2\omega_k + \omega_x} \\[3mm] -\dfrac{\sin\left(\left(\omega_j + 2\omega_k + \omega_x\right)\tau\right)}{\omega_j + 2\omega_k + \omega_x} \end{array} \right), \qquad 3.70$$

$$\gamma_9\big|_{\omega_x \neq \omega_j} = J_1\left(\beta_k\right) \cdot J_1\left(\beta_j\right)\left(\begin{array}{c} \dfrac{1}{\omega_j + \omega_k - \omega_x} \\[3mm] +\dfrac{1}{\omega_j - \omega_k + \omega_x} \\[3mm] -\dfrac{1}{\omega_j - \omega_k - \omega_x} \\[3mm] -\dfrac{1}{\omega_j + \omega_k + \omega_x} \\[3mm] -\dfrac{\cos\left(\left(\omega_j + \omega_k - \omega_x\right)\tau\right)}{\omega_j + \omega_k - \omega_x} \\[3mm] -\dfrac{\cos\left(\left(\omega_j - \omega_k + \omega_x\right)\tau\right)}{\omega_j - \omega_k + \omega_x} \\[3mm] +\dfrac{\cos\left(\left(\omega_j - \omega_k - \omega_x\right)\tau\right)}{\omega_j - \omega_k - \omega_x} \\[3mm] +\dfrac{\cos\left(\left(\omega_j + \omega_k + \omega_x\right)\tau\right)}{\omega_j + \omega_k + \omega_x} \end{array} \right). \qquad 3.71$$

It is important to notice that each expression of $\gamma\big|_{\omega_x \neq \omega_j}$ in equations 3.63 through 3.71 are

nearly proportional to $\left(\dfrac{1}{\omega_i^x} \right)$, assuming that $\omega_x \approx \omega_j \approx \omega_k$, except for two, $\gamma_5\big|_{\omega_x \neq \omega_j}$ and

$\gamma_7\big|_{\omega_x \neq \omega_j}$, whose values increase as $(\omega_x \to \omega_j)$. Once again, if the integration time is

significantly long, $\left(\tau \gg \dfrac{2\pi}{|\omega_x - \omega_{j \neq x}|} \right)$, $\gamma_5\big|_{\omega_x \neq \omega_j}$ and $\gamma_7\big|_{\omega_x \neq \omega_j}$ too will remain significantly

smaller than the most dominate term, for the coherent demodulation case, evaluated in

equation 3.59, $\left(\dfrac{\tau}{2} \right)$. If said conditions are met than we can write the final expression for

the contribution to the total phase error signal governed by the interaction of the xth phase

modulated beam with all other phase modulated beams, S_{xj}, as seen below,

$$S_{xj} = S_{xj}\big|_{\omega_x = \omega_j} = R_{PD} P_x^{1/2} \cdot J_1(\beta_x) \cdot \frac{1}{2} \sum_{\substack{j=1 \\ j \neq x}}^{N-1} P_j^{1/2} J_o(\beta_j) \cdot \sin(\phi_j - \phi_x). \tag{3.72}$$

(Note again that the summation index in equation 3.72 was reverted from k back to j)

This is a very important result as S_{xj} adds to the robustness of the LOCSET phase locking

system. Unlike many other methods of phase locking, where the phase error signal

generated is governed only by the independent interaction of each phase controlled beam

with a common reference beam [3,4,20 ,21,23,24,32,61], LOCSET adds a measurement

proportional to the sum of the phase difference of each beam with respect to all other

beams in the system. If the reference beam where to somehow be lost, maybe via

amplifier failure or beam misalignment, the LOCSET system would continue to phase

lock the remaining beams whereas many other coherent beam combination methods

would fail entirely [3,4,20 ,21,23,24,32,61].

3.2.4 Self-Referenced LOCSET Phase Error Signal

Let's now bring each component of the total phase error together into a single representation of the Self-Reference LOCSET phase error signal. Beginning with the general expression for the phase error of the xth phase modulated beam with respect to all other beams in the system we have again equation 3.23,

$$S_x = S_u + S_{xu} + S_{xj}.$$

3.23

From our analysis of the phase error component governed only the presence of light from the un-modulated reference beam at the photodetector we can set S_u to zero. Plugging in the expressions for S_{xu}, equation 3.42, and S_{xj}, 3.72, we have the following final representation of the Self-Referenced LOCSET phase error correction signal for the xth control loop channel, S_{SRx}, shown in equation 3.73,

$$S_{SRx} = R_{PD} \cdot P_x^{\frac{1}{2}} \cdot J_1(\beta_x) \left(P_u^{\frac{1}{2}} \sin(\phi_u - \phi_x) + \frac{1}{2} \sum_{\substack{j=1 \\ j \neq x}}^{N-1} P_j^{\frac{1}{2}} \cdot J_o(\beta_j) \cdot \sin(\phi_j - \phi_x) \right).$$

3.73

It is important to note that the electronic phase error signal of a self-referenced phase locking system, S_{SRx}, changes only with the slow variations in the optical phase differences between combined beams. Of course this assumes that the optical power and phase modulation depth of the individual phase modulated beams remain relatively constant which, in practice, is generally a valid assumption. As long as the phase difference between each combined beam is zero the phase error, S_{SRx} is also zero. If the xth beam drifts out of phase with the rest of the system, the phase error signal for the xth beam will be nonzero and carry a sign (+/-) indicating the direction in phase it drifted

with respect to the other beams. An error correction signal is then applied to the xth beam's phase control device and the system returns towards optimal phase locking.

3.2.5 Self-Synchronous LOCSET Phase Error Signal

As previously stated, an un-modulated reference beam, though often implemented, is not necessary for LOCSET operation. Let's take a look again at the expression for the Self-Referenced LOCSET phase error signal, S_{SRx}, in equation 3.73. The only term in the expression that is influenced by the un-modulated reference beam is the first term inside the parenthesis $\left(P_u^{1/2} \sin \left(\phi_u - \phi_x \right) \right)$. By simply setting the optical power of the un-modulated reference beam to zero, essentially turning the reference beam off, we eliminate its contribution to the phase error signal, as shown in equation 3.74,

$$S_{SSx} = R_{PD} \cdot P_x^{1/2} \cdot J_1 \left(\beta_x \right) \frac{1}{2} \sum_{\substack{j=1 \\ j \neq x}}^{N-1} P_j^{1/2} \cdot J_o \left(\beta_j \right) \cdot \sin \left(\phi_j - \phi_x \right).$$

3.74

Operation without a reference beam is known as Self-Synchronous LOCSET and is denoted as S_{SSx}.

Operating without a common reference beam for each of the N-1 phase controlled channels is not intuitive for most of us. The reason LOCSET is capable of operating without a reference beam is because it measures the relative phase error of a single beam with respect to every other beam in the system. Because the phase information of a given beam is known with respect to all others the reference beam is no longer needed, as it is only a single element of the coherently combined beam.

3.2.6 Relative Strength of LOCSET Error Signal Terms (η and γ)

Before proceeding let's take a step back and revisit the complete solution to the

LOCSET error signal, S_x, for ideal and experimental conditions. For the purposes of this

discussion we will assume a four channel LOCSET coherent beam combination system

with an un-modulated reference beam and three RF phase modulated beams with unique

modulation frequencies, 99MHz, 100MHz and 101MHz respectively, and a common

modulation amplitude, $\beta = 0.1$ radians. We will also assume that the optical powers in

each beam are equal such that: $P_u = P_x = P_j = P_k = P$. Also in this discussion we will

utilize a demodulation frequency of 100MHz (i.e. we want to demodulate the phase error

of the channel with a 100MHz phase modulation with respect to the other channels in the

system). The goal here is to demonstrate which terms contribute most predominately to

the LOCSET phase error signal, S_x. We'll begin by re-writing our expression for S_x by

summing equations 3.27 and 3.43 together, as shown below,

$$
S_x = \frac{R_{PD} \cdot P}{\tau} \left(\begin{array}{l} \displaystyle\sum_{j=1}^{N-1} \left(\begin{array}{l} \cos\left(\phi_u - \phi_j\right)\cdot\left(\eta_1 + \eta_2\right) \\ + \sin\left(\phi_u - \phi_j\right)\cdot\eta_3 \end{array} \right) \\ + \displaystyle\sum_{k=1}^{N-1}\sum_{j=1}^{N-1} \left(\begin{array}{l} \cos\left(\phi_k - \phi_j\right)\left(\dfrac{\gamma_1}{2} + \dfrac{\gamma_2}{2} + \dfrac{\gamma_3}{2} + \dfrac{\gamma_4}{2}\right) \\ - \sin\left(\phi_k - \phi_j\right)\left(\dfrac{\gamma_5}{2} + \dfrac{\gamma_6}{2}\right) \\ + \sin\left(\phi_k - \phi_j\right)\left(\dfrac{\gamma_7}{2} + \dfrac{\gamma_8}{2}\right) \\ + \cos\left(\phi_k - \phi_j\right)\left(\dfrac{\gamma_9}{2}\right) \end{array} \right) \end{array} \right). \qquad 3.75
$$

Notice that the terms in equation 3.75 have been rearranged, from their original forms in

equations 3.27 and 3.43, such that the multiplicative factors before both summations are

the same. This allows us an apples to apples comparison of each η and γ term in equation 3.75 as shown in Table 3 for different integration times, τ.

In Table 3 it is important to notice the terms highlighted in blue, $\eta_3\big|_{\omega_x=\omega_j}$ and $\gamma_7\big|_{\omega_x=\omega_j}$, as they are the dominate error terms previously isolated in the discussions leading to the reduced form of the LOCSET error signal for both self-referenced and self-synchronous configurations shown in equations 3.73 and 3.74 respectively. To obtain those solutions we established a LOCSET operating condition requiring the electronic integration time of the xth LOCSET control loop be much greater than the interference beat note period between the two closest RF modulation frequencies in the entire beam combination system, $\left(\tau \gg \dfrac{2\pi}{\left|\omega_x - \omega_{j\neq x}\right|} \right)$. Under the conditions stated above this would require that the integration time τ be much greater than 1μs. For the moment let's assume that an integration time of 10.45μs is implemented in our LOCSET control system. We can then evaluate each term, η's and γ's, in equation 3.75 for the frequencies and phase modulation amplitudes defined above, to obtain the right most column in Table 3. Notice that the terms closest to the desired error signal term, $\eta_3\big|_{\omega_x=\omega_j}$, excluding $\gamma_7\big|_{\omega_x=\omega_j}$, has approximately $1/200^{th}$ the contribution as $\eta_3\big|_{\omega_x=\omega_j}$, and only $1/100^{th}$ the contribution of $\gamma_7\big|_{\omega_x=\omega_j}$. All other terms of the error signal, for a 10.45μs integration time, remain significantly smaller. Therefore, under the previously stated conditions, all assumptions leading to the reduced form LOCSET error signal expressions in equations 3.73 and 3.74 are well justified.

	$\tau = 2.45\,\mu s$	$\tau = 3.0\,\mu s$	$\tau = 10.45\,\mu s$
	experimental	ideal	example
	$\left\|\dfrac{\eta_i,\gamma_i}{\eta_3}\right\|_{\omega_x=\omega_j}$	$\left\|\dfrac{\eta_i,\gamma_i}{\eta_3}\right\|_{\omega_x=\omega_j}$	$\left\|\dfrac{\eta_i,\gamma_i}{\eta_3}\right\|_{\omega_x=\omega_j}$
$\eta_1\big\|_{\omega_x=\omega_j}$	$\sim \frac{1}{200}$	$\frac{1}{\infty}$	$\sim \frac{1}{850}$
$\eta_2\big\|_{\omega_x=\omega_j}$	$\sim \frac{1}{6\cdot10^3}$	$\frac{1}{\infty}$	$\sim \frac{1}{2.5\cdot10^4}$
$\eta_3\big\|_{\omega_x=\omega_j}$	$\frac{1}{1}$	$\frac{1}{1}$	$\frac{1}{1}$
$\eta_1\big\|_{\omega_x\neq\omega_j}$	$\sim \frac{1}{200}$	$\frac{1}{\infty}$	$\sim \frac{1}{850}$
$\eta_2\big\|_{\omega_x\neq\omega_j}$	$\sim \frac{1}{4\cdot10^3}$	$\frac{1}{\infty}$	$\sim \frac{1}{1\cdot10^4}$
$\eta_3\big\|_{\omega_x\neq\omega_j}$	$\sim \frac{1}{50}$	$\frac{1}{\infty}$	$\sim \frac{1}{200}$
$\frac{1}{2}\cdot\gamma_1\big\|_{\omega_x=\omega_j}$	$\sim \frac{1}{400}$	$\frac{1}{\infty}$	$\sim \frac{1}{2\cdot10^3}$
$\frac{1}{2}\cdot\gamma_2\big\|_{\omega_x=\omega_j}$	$\sim \frac{1}{5\cdot10^5}$	$\frac{1}{\infty}$	$\sim \frac{1}{2\cdot10^6}$
$\frac{1}{2}\cdot\gamma_3\big\|_{\omega_x=\omega_j}$	$\sim \frac{1}{4\cdot10^5}$	$\frac{1}{\infty}$	$\sim \frac{1}{2\cdot10^6}$
$\frac{1}{2}\cdot\gamma_4\big\|_{\omega_x=\omega_j}$	$\sim \frac{1}{2\cdot10^8}$	$\frac{1}{\infty}$	$\sim \frac{1}{9\cdot10^8}$
$\frac{1}{2}\cdot\gamma_5\big\|_{\omega_x=\omega_j}$	$\sim \frac{1}{100}$	$\frac{1}{\infty}$	$\sim \frac{1}{400}$
$\frac{1}{2}\cdot\gamma_6\big\|_{\omega_x=\omega_j}$	$\sim \frac{1}{8\cdot10^4}$	$\frac{1}{\infty}$	$\sim \frac{1}{3.5\cdot10^5}$
$\frac{1}{2}\cdot\gamma_7\big\|_{\omega_x=\omega_j}$	$\sim \frac{1}{2}$	$\sim \frac{1}{2}$	$\sim \frac{1}{2}$
$\frac{1}{2}\cdot\gamma_8\big\|_{\omega_x=\omega_j}$	$\sim \frac{1}{8\cdot10^4}$	$\frac{1}{\infty}$	$\sim \frac{1}{4\cdot10^5}$
$\frac{1}{2}\cdot\gamma_9\big\|_{\omega_x=\omega_j}$	$\sim \frac{1}{1\cdot10^4}$	$\frac{1}{\infty}$	$\sim \frac{1}{6\cdot10^5}$
$\frac{1}{2}\cdot\gamma_1\big\|_{\omega_x\neq\omega_j}$	$\sim \frac{1}{400}$	$\frac{1}{\infty}$	$\sim \frac{1}{2\cdot10^3}$
$\frac{1}{2}\cdot\gamma_2\big\|_{\omega_x\neq\omega_j}$	$\sim \frac{1}{3\cdot10^5}$	$\frac{1}{\infty}$	$\sim \frac{1}{1\cdot10^6}$
$\frac{1}{2}\cdot\gamma_3\big\|_{\omega_x\neq\omega_j}$	$\sim \frac{1}{3\cdot10^5}$	$\frac{1}{\infty}$	$\sim \frac{1}{2\cdot10^6}$
$\frac{1}{2}\cdot\gamma_4\big\|_{\omega_x\neq\omega_j}$	$\sim \frac{1}{8\cdot10^7}$	$\frac{1}{\infty}$	$\sim \frac{1}{4\cdot10^8}$
$\frac{1}{2}\cdot\gamma_5\big\|_{\omega_x\neq\omega_j}$	$\sim \frac{1}{100}$	$\frac{1}{\infty}$	$\sim \frac{1}{400}$
$\frac{1}{2}\cdot\gamma_6\big\|_{\omega_x\neq\omega_j}$	$\sim \frac{1}{9\cdot10^5}$	$\frac{1}{\infty}$	$\sim \frac{1}{4\cdot10^5}$
$\frac{1}{2}\cdot\gamma_7\big\|_{\omega_x\neq\omega_j}$	$\sim \frac{1}{100}$	$\frac{1}{\infty}$	$\sim \frac{1}{400}$
$\frac{1}{2}\cdot\gamma_8\big\|_{\omega_x\neq\omega_j}$	$\sim \frac{1}{9\cdot10^5}$	$\frac{1}{\infty}$	$\sim \frac{1}{4\cdot10^5}$
$\frac{1}{2}\cdot\gamma_9\big\|_{\omega_x\neq\omega_j}$	$\sim \frac{1}{8\cdot10^5}$	$\frac{1}{\infty}$	$\sim \frac{1}{3\cdot10^5}$

Table 3: Comparison of each term of the xth LOCSET error signal, S_x, for different integration times, τ. Cells highlighted in blue contain the LOCSET error terms we want to isolate as, when combined, they formulate an ideal control loop error signal. Values in each cell are normalized to the most dominate error term $\eta_3\big\|_{\omega_x=\omega_j}$.

Let's now consider a typical control loop integration time utilized in the experimental work discussed in later chapters, $\tau \approx 2.45 \mu s$. Said integration time, chosen to establish a balance between optimizing the LOCSET error signal and increasing the beam combination system bandwidth under similar operating conditions, does not strictly

meet the $\left(\tau \gg \dfrac{2\pi}{\left| \omega_x - \omega_{j \neq x} \right|} \right)$ condition previously discussed. The question then is whether

or not the desired LOCSET error signal components will remain dominant for the chosen integration time, τ.

Looking at Table 3, column 1, we see that, for an integration time of 2.45μs, the terms highlighted in blue are not nearly as dominate as for a 10.45μs integration time. All is not lost though as the closest term to $\eta_3 \big|_{\omega_x = \omega_j}$, excluding $\gamma_7 \big|_{\omega_x = \omega_j}$, has approximately

$1/50^{\text{th}}$ the contribution of $\eta_3 \big|_{\omega_x = \omega_j}$ and $1/25^{\text{th}}$ that of $\gamma_7 \big|_{\omega_x = \omega_j}$. All other terms of the error

signal, for a 2.45μs integration time, remain significantly smaller and therefore contribute very little to the overall error signal S_x. Even though a factor of 50 or 25 is nothing to scoff at it might be a bit of a stretch to mathematically ignore terms this close to the desired error signal components, $\eta_3 \big|_{\omega_x = \omega_j}$ and $\gamma_7 \big|_{\omega_x = \omega_j}$. As it turns out, in practice, the

beam combination systems discussed in later chapters, operating with a 2.45μs integration time, still perform quite nicely. When implementing integration times at or near to 2.45μs said experiments perform with average optical phase errors typically between λ/50 and λ/75 indicating that a factor of 50 over the nearest unwanted term in the error signal is indeed enough to establish low phase error coherent beam combination.
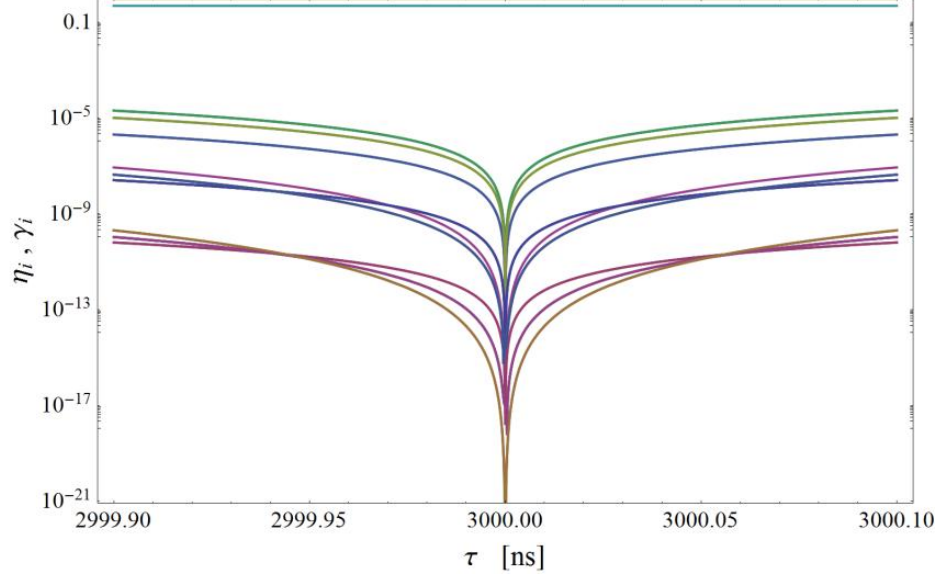
Figure 17: Plot of individual terms, η's and γ's, of the total phase error signal, S_x, defined in equation 3.75, as a function of integration time, τ, near 3μs.

Looking at the expressions for η_1, η_2, and η_3 and $\gamma_1 - \gamma_9$ we see that all terms are predominantly governed by the oscillatory behavior of sine and cosine functions. A question that might come to mind is whether or not there are localized sweet spots in the phase error signal where, for specific integration times, all terms go to zero except the desired terms, $\eta_3|_{\omega_x = \omega_j}$ and $\gamma_7|_{\omega_x = \omega_j}$. As it turns out, *for the frequency and phase modulation amplitude conditions previously defined*, integration times that are integer multiples of the beat note period between the two closest modulation frequencies,

$$\left(\tau = N \cdot \frac{2\pi}{\left| \omega_x - \omega_{j \neq x} \right|} \right)$$ where N is a positive integer not including 0, the phase error of

every term except those desired, $\eta_3|_{\omega_x = \omega_j}$ and $\gamma_7|_{\omega_x = \omega_j}$, does indeed go to zero as shown in

Figure **17** (for an integration time of 3μs). Said behavior is also evidenced in Table 3,

column 2, where all terms except $\eta_3\big|_{\omega_x=\omega_j}$ and $\gamma_7\big|_{\omega_x=\omega_j}$ equal zero ($1/\infty$) for an integration

time of 3μs.

Let's now consider the more general case were we will treat ω_x, ω_j, and ω_k as

unknown constants, we can then define a condition, or a set of conditions, on the

integration time τ where all undesired error signal terms will go to zero. Looking again at

the oscillatory behavior of all η and γ terms above we realize that if the products of $\tau\Delta\omega$

and $\tau\omega_i$ are equal to following quantities,

$$\tau \cdot \Delta\omega = N \cdot 2\pi, \qquad\qquad 3.76$$

$$\tau \cdot \omega_i = M \cdot 2\pi, \qquad\qquad 3.77$$

for all values of ω_i, the RF phase dither frequency of the ith LOCSET channel, and treat

M and N as integers (that cannot be equal unless: $\Delta\omega = \omega_i$), all undesired error terms will

evaluate to zero. Therefore, if the two general integration time conditions stated above, in

equations 3.76 and 3.77, are met the LOCSET error signal expressions for both Self-

Referenced and Self-Synchronous configurations will reduce to exactly that of the

simplified expressions provided in equations 3.73 and 3.74 respectively.

In summary, the safest way to operate a LOCSET coherent beam combination

system is to implement an integration time that meets our previously established

integration time condition, $\left(\tau \gg \dfrac{2\pi}{\left|\omega_x - \omega_{j\neq x}\right|} \right)$. If said condition is met, each undesired

term in the complete error signal for the xth channel, S_x, remains significantly smaller

than the desired error signal terms, $\eta_3\big|_{\omega_x=\omega_j}$ and $\gamma_7\big|_{\omega_x=\omega_j}$, regardless of how the

integration time is set. However if someone wishes to increase the response time of the

84

LOCSET control electronics by decreasing the integration time care must be taken to hit

on, or very near, the sweet spots strictly defined by equations 3.76 and 3.77 above.

Another possible way to decrease the integration time, and still meet the

integration time requirement, $\left(\tau \gg \dfrac{2\pi}{\left| \omega_x - \omega_{j \neq x} \right|} \right)$, is to simply increase the frequency

separation between the RF phase modulation frequencies in the control loop. Said action

must be weighed against the number of desired channels in the beam combination

system. If there are only two or three channels then separating the frequencies isn't really

a problem. If there are 30, 40, or even 50 channels then the user may encounter some

bandwidth limitations when trying to further separate the modulation frequencies.

3.3. LOCSET Implementation

In the analysis above we established both the Self-Referenced and Self-Synchronous

LOCSET error signals. In theory, only the procedures described above are needed to

correct for the optical phase differences of the entire system. In practice there are

practical limits to the components used in implementing a beam combination system.

Imagine the scenario of the Self-Referenced LOCSET beam combination system. There

is one un-modulated reference beam and N-1 phase modulated beams. Let assume each

of the N beams is confined to individual, spatially separate, optical fibers of some

common length. Now imagine that the un-modulated reference fiber is slowly heated,

maybe with a hot plate. The heated fiber undergoes an index of refraction change due to

the change in temperature, $\left(dn \big/ dT \right)$, and thereby experiences changes in optical path

length. During heating, the phase of the un-modulated beam changes independently of the

other beams. Because there is no phase control on the reference beam each of the other

channels must track in phase with the un-modulated reference as well as to each other.

Let's assume that the un-modulated beam undergoes 1000 waves of phase change due to

the heating. Each of the modulated beams must also be able to change their phases by an

equivalent amount to maintain optimal phase locking without interruption. We'll also

assume that the modulated beams are phase controlled via an off the shelf electro-optical

phase modulators (i.e. $LiNbO_3$ phase modulators) that equate changes in applied voltage

to changes in optical phase at a rate of one wave of phase change for every 5 volts

applied ($V_\pi = 2.5V$). This would require 5000 volts for 1000 waves of phase change. This

is an impractical expectation in the physical world, at least when dealing situations where

N is large.

There is a solution to this problem however. Each time an optical beam cycles 1

wave of phase (2π radians) it is as if the phase of the beam returned to zero phase change,

ignoring of course coherence length considerations. This is most easily seen when

considering two beam interference governed by equation 3.1,

$$\left.\frac{Int(\Delta\phi)}{Int_o}\right|_{MAX} = 2(1+\cos(0)) = 2(1+\cos(2 \cdot N \cdot \pi)) = 4. \qquad 3.1$$

Here the intensity of the two combined beams is optimized (maximum) when the phase

difference between the 2 beams is an integer multiple of 2π, $(\Delta\phi = N \cdot 2\pi)$ including N =

0. This property of beam interference can be exploited to reduce the voltage requirement

at a given phase modulator. Once the phase of the xth modulated beam has been changed

by some threshold value, the control loop channel can be designed to reset, or reduce, the

voltage on the phase controller in accordance with a $2\pi N$ phase shift. If done fast enough

said reset will only pull the system out of optimal performance for a very short time. Implementation of this reset will be described in the following section.

3.3.1 Practical Implementation of LOCSET
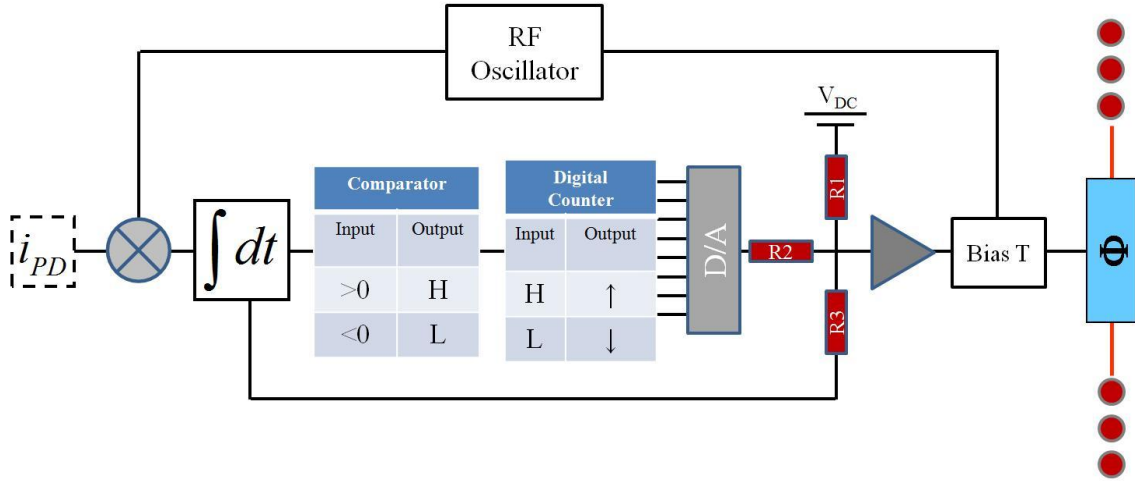
Figure 18: Basic operational schematic of single channel LOCSET operation. N-1 identical LOCSET channels, with the exception of different RF phase dither frequencies, are implemented in a Self-Referenced LOCSET system.

Figure 18 provides a basic conceptual view of how a single LOCSET channel is experimentally implemented. Notice that it is essentially the same schematic shown in Figure 16 but this time with the addition of a comparator, a digital counter, and a digital to analog (D/A) converter. These components combine to form a digital reset circuit providing a single LOCSET channel the capability of performing $2\pi N$ resets when the applied phase change at the xth phase modulator has reached some threshold value.

It is easiest to conceptually understand single channel LOCSET operation by beginning at the RF oscillator shown at the top of Figure 18. The signal from the RF oscillator is split two ways with one feeding into a bias-T and then to the phase modulator. This is the unique RF phase dither applied to the xth optical beam that will be used to demodulate its phase error with respect to all others, as mathematically outlined

earlier in this chapter. The second portion of the RF signal is mixed with the sampled total photocurrent input into the xth LOCSET channel, as shown to the left of Figure 18. The mixed signal is then integrated over some time τ and the error signal for the xth LOCSET channel, shown in equation 3.73, is generated. This error signal is then split 2 ways with one portion feeding into a weighted summing amplifier and the second portion feeding into the digital reset circuit. The first component of the digital reset circuit, a comparator, latches high if the LOCSET error signal is greater than zero and latches low if less than zero. The value, either high or low, feeds into an 8 bit bi-directional digital counter that either counts up, if latched high, or down, if latched low. The output of the digital counter is then feed to a D/A converter where a full 8 bit cycle is converted to a voltage corresponding to a $2\pi N$ phase change at the phase modulator (where N is an integer). If the counter counts beyond its last byte, the 256th, it immediately begins again at zero. This large and sudden change at the digital counter translates to a $2\pi N$ voltage change at the D/A converter, forcing the phase modulator to reset by $2\pi N$. N is typically chosen to be less than or equal to three and depends entirely on threshold values of the phase modulators used and experimental requirements. The D/A output is also feed to the weighted summing amplifier. Here the digital reset circuit output, the error signal from the integrator, and a DC bias are weighted, summed together and input to a bias-T. Here the signal is combined with the unique RF phase dither and sent to the phase modulator for final phase correction, and RF phase modulation.

The digital reset circuit serves two purposes. The first is to provide over voltage protection at the phase modulator. The second purpose is to keep the LOCSET error signal at or near zero by taking the applied voltage load to the phase modulator from the

integrator. If the integrator output, and therefore the error signal, is above zero the digital reset circuit will continue to count up until the integrator output becomes zero again. This allows the voltage output of the integrator to stay at or near zero, well between its voltage rails, and the digital reset circuit to perform its primary function, limiting the voltage at the phase modulator while maintaining phase lock of the xth beam with respect to each of the others.

3.3.2 LOCSET Implementation Considerations

So far we have painted a rosy picture of a coherent beam combination system that can take N optical beams with identical optical properties and coherently combined them via LOCSET, regardless of what those optical properties may be. Unfortunately there are some practical considerations that need to be considered; the two most important being single frequency operation and linewidth of the optical sources to be combined.

If the lasers to be combined are not single frequency then the possibility of complex beat notes, due to the frequency difference of the 2 modes, at the photodetector becomes very real and can confuse the LOCSET control electronics. Even if the phase error contribution of a single optical frequency can be isolated and corrected for there is no guarantee that light at other frequencies will also be optimally combined. Multi-tone coherent beam combination is an active area of research but the work is still in its infancy, see reference [62].

The final consideration is that of the linewidth of the combined laser sources. The linewidth of an optical beam does not pose any direct limitations on the phase locking control electronics. The limitation comes into play via the actual interaction of the optical beams at or before the photodetector that feeds the LOCSET electronics. As the linewidth

of the laser sources is increased the coherence length of each of the beams decreases according to equation 3.78,

$$l_c = \frac{c}{\Delta v},$$
3.78

where l_c is the coherence length of an optical beam, c is the speed of light (3×10^8 m/s) and Δv is the linewidth of the laser source. For narrow linewidths, on the order of 10's of kilohertz, the coherence length is 10's of kilometers. If the linewidth of the laser source is increased to 10's of gigahertz the coherence length is reduced to just a few 10's of millimeters. Therefore, for broader linewidth laser sources, the optical path length matching requirement becomes a real concern as each beam's path length must be controlled to a fraction of the optical coherence length of a single beam.

To combine multiple coherent optical sources, with linewidths of 10 GHz, the optical path length differences must be controlled to within a fraction of the coherence length, l_c, of 30mm. Let's assume that the requirement on the path length difference between any two beams in the system must be within 1/10th of the overall coherence length of a single beam, l_c (not an unreasonable condition). This would require that the optical path length difference between each of the beams in the system to be within 3mm of each other. Depending of the design of the optical system, and the number of combined beams involved this can be a difficult, but not impossible, condition to meet.

The simple solution to the path length problem would be to narrow the linewidth of the optical sources. An extreme, though not unreasonable, shift could be to implement 10 kHz laser sources. This would provide a coherence length of 30km which would make the path length differences between beams a non-concern. The reader may recall from

Chapter 2 the discussion regarding output power trade off's between building fiber amplifiers with narrow and broadened linewidths. Narrow linewidths provide the flexibility of not having to account for optical path length differences between the combined amplifiers but introduces non-linear effects in the amplifiers that ultimately limit their output power. By utilizing broader linewidths it becomes much easier to produce high output powers from each of the sources to be combined but it can force stringent optical path length considerations. A balance needs to be made between broadening the linewidth of the optical sources and optical path length matching. There isn't necessarily a correct balance for all situations as it will be dictated primarily by the needs of the user, what technologies are available, and how much complexity the user is willing to have in the beam combination system.

3.4. Chapter Summary:

In this chapter this author derived the detailed and simplified error signal expressions for both the Self-Referenced and Self-Synchronous LOCSET configurations. The reader was then presented with a detailed error analysis of the complete LOCSET error signal demonstrating that, under typical experimental conditions, the expressions for both Self-Referenced and Self-Synchronous configurations do indeed simplify to the basic expressions found in equations 3.73 and 3.74 respectively. The chapter was then concluded with a discussion on the general implementation of the LOCSET phase locking electronics in a basic coherent beam combination system.

Chapter 4.   Theory of Optical Phase Error Measurements:

Two fundamental properties of an optical beam are its field amplitude and its phase state. Measuring relative field amplitude is rather straight forward. Simply place a photodetector into a beam and measure the detector output voltage vs. time. This data can then be related to the beams relative field amplitude by detector and free space constants. Measuring phase characteristics of an optical beam is a bit more elusive and will be the primary focus of this chapter. A diagnostic setup utilizing in-phase (I) and quadrature (Q) data processing to measure the optical phase of a beam, whether a single beam (single channel) or the output of multiple coherently combined beams (multi-channel), with respect to a stable reference beam will be described mathematically and discussed in the sections to follow.

4.1. Mathematical Description: Single Channel Optical Phase Error Measurements
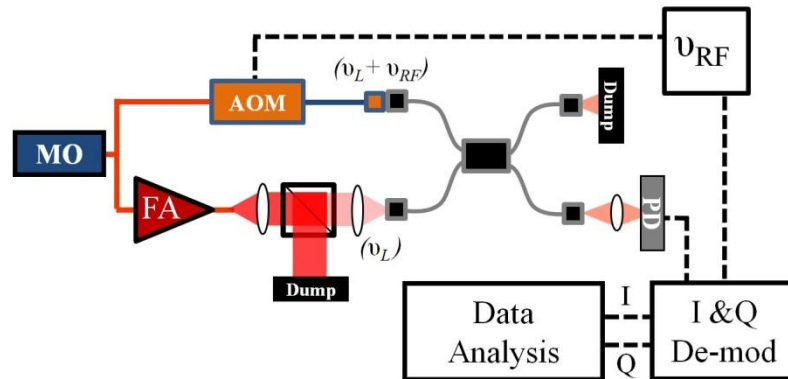
Figure 19: Single channel phase error measurement experimental setup. As shown, measures the phase difference of the amplified beam (FA-Fiber Amplifier) with respect to a frequency shifted reference beam. (MO: Master Oscillator, AOM: Acousto-Optic Modulator, υ_L: Optical Frequency, υ_{RF}: RF Frequency, PD: Photodetector)

It is easiest to understand the mathematics of a phase error measurement with knowledge of its experimental setup and implementation. The setup shown in Figure 19 begins at the left with a stable single frequency master oscillator (MO). The MO is coupled into a fiber and split two ways. The lower fiber feeds into a fiber amplifier (though any sort of phase disturbance could be represented here) where we expect phase changes, primarily due to thermal changes in the amplifier, to occur during the different stages of operation. The second upper most fiber feeds into an acousto-optic modulator (AOM) where the light undergoes a frequency shift of υ_{RF}, typically 80-100 MHz [63,64]. The light from the fiber amplifier and the unamplified frequency shifted reference fiber are each coupled into a 2x2 fiber coupler where the 2 beams are combined. The combined light is divided and exits both output fibers of the 2x2 coupler, though only one output will be used in measuring the optical phase difference between the two beams; the other is dumped into a beam block. The combined output, a complex interference beat note governed by the differences between the frequency and time

93

varying optical phases of the two beams, is then incident on a photodetector which feeds

into the I and Q data processing electronics. I and Q are then generated via coherent RF

demodulation and saved as a function of time for later analysis. The experimental setup

described above, and shown in Figure 19, is the same as, or very similar to, the

experimental configurations shown in references: 63, 64, 65, and 66.

4.1.1 Field Equations

Let's begin our discussion by defining each of the optical fields involved in measuring

the phase error of an optical beam: the phase stable, frequency shifted, reference beam,

E_R, and the field of interest we aim to measure the phase changes of, E_i, over some data

acquisition time t_{Acq}, as defined in equations 4.1 and 4.2 respectively,

$$E_R(t) = E_{Ro} \cos\left(\omega_R t - k_R z + \phi_R\right),$$

4.1

$$E_i(t) = E_{io} \cos\left(\omega_i t - k_i z + \phi_i\right).$$

4.2

Here E_{Ro} and E_{io} are the field amplitudes of E_R and E_i respectively, ω_R and ω_i are

proportional to the frequency of E_R and E_i, k_R and k_i are the wave numbers of E_R and E_i, z

is the position in space of the time varying interaction of E_R and E_i, and finally, ϕ_R and ϕ_i

are the optical phase states of E_R and E_i respectively. For simplicity let's assume that the

field amplitudes of the two beams are equal, $\left(E_{Ro} = E_{io} = E_o\right)$, and the location of beam

interaction is at position $z = 0$. With these considerations equations 4.1 and 4.2 simplify

to equations 4.3 and 4.4 respectively,

$$E_R(t) = E_o \cos\left(\omega_R t + \phi_R\right),$$

<div align="right">4.3</div>

$$E_i(t) = E_o \cos\left(\omega_i t + \phi_i\right).$$

<div align="right">4.4</div>

Before proceeding with the mathematical analysis it is important to make

absolutely clear that with the experimental configuration shown in **Figure 19**, *and*

described in the discussion to follow, that we are not measuring the absolute optical

phase of the beam of interest, E_i. Instead we are measuring the optical phase difference,

$\Delta\phi$, between the electric field of interest, E_i, and the reference field, E_R. Therefore, if for

some reason the phase of the reference beam is changing wildly and independently in

time this measurement will have little to no practical meaning. If care is taken to isolate

the reference beam from environmental phase changes then we can treat it as having a

fixed, or minimally varying, phase state for a given time frame when compared to the

time varying phase behavior of the beam of interest. If this condition is true then we

assume that by measuring the phase differences between the two beams, $\Delta\phi$, we are

effectively measuring the optical phase changes of E_i over some acquisition time, t_{Acq}.

In chapters to follow, pertaining to phase error measurements of single and multi-

channel systems, background measurements to determine the noise of the individual

measurement systems will be discussed in detail. Background disturbances, phase

differences between the reference field and the field of interest due to external influences

outside the control of the experiment, are measured for the respective experimental

setups. Typical measurement errors of 0.2 radians ($\sim\lambda/30$) were observed for the larger

scale single amplifier phase error measurement and errors of 0.016 - 0.013 radians ($\lambda/400$

- $\lambda/500$) were typically observed for the more environmentally controlled multi-channel

beam combination experiments. Said results demonstrate that there is little phase

<div align="center">95</div>

variation between the field of interest and the reference field when no deliberate phase disturbances are applied and thus supports the claim of having a phase stable reference beam.

4.1.2 Time Varying Intensity

This author knows of no photodetector that can directly measure electric field characteristics of an optical beam. Instead detectors are capable of measuring the optical intensity of a beam which is related to the electric field via equation 4.5,

$$Int_T(t) = \frac{1}{2} \cdot \left(\frac{\varepsilon_o}{\mu_o} \right)^{\frac{1}{2}} E_T^2(t). \qquad 4.5$$

For the purpose of this discussion $E_T(t)$ is the sum of the reference field, E_R, and the field of interest, E_i. If we plug in the expressions for E_i and E_R into equation 4.5, assume each beam is co-propagating and occupying the same space (i.e. perfect overlap), and utilize a few standard trig identities we get a new expression for the optical intensity of the interfering beams as shown in equation 4.6,

$$Int_T(t) = 2 \cdot Int_o \left(1 + \cos\left(\Delta\omega \cdot t + \Delta\phi(t) \right) \right), \qquad 4.6$$

Here Int_o is the optical intensity of a single beam, $\left(Int_o = \frac{1}{2} \cdot \left(\frac{\varepsilon_o}{\mu_o} \right)^{\frac{1}{2}} E_o^2 \right)$, $\Delta\omega$ represents the optical frequency difference between E_i and E_R, often referred to as the optical beat note frequency, and $\Delta\phi(t)$ is the time varying optical phase difference between the two electrics fields, E_R and E_i. *For the rest of our discussion the dependence of $\Delta\phi$ on time will been left out for simplicity as it is assumed $\Delta\phi$ changes much more slowly than the*

intensity fluctuations introduced by $\Delta\omega$. From here, the goal is to isolate $\Delta\phi$ from all other components of the optical beat note defined by equation 4.6.

4.1.3 Transition to Electronic Domain

Because the data processing happens in the electronic domain we must first convert the optical intensity to an electrical current $i_{PD}(t)$. This is done by placing a photodetector at a fixed position in the beam path (remaining true to the assumptions above, at $z = 0$). Here the optical intensity is converted to an electrical current via equation 4.7,

$$i_{PD}(t) = R_{PD} \cdot A \cdot Int_T(t),$$

4.7

where R_{PD} is the responsivity of the photodetector, A is the active area of the photodetector, and $Int_T(t)$ is the time varying optical intensity incident on the active area of the photodetector. It is assumed throughout this analysis that the responsivity of the photodetector is uniform across the entire active area of the photodetector. It is also assumed that the active area of the photodetector is uniformly illuminated by the optical beam. By plugging the expression for the optical intensity, equation 4.6, into equation 4.7 we have a complete expression for the photodetector current, $i_{PD}(t)$, as shown in equation 4.8,

$$i_{PD}(t) = R_{PD} \cdot A \cdot 2 \cdot Int_o \left(1 + \cos\left(\Delta\omega \cdot t + \Delta\phi\right)\right).$$

4.8

Notice that the optical phase difference, $\Delta\phi$, is only found in the right most AC term in equation 4.8. As we are only interested in measuring $\Delta\phi$ as a slowly varying function of time it is useful to filter out the DC term, the left most term in parenthesis of equation 4.8, by utilizing an AC coupled photodetector. In dropping the DC term we are left with

the following expression for the AC photocurrent, $i_{AC}(t)$, shown in equation 4.9, where $\left(\chi = R_{PD} \cdot A \cdot 2 \cdot Int_o\right)$,

$$i_{AC}(t) = \chi \cdot \cos\left(\Delta\omega \cdot t + \Delta\phi\right).$$

4.9

Again, $\Delta\omega$ is proportional to the difference in frequency between the frequency shifted reference beam, E_R, and the beam of interest, E_i, and $\Delta\phi$ is the slowly varying optical phase difference between the 2 beams respectively.

4.1.4 Isolate $\Delta\phi$ via I & Q Data Processing

As stated above, the primary goal of this chapter is to derive a method of measuring the optical phase difference, $\Delta\phi$, of a beam of interest, E_i, with respect to a stable reference beam, E_R. This is done in a similar manner as the LOCSET error signal is generated, via coherent RF demodulation, as outlined in Chapter 3. To begin we must first re-write equation 4.9 in a different form utilizing the trig identity shown in equation 4.10,

$$\cos\left(\alpha + \beta\right) = \cos\left(\alpha\right)\cos\left(\beta\right) - \sin\left(\alpha\right)\sin\left(\beta\right).$$

4.10

If we set α equal to the phase difference between the two fields, $\left(\alpha = \Delta\phi\right)$, and β equal the difference in frequency, $\Delta\omega$, multiplied by time, $\left(\beta = \Delta\omega \cdot t\right)$, equation 4.9 becomes equation 4.11,

$$i_{AC}(t) = \chi\left(\cos\left(\Delta\phi\right)\cos\left(\Delta\omega \cdot t\right) - \sin\left(\Delta\phi\right)\sin\left(\Delta\omega \cdot t\right)\right).$$

4.11

From here it is instructive to lump the slowly varying terms of $\Delta\phi$ into expressions for $I(\Delta\phi)$, the 'in-phase' component, and $Q(\Delta\phi)$, the 'quadrature' component of $i_{AC}(t)$ as

shown in equations 4.12 and 4.13 respectively, and write a new expression for $i_{AC}(t)$

using in-phase and quadrature components, $I(\Delta\phi)$ and $Q(\Delta\phi)$, as shown in equation 4.14,

$$I(\Delta\phi) = \chi\cos(\Delta\phi),$$
4.12

$$Q(\Delta\phi) = \chi\sin(\Delta\phi),$$
4.13

$$i_{AC}(t) = I(\Delta\phi)\cos(\Delta\omega\cdot t) - Q(\Delta\phi)\sin(\Delta\omega\cdot t)$$
4.14

Up to now no actual changes have been assigned to the photodetector current. We've

simply mathematically separated the different components of $i_{AC}(t)$ as governed by

common optical properties. The task now is to isolate $I(\Delta\phi)$ and $Q(\Delta\phi)$ from equation

4.14 via coherent RF demodulation. It is important to note that $I(\Delta\phi)$ and $Q(\Delta\phi)$ are the

Fourier cosine and sine coefficients of $i_{AC}(t)$ at frequency $\Delta\omega$, respectively, and can be

isolated by simply multiplying, or mixing, $i_{AC}(t)$ with a sine or cosine demodulation

signal at a frequency $\Delta\omega$ and integrating over some time T. In the following subsections

we will perform these operations, isolate $I(\Delta\phi)$ and $Q(\Delta\phi)$, and discuss the final results.

4.1.4.1 Isolate $I(\Delta\phi)$: Calculate Fourier Cosine Component of $i_{AC}(t)$

Though chosen arbitrarily we'll begin by isolating $I(\Delta\phi)$ from the expression for

$i_{AC}(t)$ found in equation 4.14. To do so we must first multiply the expression for $i_{AC}(t)$ by

the cosine of the demodulation frequency $\left(\cos(\Delta\omega\cdot t)\right)$. The next step is to integrate the

combined signal over a significantly long time, T, to isolate $I(\Delta\phi)$ from $i_{AC}(t)$ as governed

by T being much greater than the inverse of the RF beat note frequency, $\left(T \gg 2\pi/\Delta\omega\right)$,

and shown in equation4.15,

$$a_c = \frac{1}{T} \int_0^T i_{AC}(t) \cos(\Delta\omega \cdot t) \, dt. \tag{4.15}$$

Plugging in the expression for $i_{AC}(t)$, equation 4.14, into equation 4.15, and separating the integrals we have the following equation, 4.16, for the Fourier cosine component, a_c,

$$a_c = \frac{I(\Delta\phi)}{T} \int_0^T \cos^2(\Delta\omega \cdot t) \, dt - \frac{Q(\Delta\phi)}{T} \int_0^T \sin(\Delta\omega \cdot t) \cos(\Delta\omega \cdot t) \, dt. \tag{4.16}$$

Notice that as the integration time, T, increases the integral to the right remains small (as it oscillates about zero) while the integral to the left continually increases as $\cos^2(\Delta\omega \cdot t)$ is positive for all t. For significantly long integration times, T, we can ignore the terms to the right and write equation 4.16 as equation 4.17,

$$a_c = \frac{I(\Delta\phi)}{T} \int_0^T \cos^2(\Delta\omega \cdot t) \, dt = \frac{I(\Delta\phi)}{2T} \left(\int_0^T dt + \int_0^T \cos(2 \cdot \Delta\omega \cdot t) \, dt \right). \tag{4.17}$$

Performing the final integration for large T we have the final expression for the Fourier cosine component of $i_{AC}(t)$, a_c, as shown in equation 4.18,

$$a_c = \frac{I(\Delta\phi)}{T} \left(\frac{T}{2} - 0 \right) = \frac{I(\Delta\phi)}{2}. \tag{4.18}$$

Here a_c is a measureable quantity that differs from the 'in-phase' component of $i_{AC}(t)$, $I(\Delta\phi)$, only by a factor of $1/2$.

4.1.4.2 Isolate Q(Δφ): Calculate Fourier Sine Component of $i_{AC}(t)$

Next we want to isolate the quadrature component of $i_{AC}(t)$, $Q(\Delta\phi)$, by calculating the Fourier Sine component of $i_{AC}(t)$, a_s. This is accomplished by multiplying, or mixing, $i_{AC}(t)$ by the a sinusoidal demodulation signal of frequency $\Delta\omega$, $(\sin(\Delta\omega \cdot t))$, and then

integrating the result for a significantly long integration time, T, as defined previously $(T \gg 2\pi/\Delta\omega)$. Because the mathematical analysis is virtually identical as that used to isolate the 'in-phase' component of $i_{AC}(t)$, $I(\Delta\phi)$, we will simply define the Fourier sine component, a_s, in equation 4.19, and provide the result in equation 4.20,

$$a_s = \frac{1}{T}\int_0^T i_{AC}(t)\sin(\Delta\omega \cdot t)dt,$$
4.19

$$a_s = -\frac{Q(\Delta\phi)}{2}.$$
4.20

As seen in equation 4.20 the measurable Fourier sine component, a_s, of the optical intensity, $i_{AC}(t)$, differs from the quadrature component, $Q(\Delta\phi)$, by a factor of $-1/2$.

4.1.4.3 Extracting Δϕ

Equations 4.18 and 4.20 provide us with measurable quantities that are proportional to the optical phase difference, $\Delta\phi$, between the reference field, E_R, and the field of interest, E_i. Unfortunately, by themselves, their usefulness is limited due to the discontinuous behavior of arcsines and arccosines, where quadrant mapping is difficult and often impossible (phase unwrapping through multiples of π). If we look closely though we realize that if we take the ratio of a_s and a_c we get an expression proportional to the tangent of the optical phase difference, $\Delta\phi$, shown in equation 4.21,

$$\frac{a_s}{a_c} = \frac{-Q(\Delta\phi)}{I(\Delta\phi)} = -\tan(\Delta\phi).$$
4.21

The negative sign in the two right most terms of equation 4.21 can easily be accounted for by simply multiplying the ratio of the measureable quantities, a_s and a_c, by (-1) during final data processing as shown in equation 4.22,

$$(-1)\frac{a_s}{a_c} = \frac{Q(\Delta\phi)}{I(\Delta\phi)} = \tan(\Delta\phi).$$

4.22

We then solve equation 4.22 for the final expression of $\Delta\phi$ as shown in equation 4.23,

$$\Delta\phi = \tan^{-1}\left(\frac{Q(\Delta\phi)}{I(\Delta\phi)}\right) = \tan^{-1}\left(-\frac{a_s}{a_c}\right).$$

4.23

We see in equation 4.23 that the optical phase difference, $\Delta\phi$, between the field of

interest, E_i, and the reference field, E_R, is equal to the arctangent of the ratio of the

quadrature, $Q(\Delta\phi)$, and in-phase, $I(\Delta\phi)$, components of the time varying optical intensity.

Therefore, by measuring $I(\Delta\phi)$ and $Q(\Delta\phi)$, or more accurately a_s and a_c (and accounting

for the negative sign), it is easy to extract the optical phase difference, $\Delta\phi$, as a slowly

varying function of time. Unfortunately though, due to the nature of the arctangent, when

$\Delta\phi$ extends beyond $\pm\frac{\pi}{2}$ our expression for $\Delta\phi$ becomes asymptotic and does not directly

reflect reality. To account for this solely mathematical behavior we will utilize a simple

method of quadrant mapping to un-wrap the phase behavior described in equation 4.23.

4.1.4.4 Phase Data Unwrapping and Quadrant Mapping (Simulated)
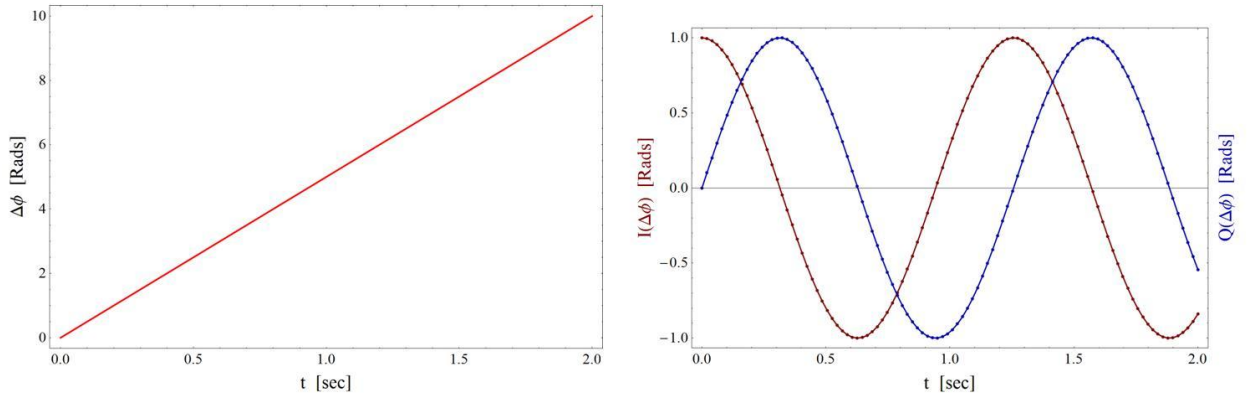
Figure 20 Left: Defined linear phase behavior, $\Delta\phi$, as a function of time. Right: Resulting simulated measurement of $I(\Delta\phi)$ & $Q(\Delta\phi)$ data.

The aim of the demonstration to follow is to establish a method capable of accounting for any 'non-physical' discontinuities in the phase behavior when $\Delta\phi$ extends beyond the $+/- \pi/2$ limit of the arctangent found in equation 4.23. For the purposes of this discussion we'll assume we know for certain that $\Delta\phi$ is a linear function in time and increases at a rate of 5 radians per second, as shown in Figure 20 (left) and described by the following equation,

$$\Delta\phi(t) = 5 \cdot t.$$
4.24

We'll also assume that all $I(\Delta\phi)$ and $Q(\Delta\phi)$ measurements have been completed, governed by equations 4.12 and 4.13 respectively, and are also shown Figure 20 (right). According to equation 4.23, we simply take the arctangent of the ratio of $Q(\Delta\phi)$ to $I(\Delta\phi)$ for each corresponding pair of data points in Figure 20 to determine the time varying phase behavior, $\Delta\phi$. Said operations are then performed to generate the calculated phase behavior, $\Delta\phi$, shown Figure 21.
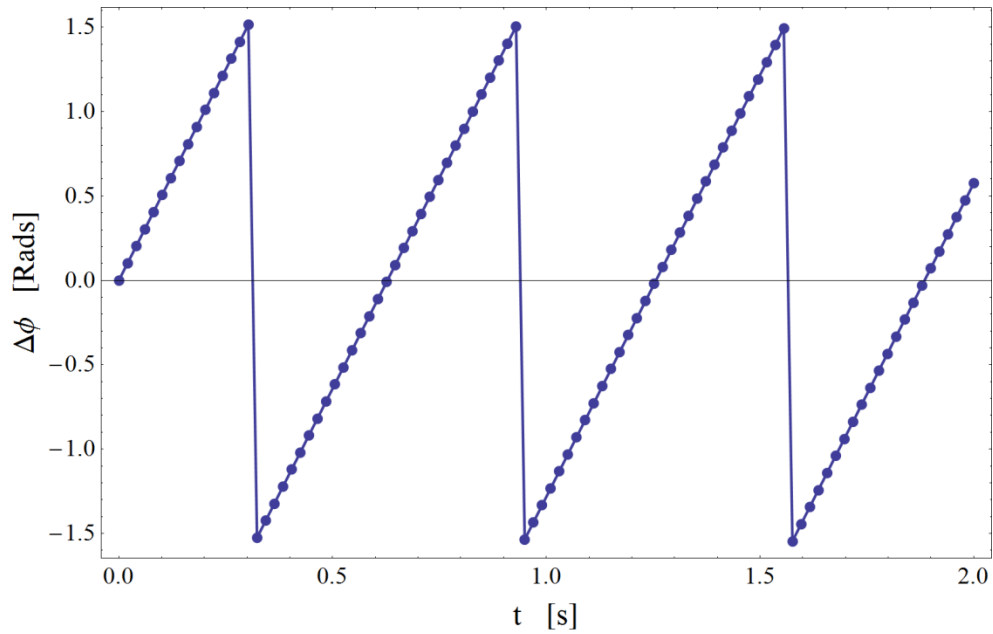
Figure 21: Calculated phase behavior, $\Delta\phi$, from the simulated $I(\Delta\phi)$ and $Q(\Delta\phi)$ data shown in Figure 20 (no phase unwrapping).

The result shown in Figure 21 is a segmented linear function with discontinuities and not

the perfectly linear function we had expected to find (that shown in Figure 20). When

comparing Figure 21 to Figure 20 it looks as if it might possible to devise a set of rules to

shift the linear segments of Figure 21 and rebuild the linear behavior we had expected. As

it turns out, these rules are determined via quadrant mapping and are discussed below.
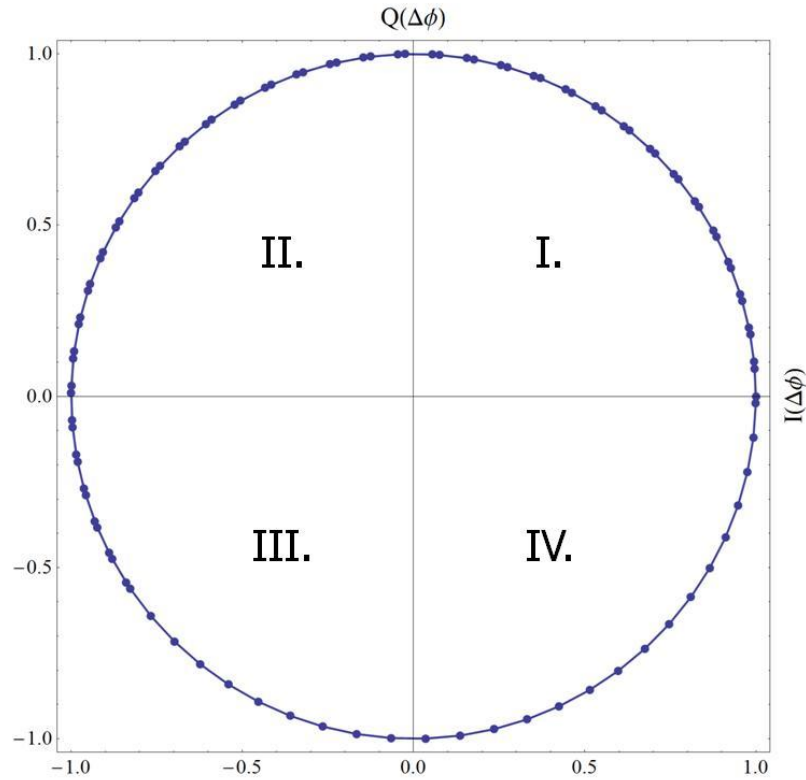
Figure 22: IQ data parametric plot. Data normalized to 1 and used in determining how to unwrap the calculated piece wise phase behavior, $\Delta\phi$, shown in Figure 21.

If we plot our $I(\Delta\phi)$ and $Q(\Delta\phi)$ data as a parametric plot, as shown in Figure 22,

we find that the result is a circle centered about the $(0, 0)$ point of a Cartesian plane. It is

then possible to monitor which of the four Cartesian quadrants each IQ data pair is

located in. By tracking the quadrant that each IQ data pair lies in we can create a list of

rules that determine when, and how, to shift the raw phase behavior data $\Delta\phi$, shown in

Figure 21, to correct for each non-physical discontinuity in its data set. Though not

immediately obvious in the data shown above said rules are as follows:

· If the ith IQ pair is found in quadrant 1, and the [i+1] IQ pair is found in quadrant 2, then shift the raw $\Delta\phi$ data in Figure 21, beginning at point [i+1], by $^+\pi$ radians.

· If the ith IQ pair is found in quadrant 2, and the [i+1] IQ pair is found in quadrant 1, then shift the raw $\Delta\phi$ data in Figure 21, beginning at point [i+1], by $^-\pi$ radians.

· If the ith IQ pair is found in quadrant 3, and the [i+1] IQ pair is found in quadrant 4, then shift the raw $\Delta\phi$ data in Figure 21, beginning at point [i+1], by $^+\pi$ radians.

· If the ith IQ pair is found in quadrant 4, and the [i+1] IQ pair is found in quadrant 3, then shift the raw $\Delta\phi$ data in Figure 21, beginning at point [i+1], by $^-\pi$ radians.

The 4 rules listed above tell us that each time our in-phase and quadrature data pairs cross between quadrants 1 and 2, or between quadrants 3 and 4, the raw phase behavior data shown in Figure 21 must be shifted by +/- π. A positive shift occurs when the IQ data traverses between quadrants counter clockwise whereas a negative shift occurs when the IQ data traverses clockwise between quadrants. Programmatically these rules are rather straightforward to implement and the result is shown in Figure 23.
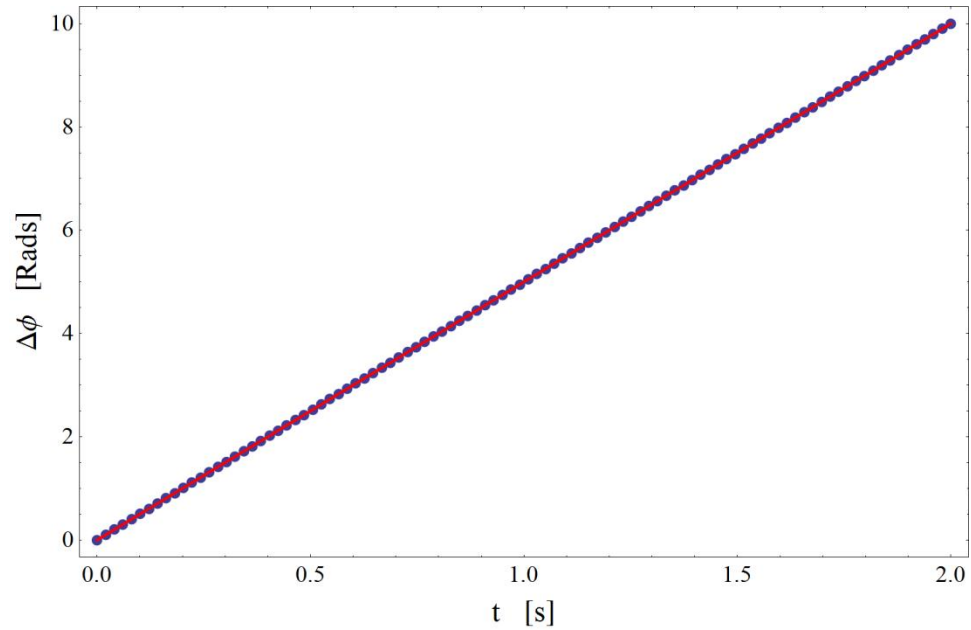
Figure 23: Result when quadrant mapping is used to un-wrap phase difference function in Figure 21.

When rules listed above are applied to the discontinuous phase behavior data set shown in Figure 21, we end up with our desired linear data set, $\Delta\phi$, shown in Figure 23. Pay special attention to that fact that the unwrapped calculated phase behavior shown in Figure 23 tracks very well to the expected linear phase behavior of $\Delta\phi$ (from Figure 20, overlaid in red).

It needs to be mentioned that, if these rules are to be followed, there must be at least one collected data point in each quadrant in the IQ phase plane shown in Figure 22. Stated another way, there must be at least one data point per $\pi/2$ phase change in the optical beam(s) being analyzed. If said condition is not met then there is no accurate or guaranteed way to unwrap phase behavior data when utilizing equation 4.23.

4.2. Mathematical Description: Multi-Channel Optical Phase Error Measurements
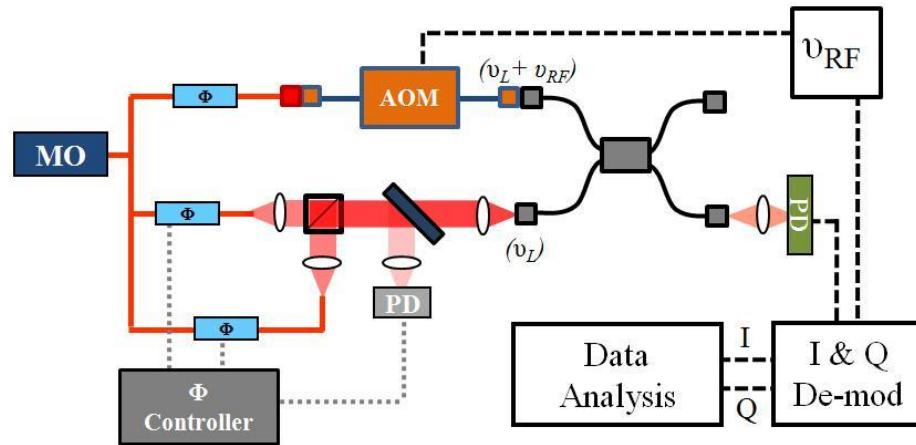
Figure 24: Multi-channel phase error measurement experimental setup. As shown, measures the phase difference of a 2 channel coherently combined beam with respect to a frequency shifted reference beam. (MO: Master Oscillator, AOM: Acousto-Optic Modulator, υ_L: Optical Frequency, υ_{RF}: RF Frequency, PD: Photodetector)

Up until now we have only considered measuring the phase error of single beam, E_i, with respect to a stable reference beam, E_R. This is an important case to be sure but the measurement can easily be extended to measuring the phase error of a coherently combined beam, E_c, comprised of N individual beams, as shown in Figure 24. In the text to follow we will justify such an experiment by mathematically showing that a coherently combined beam, where the phase state, ϕ_i, of each of the N beams in the combined beam is the same except for possible small deviations $\Delta\phi_i$, can be treated, *for informational purposes only*, as a single beam. If treated as a single beam the IQ phase error demodulation technique described previously for a single beam can also be applied to measure the phase error of the coherently combined beam.

4.2.1 Define Electric Field for Coherently Combined Beam, E_c

Let's begin our discussion with an expression for a coherently combined beam, E_c, as shown in equation 4.25,

$$E_C(t) = \sum_{i=1}^{N} E_i(t).$$
<div align="right">4.25</div>

Here E_i is the electric field of a single beam as expressed in equation 4.3 assuming common optical frequencies, field amplitudes, and polarizations for all beams in the combination system. Plugging equation 4.3 into our expression for the combined beam, E_C, we have equation 4.26,

$$E_C(t) = E_o \sum_{i=1}^{N} \cos(\omega \cdot t + \phi_i).$$
<div align="right">4.26</div>

Utilizing the trigonometric identity shown in equation 4.10 we can rewrite equation 4.26 as shown in equation 4.27

$$E_C(t) = E_o \cos(\omega \cdot t) \sum_{i=1}^{N} \cos(\phi_i) - E_o \sin(\omega \cdot t) \sum_{i=1}^{N} \sin(\phi_i).$$
<div align="right">4.27</div>

Assuming that each of the N beams in the combined beam deviate from some common optimal phase condition, ϕ_C, by some unknown amount, $\Delta\phi_j$, we can then write the expression for the combined beam as follows,

$$E_C(t) = E_o \cos(\omega \cdot t) \sum_{j=1}^{N} \cos(\phi_C + \Delta\phi_j) - E_o \sin(\omega \cdot t) \sum_{j=1}^{N} \sin(\phi_C + \Delta\phi_j).$$
<div align="right">4.28</div>

By expanding the sine and cosine terms in equation 4.28 we obtain the following expression for the combined beam, E_c,

$$E_C(t) = \begin{pmatrix} E_o \cos(\omega \cdot t) \left(\cos(\phi_C) \sum_{j=1}^{N} \cos(\Delta\phi_j) - \sin(\phi_C) \sum_{j=1}^{N} \sin(\Delta\phi_j) \right) \\ -E_o \sin(\omega \cdot t) \left(\sin(\phi_C) \sum_{j=1}^{N} \cos(\Delta\phi_j) + \cos(\phi_C) \sum_{j=1}^{N} \sin(\Delta\phi_j) \right) \end{pmatrix}. \qquad 4.29$$

Up to this point no simplifications or assumptions have been made except that each beam

shares common frequency, amplitude, and polarization characteristics. The phase states

of each beam are left to wander freely, $\Delta\phi_j$, from a common optimal phase state, ϕ_C. Let's

now assume that a method of phase optimization, such as LOCSET, is implemented and

the deviation, $\Delta\phi_j$, from the optimal phase state, ϕ_C, is very small, a small fraction of a

wave, but still time varying. We can then apply small angle approximations to the sine

and cosine terms of $\Delta\phi_j$ as defined in equations 4.30 and 4.31,

$$\cos(\Delta\phi_{Small}) \sim 1, \qquad 4.30$$

$$\sin(\Delta\phi_{Small}) \sim \Delta\phi_{Small}. \qquad 4.31$$

The small angle expressions afford us the opportunity to simplify the summations found

in equation 4.29 as shown in equations 4.32 and 4.33,

$$\sum_{j=1}^{N} \cos(\Delta\phi_j) \approx \sum_{j=1}^{N} 1 = N, \qquad 4.32$$

$$\sum_{j=1}^{N} \sin(\Delta\phi_j) \approx \sum_{j=1}^{N} \Delta\phi_j = \frac{N}{N} \sum_{j=1}^{N} \Delta\phi_j = N \cdot \overline{\Delta\phi}. \qquad 4.33$$

Here $\overline{\Delta\phi}$ is the average deviation of the combined beam from some common optimal

phase condition, ϕ_C, ($\overline{\Delta\phi}$ can also be thought of as the average phase error of the

coherently combined beam) and N is the total number of beams in the beam combination

system. Inserting the results of equations 4.32 and 4.33 into equation 4.29 we obtain a

new expression, 4.34, for the combined beam, Ec, **accurate only for small deviations of** **$\Delta\phi_j$,**

$$\frac{E_C(t)}{N \cdot E_o} = \begin{pmatrix} \left(\cos(\omega \cdot t) \cdot \cos(\phi_C) - \sin(\omega \cdot t) \cdot \sin(\phi_C)\right) \\ -\overline{\Delta\phi}\left(\cos(\omega \cdot t) \cdot \sin(\phi_C) + \sin(\omega \cdot t) \cdot \cos(\phi_C)\right) \end{pmatrix}. \qquad 4.34$$

By applying the trigonometric identities found in equations 4.10 and 4.35 to equation 4.34 we obtain a final expression for the combined beam, E_c, shown in equation 4.36,

$$\cos(\alpha + \beta) = \cos(\alpha)\cos(\beta) - \sin(\alpha)\sin(\beta), \qquad 4.10$$

$$\sin(\alpha + \beta) = \cos(\alpha)\sin(\beta) + \sin(\alpha)\cos(\beta), \qquad 4.35$$

$$E_C(t) = N \cdot E_o \left(\cos(\omega \cdot t + \phi_C) - \overline{\Delta\phi} \cdot \sin(\omega \cdot t + \phi_C)\right). \qquad 4.36$$

For informational purposes only, it is instructive to rewrite equation 4.36 in a different form by 'reversing' the mathematical small angle approximations, though not eliminating the small angle limitations on our expression for $E_c(t)$, defined in equations 4.30 and 4.31 and applying them to equation 4.36, as highlighted in red below in equation 4.37,

$$E_C(t) = N \cdot E_o \left(\cos(\omega \cdot t + \phi_C)\cos(\overline{\Delta\phi}) - \sin(\omega \cdot t + \phi_C)\sin(\overline{\Delta\phi})\right). \qquad 4.37$$

We can then rewrite the cosine expansion shown in equation 4.37 via equation 4.10 to obtain the final, *solely for informational purposes only*, form of the coherently combined electric field, E_c, shown in equation 4.38,

$$E_C(t) = N \cdot E_o \cos(\omega \cdot t + \phi_C + \overline{\Delta\phi}). \qquad 4.38$$

Here N is the number of electric fields that form the coherently combined beam (E_c), E_o is the common field amplitude of each individual beam, ω is proportional to the common optical frequencies of the combined beams, ϕ_c is the common phase state that each of the

N beams are aiming to achieve via phase locking, and $\overline{\Delta\phi}$ is the average, small angle, phase deviation of the combined beams with respect to ϕ_c. $\overline{\Delta\phi}$ is effectively the phase error of the combined beam as compared to optimal beam combination and is an excellent measure of the performance of a coherent beam combination system, assuming of course that it can be isolated from other terms found in equation 4.38.

4.2.2 Phase Error Measurement of Coherently Combined Beam

The purpose of the derivation above was to show that a coherently combined beam made up of N perfectly overlapped beams with common optical characteristics can be treated as a single beam, E_c, with field amplitude NE_o, frequency $(\omega/2\pi)$, and a phase state $\left(\phi_C + \overline{\Delta\phi}\right)$. It is then possible to plug the final expression of the combined beam, E_c, equation 4.38, into equation 4.5, and utilize the in-phase and quadrature data processing technique defined above to extract/measure the average phase deviation $\left(\phi_c + \overline{\Delta\phi}\right)$ as a function of time as shown in equation 4.39

$$\phi_c + \overline{\Delta\phi} = \tan^{-1}\left(\frac{Q\left(\phi_c + \overline{\Delta\phi}\right)}{I\left(\left(\phi_c + \overline{\Delta\phi}\right)\right)}\right) = \tan^{-1}\left(\frac{a_s}{a_c}\right). \qquad 4.39$$

Assuming, as we did before, that $\overline{\Delta\phi}$ fluctuates much faster than the common optical phase state of the N beams we can treat ϕ_c as a constant and trust that any time varying fluctuations in $\left(\phi_c + \overline{\Delta\phi}\right)$ can be attributed solely to $\overline{\Delta\phi}$, the optical phase error of the coherently combined beam.

It is important to reiterate that the discussion above, beginning directly after equation 4.36 and culminating in the final expression for the optical phase error $\overline{\Delta\phi}$ in equation 4.39, was intended only to provide understanding to the process of measuring the phase error of a coherently combined beam. None of the mathematical manipulations stated in the aforementioned text are required for phase behavior measurements of coherently combined beams to work properly.

4.3. Chapter Summary:

In this chapter the reader was introduced to a measurement technique capable of measuring the optical phase behavior of both single and coherently combined beams with respect to a phase stable, frequency shifted, reference beam. This author then derived the expressions for the demodulated components for both the in-phase (I) and quadrature (Q) components of the measured photocurrent proportional to the intensity fluctuations governed by interference between the beam of interest (single or multi-channel) and a frequency shifted reference beam. The reader was then provided with a final relationship relating the measured I and Q components of the photodetector signal to the optical phase behavior of the beam of interest as measured with respect to a phase stable, frequency shifted, reference beam. The chapters to follow will describe the experimental implementation and results of the phase behavior measurements described above.

Chapter 5.   Experimental Results: Phase Fluctuations in a 100W Fiber Amplifier

As stated in earlier chapters the primary goal of coherent beam combination is to increase the total optical output power of a laser system. For the purposes of this research, this is accomplished in 2 steps: first, by squeezing every possible photon out of a single fiber amplifier while maintaining such important optical characteristics as single frequency, narrow 'enough' linewidth, single transverse mode, stable polarization, and diffraction limited beam quality. This is a tall order to be sure and remains an ongoing area of research [7,11,15,17,18,23,61,67,68,69,70,71]. The second step is to coherently combine several high power fiber amplifier outputs into a single beam/output; just how many beams depends entirely on the application and needs of the user. For the remainder of this chapter we will focus on how step two, coherent beam combination, relates to step one via the phase behavior of a high power amplifier during amplifier turn on and steady state operation. We will focus our attention on the phase behavior of a 100W amplifier built by NuFern and utilized in the Air Force Research Laboratory Joint High Power Fiber Amplifier Test Bed [38,66,72]. With knowledge of the time varying phase behavior of the amplifier we gain an understanding of the performance parameters required of the phase control loop to maintain coherent combination of multiple high power fiber sources.

5.1. Review: Phase Noise Measurement Experimental Setup (Single Channel)
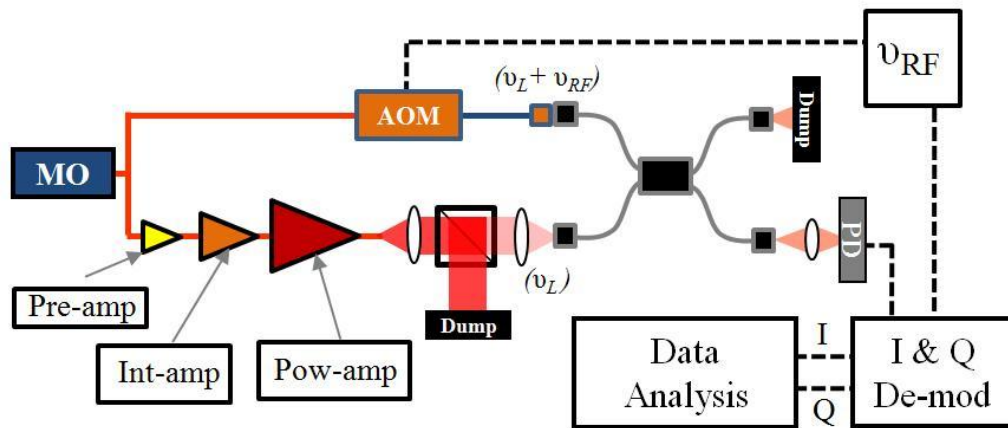
Figure 25: Experimental setup of time varying phase measurement of a single 100W NuFern fiber amplifier. The 3 stages of light amplification are denoted, in order of operation: pre-amplifier (pre-amp), intermediate amplifier (int-amp), and the power amplifier (pow-amp). The phase measurement technique shown in this figure is same as described in Chapter 4.

The experimental setup used to measure the phase error of a single high power amplifier is the same as outlined previously in Chapter 4. The setup begins, as shown to the left of Figure 25, with a single frequency, low power, polarized master oscillator (MO). Light from the MO is coupled into a fiber and then split two ways. One beam, the upper most fiber in Figure 25, feeds light into an acousto-optic modulator (AOM) where the light undergoes a frequency shift, υ_{RF}, of 80MHz. The light from the AOM is then fed into a 2x2 fiber splitter/combiner and used as the phase stable reference beam to measure the time varying phase changes of the high power amplifier against. The second, lower most fiber in Figure 25, feeds into pre-amplification stage where the light from the MO, 10-20mW, is amplified to 200-300mW. The light from the pre-amplifier is then feed into an intermediate amplification stage where it is then amplified to 8-10W. The light from the intermediate amplifier is then input into the final power amplifier where it is amplified to a maximum of approximately 100W while maintaining good polarization,

mode quality, single frequency, and narrow linewidth (~10kHz) characteristics [38,66,72]. To measure time varying phase changes of the high power fiber amplifier the output must be heavily attenuated before coupling into the 2x2 fiber splitter/combiner, as shown in Figure 25. Here, in the 2x2 splitter combiner, the light from the power amplifier is interfered with the phase stable, frequency shifted, un-amplified reference beam. The combined beam is then incident on a photodetector were a complex optical interference beat note is converted to a time varying electrical current i_{PD}. The time varying phase behavior of the high power fiber amplifier is then extracted from i_{PD} via coherent RF demodulation where the in-phase (I) and quadrature (Q) components of i_{PD} are measured and recorded for final analysis, as described in Chapter 4. The time varying phase difference, $\Delta\phi$, between the high power amplifier and the frequency shifted reference beam is calculated from I and Q via equation 5.1, as derived in Chapter 4,

$$\Delta\phi(t) = \tan^{-1}\left(\frac{Q(t)}{I(t)}\right).$$
5.1

Because the time varying phase changes in the high power amplifier are assumed to be much greater than phase fluctuations in the isolated, unamplified, phase stable, reference beam we can rewrite equation 5.1 as shown in equation 5.2,

$$\Delta\phi(t) = \phi_{PA}(t) - \phi_R \approx \phi_{PA}(t) = \tan^{-1}\left(\frac{Q(t)}{I(t)}\right).$$
5.2

Here ϕ_{PA} is the time varying phase of the power amplifier, and ϕ_R is the relatively constant phase state of the frequency shifted reference beam. Because ϕ_R varies much more slowly than ϕ_{PA} we will treat it as constant and equal to zero as shown in equation 5.2.

5.2. Basic Design of Power Amplifier
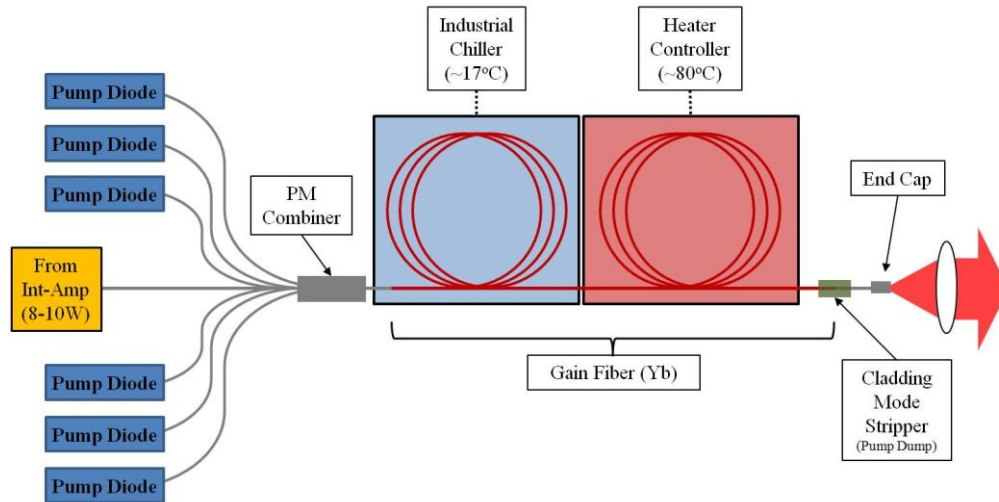
Figure 26: Schematic of a co-pumped 100W fiber amplifier built by NuFern. SBS suppression accomplished via the introduction of a thermal gradient in the gain fiber with hot and cold fiber spools.

Before delving into measurement results it is necessary to describe the basic layout and workings of the NuFern power amp as much of the phase behavior is the result of heating and cooling of components in said amplifier. Shown in Figure 26 the power amplifier begins with an input from the intermediate amplifier where 8 to 10 watts of 1064nm light is delivered to the double clad Ytterbium (Yb) doped fused silica gain fiber via the seed/core feed through leg of a 6x1x1 pump combiner. The seed light is intended to coerce the power amplifier to amplify only the wavelength and transverse mode of the seed while suppressing all others. The gain fiber is also (inner) cladding pumped with 976nm light, from six 50W quasi-wavelength stabilized pump diodes, via the pump delivery legs of the 6x1x1 combiner. The pump light induces a population inversion in the Yb doped gain fiber which subsequently amplifies the 1064nm seed light. It is important to notice in Figure 26 that the gain fiber is spooled on two separate fiber spools with approximately half the fiber length in each spool (~5m/ea.). Each spool is held at a

117

different temperature with the cold spool operating at ~17 $^{\circ}$C and the hot spool at ~80 $^{\circ}$C. In principle, the two spools introduce a thermal gradient along the length of the gain fiber which aids in the suppression of Stimulated Brillouin Scattering (SBS) [19,70,73,74], the primary limitation in the power scaling of fiber amplifiers to much higher powers. The amplified 1064nm light, and any unused 976nm pump light, then passes through a cladding mode stripper where the remaining pump light, and any stray 1064nm light found in the inner cladding of the gain fiber, is removed. The amplified 1064nm core light then feeds through to a fiber end cap and diverges to a collimating lens. After exiting the lens the collimated light is attenuated and used, for the purposes of this discussion, in measuring the phase error of the fiber amplifier as shown in Figure 25.

5.2.1 Phase Changes Due to Quantum Defect Heating

Looking at Figure 26 it's possible to make an educated guess at the primary sources of phase disturbances the power amplifier will likely encounter. The first thing to realize is that there is no such thing as a perfect optical to optical conversion in an optical gain medium (at least this author knows of no such gain material). At a very minimum we expect the presence of quantum defect heating due to the loss of energy in converting 976nm photons into lower energy 1064nm photons. Therefore, the harder we pump the gain medium - or more accurately, the more pump photons absorbed and reemitted by the gain medium - the more quantum defect heating we can expect in the gain fiber. The heating of the gain fiber is controlled via conductive and convective cooling of the fiber but for the heat to escape the core it must first radiate from the source of the heat, most notably the optical/material interactions in the core of the gain medium, through the inner and outer cladding of the optical fiber, through a protective buffer material and then

118

transfer into either of the cooling spools or the surrounding air. Suffice it to say that the core never escapes quantum defect heating when optically pumped and will therefore impose an optical phase change to the amplified beam, either through thermal expansion of the gain fiber ($\alpha_{\Delta T} = 5.5 \times 10^{-7}$ $^{\circ}$C^{-1}, for fused silica [75]) and/or the dependence of the index of refraction of the fiber on temperature ($\alpha_{\Delta n} = 1.3 \times 10^{-5}$ $^{\circ}$C^{-1}, for fused silica [75]). Because $\alpha_{\Delta n}$ is approximately 25 times greater than $\alpha_{\Delta T}$ we will treat the thermal dependence of the index of refraction the fiber as the dominating effect and ignore the coefficient of thermal expansion of the material.

5.2.2 Phase Changes Due to Temperature Controller Errors

Another likely source of phase changes in the power amplifier are the control errors of the industrial chiller, and hot plate, temperature controllers used in the power amplifier. Temperature fluctuations of less than 1°C, acting on a relatively long optical fiber, introduce easily measureable phase changes. For example, if we have a 1m gain fiber, and apply a uniform 1°C temperature change along the full length of the fiber, we can expect an approximately 20μm change in optical path length (ΔOPL) of the fiber, as governed by equation 5.3,

$$\Delta OPL = n \cdot l \cdot \alpha_{\Delta n} \cdot \Delta T.$$

5.3

Here n is the index of refraction of the gain fiber (n $\approx$ 1.45, for Fused Silica), l is the length of the gain fiber ($l = 1$m), $\alpha_{\Delta n}$ is the coefficient of the change in the index of refraction with temperature for fused silica ($\alpha_{\Delta n} = 1.3 \times 10^{-5}$ $^{\circ}$C^{-1}), and ΔT is the temperature change applied to the full length of the fiber (ΔT = 1°C). For an optical wavelength of approximately 1μm, a 20μm change in the optical path length, ΔOPL, correlates to a change in optical phase of 20 waves, or 40π Radians. Such a phase change

applied to a beam, and interfered with a stable, unchanging, reference beam, would

produce 20 cycles between constructive and destructive interference (20 fringes), as

governed by equation 3.1, an easily measureable quantity (if change is slow enough this

effect can be seen by the human eye with the aid of an IR viewer).
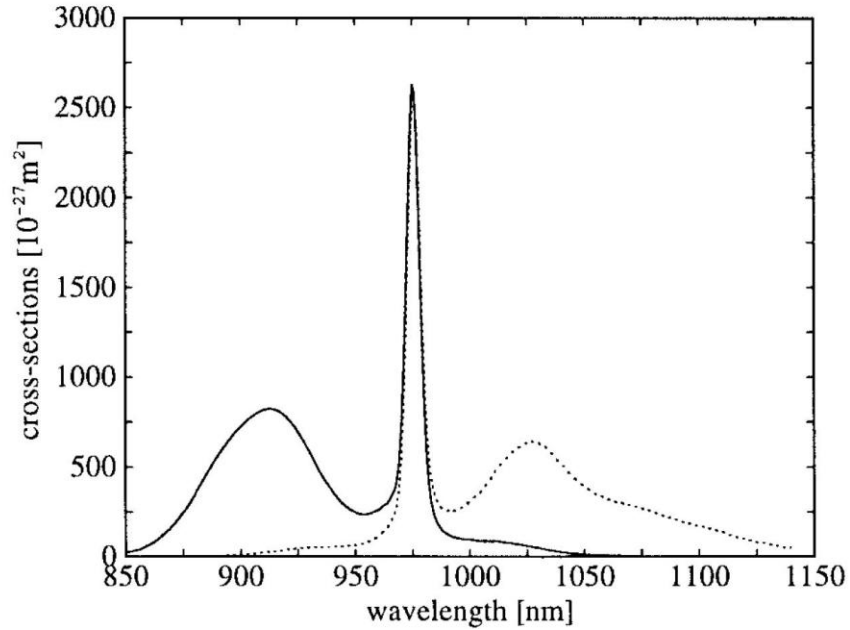
Figure 27: Absorption (solid line) and emission (dotted line) spectrum of Ytterbium (Yb) doped fused silica [76]. Note absorption and emission peak at ~975nm.

Though not expressly stated in the text above, the quasi-wavelength stabilized pump

diodes are just that, 'sort-of-wavelength stabilized' pump modules. As it turns out the

wavelength of the pump diodes used in the amplifier shown in Figure 26 are controlled

primarily by temperature. If one can fix the temperature of the pump diode then,

theoretically, its wavelength will be fixed and remain unchanged over time. In practice

these pump diodes are cooled with the same chiller water used to set the temperature of

the power amplifier cold spool shown in Figure 26. Said chiller water comes from a large

industrial chiller with a temperature control resolution of 1 to 2 $^{\text{o}}$C. This might not seem

120

like much of a temperature variance but the wavelength of the pump diodes used varies on the order of 0.4nm per 1 $^{\circ}$C. If we take a look at the absorption spectrum of an Yb doped fiber, shown in Figure 27 [76], we see that small changes in pump wavelength equates to a relatively large change in pump absorption when centered on or near the 975nm absorption line. A 1-2 $^{\circ}$C change in temperature of the pump diodes equates to a 0.4-0.8nm shift in pump wavelength. This correlates to ~2% to ~4% change in pump absorption, respectively, when centered on 976nm, the set center wavelength of the pump diodes. Such wavelength variations can lead to a slew of time varying temperature changes in the power amplifier. For example, if the pump light red shifts from 976nm (increases in wavelength) the absorption in the fiber goes down and will reduce quantum defect heating in the gain fiber, and lower the total output power of the amplifier (assuming constant input pump power). This same red shift will also lead to increased heating at the cladding mode stripper, shown in Figure 26, as more unused pump light will have to be removed after passing through the gain fiber. As it is unlikely that these two temperature changes will balance each other out, time varying, thermally induced, phase changes in the power amplifier will occur due to the time varying wavelength shifts of the pump diodes.

5.2.3 Phase Changes Due to Heating of Fiber Splices

It is worth noting that a monolithic fiber amplifier is comprised of a series of fiber components fusion spliced together. A fusion splice is where one fiber is essentially melted, tip to tip, to another fiber, creating a continuous waveguide for light to pass through. At the location of a fusion splice it is unreasonable to expect perfect uniformity due to differing dimensions in, or misalignment of, the two optical fibers being spliced

121

together as well as variations in optical index of refraction between the un-doped passive

delivery fiber and Yb doped gain fiber. Scattered light from the core and/or cladding at

these splice locations, due to non-uniformities in the fusion splice and scattering from Yb

atoms, will then be absorbed by the buffer material applied to protect the splice. This

absorption leads to heating, and in some cases failure, of the fusion splice. Said heating,

just as before, can lead to optical phase changes in the final output beam of the power

amplifier; though it is unlikely that these localized phase changes will be primary

contributors to the total phase drift/change of the final output beam as the heating occurs

over a relatively small percentage of the entire length of the fiber. For example, if the full

length of a 10m gain fiber undergoes an average change in temperature, ΔT, of only 5 $^{\circ}C$

(not an unreasonable value for 100W class fiber amplifier with 10 meters of gain fiber),

the change in optical path length, ΔOPL, will be approximately 950μm. If fiber

surrounding a fusion splice undergoes a 25 $^{\circ}C$ temperature change (also not an

unreasonable value for 100W class fiber amplifier), and acts only on a 2 cm length of

fiber (localized heating due to active cooling of fiber splice), the change in optical path

length will be ~9μm, or approximately 1% of the change introduced to heating the entire

length of fiber by only a few degrees. Though heating of fiber splices is not insignificant,

we recognize quantum defect as the dominate cause of phase fluctuations in the power

amplifier and will treat it as such in the discussions to follow.

5.3. Results: Background Phase Behavior Measurements

The data shown below in Figure 29 is representative of the time varying phase

behavior of the amplifier chain shown in Figure 25 with only the first two stages of

amplification operational. The power amplifier was left off in an effort establish the

background noise level and to determine the measurement resolution. Ideally, each stage

of amplification would remain off during background measurements but, in practice, light

from the MO in Figure 25 is so heavily attenuated, due to absorption and scattering losses

in the Yb doped gain fiber of the amplifier chain, before exiting the output of the power

amplifier that the first two stages of amplification were required to provide a large

enough optical signal to measure the phase behavior. Therefore, the pre and intermediate

amplifiers were each allowed to reach steady state operation before the data in Figure 29

was taken. Said data can then aid in isolating background phase disturbances from those

caused solely by the power amplifier as all systems (heating, cooling, etc.) were

operational during these measurements.
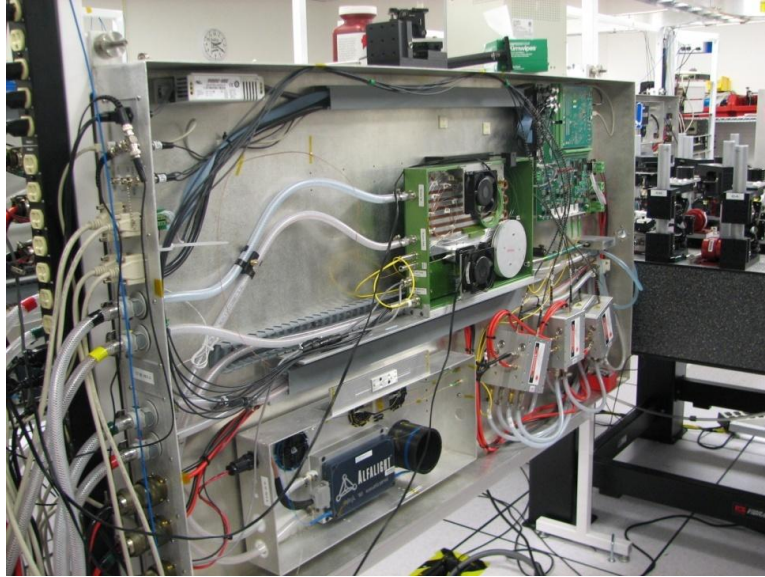
Figure 28: 1 of 16 100W power amplifier trays in the AFRL high power fiber amplifier test bed. Components in the green housing, towards the center of the image, form the NuFern power amplifier. Pump diodes housed in the stacked metal housings in the bottom right of the amplifier tray pump the Yb gain fiber in the NuFern power amplifier. Components in the rectangular aluminum tray to the bottom left of the image (including component labeled *Alfalight*) compose the intermediate amplifier. The pre amplifier mentioned in the text is not shown in this picture. Light from pre-amplifier is delivered to intermediate amplifier via the horizontal blue fiber patch cable to the left of the image (pre-amplifier is actually located in a corner of the room and is connected via 20m fiber patch cable).

It is important to note that the experimental diagram shown in Figure 25 is a very simplistic representation and does not provide the reader with a sense of scale for the single amplifier phase behavior measurements. The experiments were indeed run in a manner consistent with that shown in Figure 25 but there was approximately 50 meters of optical fiber in both the reference and amplifier beam paths of the experiment shown in Figure 25. The lengths of fiber involved were governed primarily by the requirements of the different stages of amplification (lengths of gain fiber required to generate the desired output) as well as the physical dimensions of the room. Imagine sixteen power amplifier trays, single tray shown in Figure 28, distributed evenly, approximately 4 feet apart, along two opposing sides of an optical table (lengthwise). Each of the sixteen amplifiers

is connected to its individual pre-amplification stage, via a 20m fiber patch cable, housed in one corner of the room (the MO that seeds all 16 pre-amplifiers is located in the same corner). Due to the sheer length of the fiber/environment interaction involved one would expect a considerable amount of phase noise found in both the reference and amplification legs of the experimental setup. In an effort to minimize the phase differences between the amplification chain (with power amplifier turned off) and the reference beam, the reference fiber was run right alongside the amplifier chain fiber wherever possible, though not subject to the heating or cooling implements of power amplifier (there is no active cooling of the fiber in the pre and intermediate amplification stages). This way, ideally, the reference fiber would experience the same environmental phase disturbances (mechanical vibrations, etc.) as the fiber found in the amplification chain, minimizing their effect on the phase behavior measurements. Remember that the setup shown in Figure 25 measures the difference in phase between the amplifier chain and the reference beam. Therefore if both the reference and amplified legs experience the same environmental phase disturbances then the measured phase difference will be governed entirely by phase disturbances acting only on the amplification chain (heating, cooling, etc.). In reality, it is impossible to perfectly match the phase errors of the reference leg and the amplification chain over such long distances but said efforts provided a reduction in measured environmental phase noise of nearly a factor of five, with all external systems operational (heating, cooling, fans, etc).

5.3.1 Phase Fluctuations Resulting From Industrial Chiller
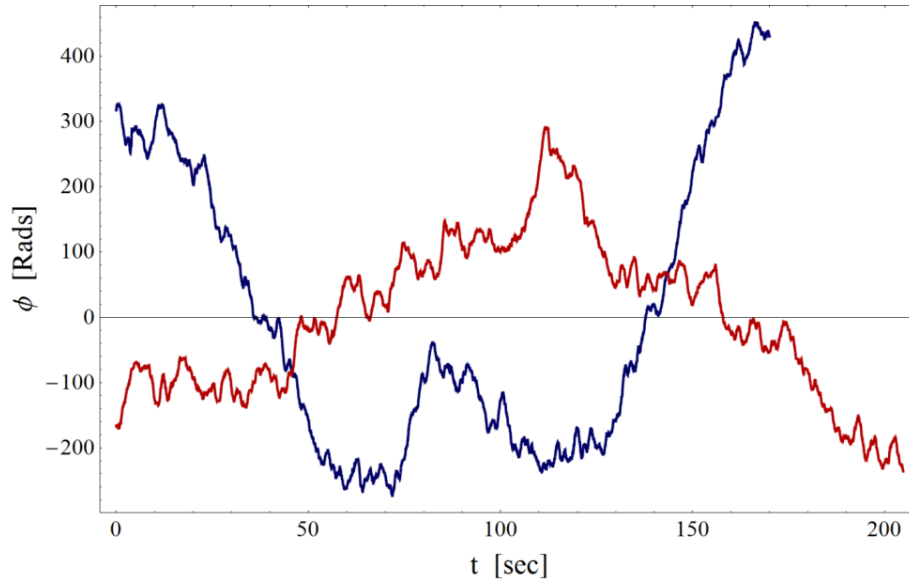
Figure 29: Time varying background phase behavior of the high power amplifier chain. Pre and intermediate amplifiers in steady state operation with power amplifier turned off. Shown are two independent data sets with phase fluctuations primarily dependant on environmental disturbances and temperature cycling of the industrial chiller.

The data shown in Figure 29 represents the background phase behavior of the high power amplification chain shown in Figure 25, with the power amplifier turned off (heating and cooling elements still on). As it turns out the very slow peak to peak phase fluctuations, shown in Figure 29, of 530-730 radians over the full 200 second data acquisition time can be attributed to slow temperature variations in the industrial chiller water used to cool components in the power amplifier. To demonstrate this we first have to relate $\Delta\phi$ to the change in optical path length, ΔOPL, via equation 5.4,

$$\Delta OPL = \frac{\Delta\phi}{2\pi} \cdot \lambda.$$

5.4

where λ is the wavelength of the light guided in the fiber, $\lambda = 1.064\mu m$. We can then plug the expression found in equation 5.4 into equation 5.3 and solve for the corresponding change in temperature, ΔT, shown in equation 5.5,

$$\Delta T = \frac{\Delta\phi \cdot \lambda}{2 \cdot \pi \cdot n \cdot l \cdot \alpha_{\Delta n}}.$$
5.5

Utilizing the material properties of fused silica defined above (n_{FS} = 1.45, $\alpha_{\Delta n}$ = 1.3x10^{-5} ^{o}C^{-1}), and a chiller/fiber interaction length, l, of 5m (5m of the 10m gain fiber is on the cold spool connected to the industrial chiller), for measured phase changes, $\Delta\phi$, of 530-730 radians, the corresponding temperature change, ΔT, is approximately 1-1.3 ^{o}C, in excellent agreement with the specified temperature resolution of the industrial chiller defined above (1-2 ^{o}C). This result provides us with two important pieces of information. First, that the phase error measurement is indeed working and sensitive enough to measure relatively small temperature changes along the length of the power amplifier gain fiber. The second is that our effort to isolate the reference leg of the phase error measurement was relatively successful. Just how successful will be discussed later on.

5.3.2 Phase Fluctuations Resulting From Hot Spool Heater

A closer look at the data in Figure 29 shows a low amplitude, approximately 10-15 second per cycle, phase oscillation riding along the broader phase behavior governed by the industrial temperature controller discussed above. With an amplitude of approximately 50 radians, peak to peak, this phase change corresponds to a temperature change of approximately 0.1 ^{o}C. As it turns out the temperature controller for the heated spool in the power amplifier, shown in Figure 26, is specified by the manufacture to have a control resolution of approximately 0.1 ^{o}C, in excellent agreement with our phase behavior measurement. Said measurement both quantifies the effect of temperature variations in the Yb gain fiber caused by temperature changes in the hot spool heater controller and demonstrates that the phase behavior measurement described above is

easily capable of measuring temperature changes of $1/10^{th}$ of $1\ ^oC$ along a 5m section of gain fiber.

5.3.3 Resolution of Single Amplifier Phase Error Measurement
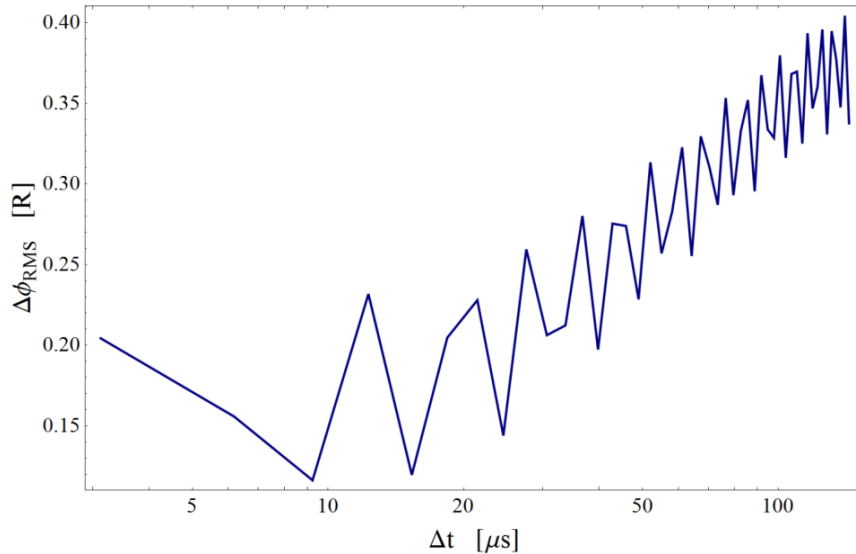
Figure 30: RMS phase error structure function for the data shown in blue in Figure 29. Left most data points provide an excellent estimate of the phase behavior measurement resolution of a single high power fiber amplifier in the AFRL fiber test bed. Typical errors of 0.2 radians were observed for a nearly $\lambda/30$ measurement error.

The goal of previous sections was to demonstrate the accuracy of the phase error measurement shown in Figure 25 and quantify the effect of hot and cold spool temperature fluctuations on the power amplifier gain fiber. Along with knowledge of the accuracy of a measurement it is also important to quantify its resolution. Because the measurement shown in Figure 25 is an interferometric measurement technique it, just like the power amplifier, is also highly sensitive to environmental disturbances (mechanical, thermal, etc) which can greatly affect the resolution of such a measurement. In an effort to establish the measurement resolution, including unavoidable environmental phase disturbances, of the phase error measurement the RMS phase difference structure

128

function is introduced. Shown in equation 5.6, the RMS phase difference as a function of

a fixed time difference, $\Delta\phi_{RMS}(\Delta t)$, or structure function, is calculated,

$$\Delta\phi_{RMS}\left(\Delta t\right)=\sqrt{\left\langle\left(\phi\left(t+\Delta t\right)-\phi\left(t\right)\right)^2\right\rangle_t}.$$ 5.6

Essentially what is being determined here is the RMS phase difference of the system

between all data points separated by some time, Δt. For short Δt, much shorter than the

expected time scale of the environmental phase disturbances, we can treat $\Delta\phi_{RMS}(\Delta t)$ as a

measure of the measurement error of the entire phase measurement system. Shown in

Figure 30 is the RMS phase structure function, $\Delta\phi_{RMS}(\Delta t)$, plotted as function of the time

difference between data points between 2µs and 144µs. We see that for the smallest of

Δt's, 2-20µs, the RMS structure function consistently shows RMS values near 0.2 radians

($\sim\lambda/30$). This therefore establishes a measurement resolution of the entire phase error

measurement of approximately $1/30^{th}$ of an optical wave. For $\lambda \approx 1$µm, the operating

wavelength of the amplifier chain previously described, the optical phase length change,

ΔOPL, measurement resolution is approximately 30nm. As we will see below such

resolution is more than adequate to resolve the phase behavior of an operating 100W

power amplifier.

5.4. Results: Turn On & Steady State Phase Behavior of a 100W Fiber Amplifier

The primary goal of the experiments about to be described is to determine the

time varying phase behavior of the power amplifier during turn on and steady state

operation. During the measurements described below the pre and intermediate stages of

amplification were already on, and in steady state operation (same as done for the

background measurements described above), long before 976nm pump light was

introduced to the power amplifier. The power amplifier was brought up manually by stepping up the drive current on the pump diodes via a LabView control program. During the two stages of operation I and Q data were acquired for later analysis as shown in Figure 25.
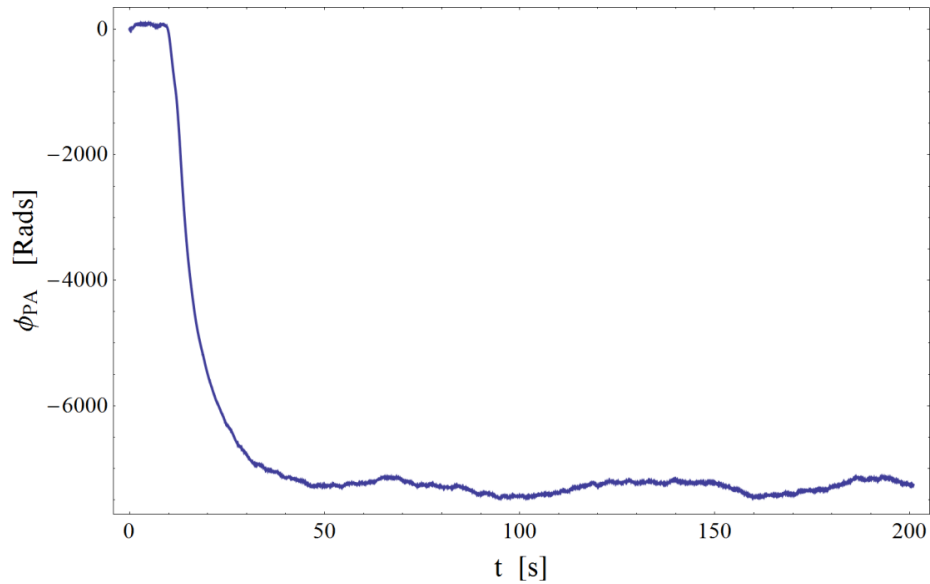
Figure 31: Time varying phase behavior of power amplifier in the 100W amplifier chain shown in Figure 25. ϕ_{PA} exhibits phase retardation (negative values) primarily due to an increase in temperature of the power amplifier gain fiber resulting in an increase in the refractive index of the gain medium.

The data shown in Figure 31 represents the time varying phase behavior exhibited by the power amplifier during turn on and steady state operation. For the first few seconds (~4s) the power amplifier remained off (no pump light introduced to the gain fiber). At approximately 4 seconds into the data acquisition the power amplifier was manually turned on, as evidenced by the 'first' sharp change in phase seen in Figure 31, and brought up to 100W operation. After 40-45 seconds the amplifier appears to reach steady state operation and remains there for the duration of the measurement.

5.4.1 Phase Behavior During Power Amplifier Turn On
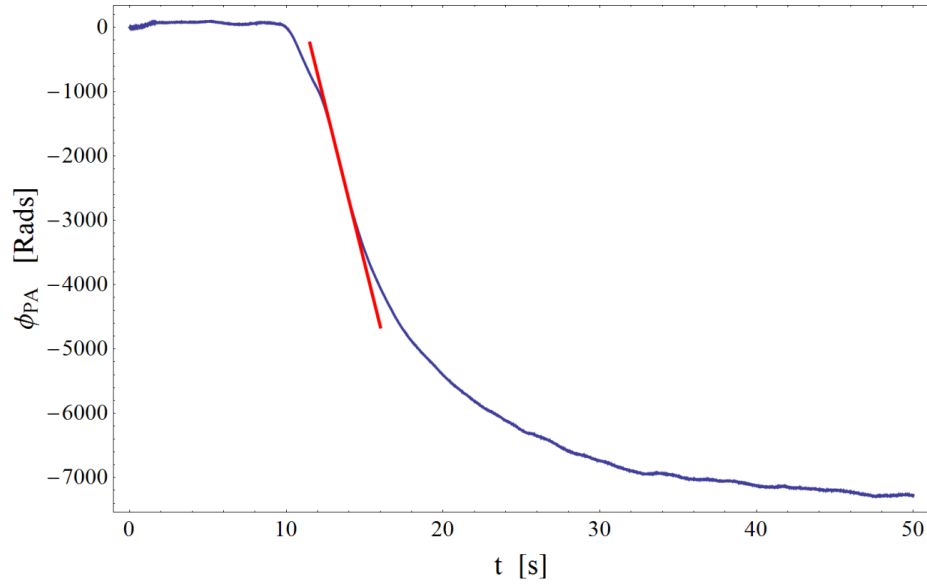
Figure 32: Phase behavior of power amplifier as it reaches steady state from a cold turn on. This figure represents the first 40s of data shown in Figure 31.

Looking at Figure 31 and Figure 32 it becomes clear that the phase behavior of the power amplifier does not reach a steady state until about 40s after the amplifier is turned on. From a beam combination perspective this time frame is possibly the most important as it is clear that the most dramatic changes in the phase behavior of the power amplifier, $\frac{d\phi_{PA}}{dt}$, occur during this window. The primary culprit of the phase excursion shown in Figure 32 is quantum defect heating of the double clad Yb gain fiber in the power amplifier, shown in Figure 26, originating from the introduction of pump light to the optical gain medium. The highest rate of change in the optical phase state, or optical path length, of the power amplifier occurs about 2 seconds after the amplifier turn on sequence began, $\left(\left. \frac{d\phi_{PA}}{dt} \right|_{MAX} = 950 \, \frac{R}{s} \approx 150 \, \frac{\lambda}{s} \right)$. Notice the sudden 'bump' or change in the measured phase state of the power amplifier directly proceeding $\left. \frac{d\phi_{PA}}{dt} \right|_{MAX}$ (not to be

131

confused with the sudden change in phase when the power amplifier was initially turned on, as discussed above). This is due to how the power amplifier was brought up to power from a cold start and will be described below.

Each of the 16 power amplifiers in the AFRL High Power Fiber Test Bed were designed with safety of the amplifier in mind. To protect the pump diodes, and subsequently the Yb doped gain fiber, from sudden electrical current spikes a simple RC circuit was implemented to limit the rate at which the power supply can ramp up the drive current to the 976nm pump diodes. The six pump diode modules shown in Figure 26 were also divided into two sets of three with each set operating on its own power supply and software controller. In the test bed control software the controllers for each pump set were left independent of the other giving the user the ability to turn three, or all six, pump diodes on at a given time as well as control of the total drive current to each pump diode set (0-40A). Said controls allow the user to vary the output power of the power amplifier between 10 and 100W.

With the pump module controls as they are we can see their effects on the optical phase state of the power amplifier in Figure 32. The user must step up the total current for each set of pump modules in the power amp from 0 to 40A in increments of 5A and each pump set must be brought up independently of the other. Therefore, the sudden increase in $\frac{d\phi_{PA}}{dt}$ at approximately 6s into the data acquisition time (~2s after amplifier turn on sequence began) is due to the introduction of the second set of pump diodes for a total of

six diodes pumping the gain medium. Had we been able to introduce the pump drive

current in a more 'step function' like way we would expect a larger $\left.\dfrac{d\phi_{PA}}{dt}\right|_{MAX}$.

From a beam combination perspective $\left.\dfrac{d\phi_{PA}}{dt}\right|_{MAX}$ provides a measure of the phase

locking control loop performance required in order to maintain optical phase locking with

a given amplifier. If the phase locking control loop is unable to correct for the maximum

rate of phase change seen in Figure 32, $\left(\left.\dfrac{d\phi_{PA}}{dt}\right|_{MAX} = 950\,\dfrac{R}{s} \approx 150\,\dfrac{\lambda}{s}\right)$, then during that

time period a beam combination system, utilizing a number of the amplifiers described

above, cannot coherently combine, eliminating all expected coherence benefits. This may

or may not be a big concern depending on the application. If the user is willing to wait for

the system to reach steady state, in this case up to ~40s, before expecting an optimized

output of the coherent beam combination system then a slower phase controller to correct

only the steady state phase fluctuations will likely work fine. If the user requires that the

system be coherently combined from the moment it turns on, through steady state

operation, then a higher control loop bandwidth will likely be required; though the

response time requirement of the phase control loop may be less than implied by

$\left.\dfrac{d\phi_{PA}}{dt}\right|_{MAX}$, as discussed in the following text.

For the sake of argument let's say that a phase control loop capable of correcting

for the phase changes seen during the turn on stage of power amplifier operation is not

available; all is not yet lost. The measurement and data described above represents the

phase state of a single power amplifier, as compared to a phase stable reference beam, as

a function of time. If we wanted to phase lock just one power amplifier, not yet turned on, to an amplifier that has already reached steady state operation then yes, we would need a fast phase control loop to maintain coherent beam combination between the two beams. Instead, if each power amplifier in the coherent beam combination system is the same (common output power etc.), and each amplifier was turned on at the same time, and brought up to power at the same rate, then the rate of change of the difference in phase, $\Delta\phi$, between each of the beams to be combined would be much slower - ideally non-existent. Because a coherent beam combination system does not work to restore a given amplifier to its original phase state (fixed reference) but instead works to correct the phase difference between a given power amplifier with respect to all other amplifiers in the system, regardless of the shared time varying phase state (floating reference), the required correction bandwidth of the control electronics will be much lower.
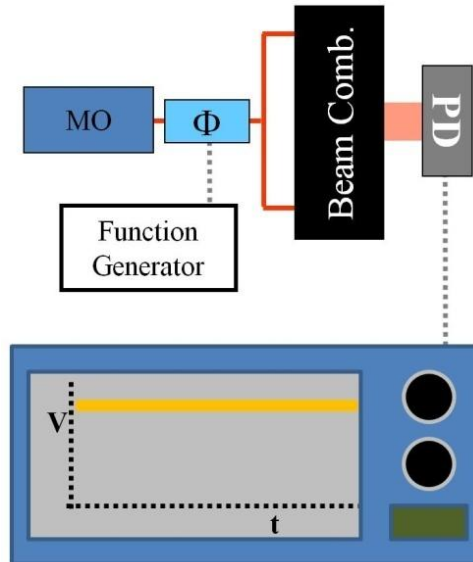
Figure 33: Beam combination thought experiment: Light from the master oscillator, MO, is arbitrarily phase modulated and split into two identical beam paths. The 2 beams, both identically phase modulated, are then recombined and incident on a photodetector. Note that regardless of phase changes applied to the phase modulator the intensity measured at the photodetector will remain constant if the optical path lengths of the two beams remain identical, assuming no independent phase disturbances on either of the two beams.

To drive this point home it is informative to do a simple thought experiment. Imagine the scenario shown in Figure 33. The output of a single frequency master oscillator passes through a single phase modulator and then splits into 2 beams. The 2 beams propagate – as drawn, in fiber – some distance, perfectly equal for both beams, and are recombined via a 'black box' ideal beam combiner. Assuming there are no external phase disturbances anywhere in the system, regardless of the time varying phase modulation applied to both optical beams, the intensity measured at the photodetector will remain constant and optimized (constructive interference). This happens because each beam, originating from a common source, traveling separate but equally long beam paths, recombined and interfered at the photodetector, have common and equal, though time varying, phase states at the photodetector. Since the phase difference between the two beams is always zero the two beams constructively interfere and continue to do so as

135

long as the optical path lengths of the two beams remain the same, regardless of the time

varying phase changes applied to the original source beam, as governed by equation 3.1.

5.4.2 Phase Behavior during Steady State, 100W, Operation of Power Amplifier

5.4.2.1 Effects of Industrial Chiller on Power Amplifier Steady State Operation
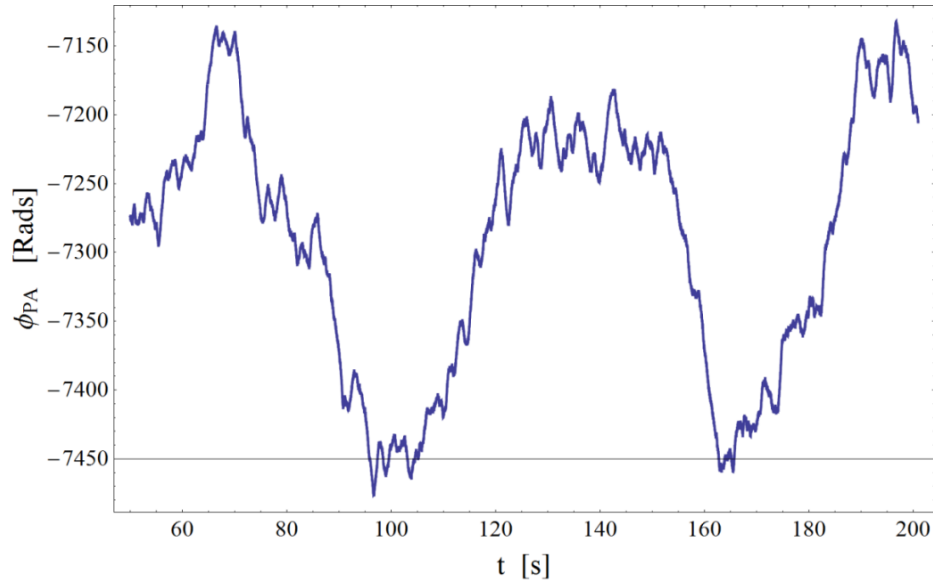
Figure 34: Phase behavior of the NuFern 100W power amplifier after reaching steady state operation from a cold turn on. This figure represents the amplifier operation after the 50s turn on period shown in Figure 31.

The data shown in Figure 34, the 50-200 second window of Figure 31, represents

the phase behavior of the power amplifier during steady state operation (at 100W). Just

like the background measurement described above the power amplifier experiences broad

cycles in optical phase, due to the temperature cycling of the industrial chiller, with much

lower amplitude environmental phase disturbances riding along on top of it. Notice that

the peak to peak amplitude during steady state operation of the power amplifier shown in

Figure 34, $\Delta\phi_{PA}$ [p-p] = ~350R, is significantly lower than the background measurements

shown in Figure 29, $\Delta\phi_{BKND}$ [p-p] = 530-730R. It is important to note that the data shown

in these two figures are only intended to provide the reader a sense of the typical time

136

varying phase fluctuations in the power amplifier for their respective operating conditions (power amplifier on or off). When looking at multiple data sets taken during experimentation it becomes clear that the peak to peak amplitude of the phase changes, due to fluctuations in the cooling temperature of the power amplifier cold spool, are anything but constant as is discussed below.

	$\Delta\phi_{P-P} / \Delta T$ (Background)	$\Delta\phi_{P-P} / \Delta T$ (Steady State, 100W)
1	410R / ~0.7 ^{o}C	770R / ~1.4 ^{o}C
2	730R / ~1.3 ^{o}C	460R / ~0.8 ^{o}C
3	530R / ~0.9 ^{o}C	350R / ~0.6 ^{o}C
4	550R / ~1.0 ^{o}C	610R / ~1.1 ^{o}C
Avg.	**555R / ~1.0 ^{o}C**	**548R / ~1.0 ^{o}C**

Table 4: Measured peak to peak phase changes, $\Delta\phi_{p-p}$, and corresponding fiber temperature changes, ΔT, during background and steady state power amplifier operation. Note that the average phase and temperature changes during background and power amplifier on measurements are nearly identical. (Data acquisition time of each data set: ~200s).

The data shown in

Table 4 is representative of the peak to peak phase behavior of the power amplifier during background measurements and during 100W steady state operation. It is clear that there are significant differences in the peak to peak phase and temperature behavior between the four data sets analyzed for each operating condition. If we take the average of the values listed in

Table 4 we see that the mean phase fluctuation, $\Delta\phi$, for both the background and 100W measurements are in excellent agreement, $\Delta\phi_{BKND} \approx \Delta\phi_{PA} \approx 550R$. When we relate the average measured phase change to its corresponding temperature change, via equation 5.5, we find that ΔT is approximately 1.0 ^{o}C, again in excellent agreement with the manufacturer specified temperature resolution of the industrial chiller used to cool components in the power amplifier, $\Delta T_{Chiller} = 1$-2 ^{o}C.

It is important to also notice that rate at which the phase cycles in Figure 34 (broad cycles due to temperature cycling of the industrial chiller) is approximately 3x

faster than is seen in the background measurements of Figure 29. This effect is caused by the greater temperature load on the chiller during power amplifier operation. As discussed previously, when pump light is introduced to the power amplifier gain fiber quantum defect heating occurs. The heat formed in the core conducts through the inner and outer cladding of the gain fiber and into the protective buffer material. The buffer material is either in contact with the hot or cold fiber spool where, during 100W operation, the fiber is cooled. The portion of the fiber in contact with the cold spool (~5m) transfers its heat to said spool and into the cooling water (~17 ^{o}C). Over time the cooling water heats up and must be re-cooled by the control unit. Because considerably more heat is introduced to the coolant during power amplifier operation the temperature controller must 'kick in' more often (cools only when temperature is greater than set threshold value), thus the increased rate in phase/temperature cycling during 100W operation, when compared to background phase fluctuations.

5.4.2.2 Effects of Hot Spool Temperature Controller on Steady State Operation

Just like during the background phase behavior measurements, during steady state 100W operation, we observe a low amplitude phase oscillation riding along the broader phase behavior governed by the industrial temperature controller. With an amplitude of approximately 50 radians, peak to peak, this phase change corresponds, again, to a temperature change of approximately 0.1 ^{o}C, in excellent agreement with the temperature control resolution of the power amplifier hot spool, discussed above. This time, just as with the industrial chiller temperature cycling time, we see a significant decrease in the cycling time of the temperature controller, now approximately 5 seconds, down from 10-15 seconds observed during background measurements. The decrease in temperature

cycling time has to do with the hot spool in the power amplifier actually cooling the power amplifier gain fiber during amplifier operation. During the background measurements, with the gain fiber un-pumped, the heater simply combated room temperature cooling to keep the fiber at ~80 ^{o}C. Once the 976nm pump light was introduced to the gain fiber quantum defect heating heated the fiber beyond the 80 ^{o}C background temperature. The temperature controller of the hot spool is capable of sensing this increase in temperature and adjusted accordingly by decreasing the hot spool temperature. Also, just like with the industrial chiller, the increased heat load, from quantum defect heating, translates to faster changes in temperature of the cooling mechanism forcing the temperature controller of the hot spool to 'kick in' more often when the temperature of the fiber goes above some threshold temperature value (~80.1 ^{o}C), thus decreasing the temperature cycling time from 10-15 seconds to ~5 seconds.

5.5. Required Control Loop Bandwidth to Correct For Phase Fluctuations During Amplifier Turn On:

As is clear from the discussion above the highest rate of change in the phase state of the power amplifier occurs shortly after the amplifier is initially turned on, as seen in Figure 32. From a coherent beam combination perspective, and in relation to the primary topic of this dissertation, the question that needs to be addressed is whether or not the LOCSET phase control electronics is capable of phase locking during this window of time. As discussed previously, if all amplifiers in the beam combination system are identical and brought up to power at the same time and rate then the phase differences between them will be minimal. For the sake of this discussion let's assume a worst case scenario where each amplifier is brought up to power after the previous amplifier has reached steady state. Our discussion will then be limited to a two amplifier situation, with one amplifier

in steady state while the second amplifier is brought up to power from a cold turn on, assuming that once all previously turned on amplifiers have reached steady state, and are coherently combined, they can be treated as a single unit.

The scenario described above is essentially the same as found in the phase error measurement of a single amplifier discussed in section 5.1. Only this time the reference beam is operating at a much higher power and is no longer frequency shifted. If we treat the reference beam as the amplifier already in steady state operation, and then bring the second amplifier in the beam combination system up to power we can expect time varying phase differences similar to that shown in Figure 32. In Figure 32 we see that the maximum rate of change in the optical phase is around 950 R/s. The question then becomes, for the purposes of this dissertation, whether or not the LOCSET phase locking electronics can operate at, or beyond, this rate, and will be discussed below.
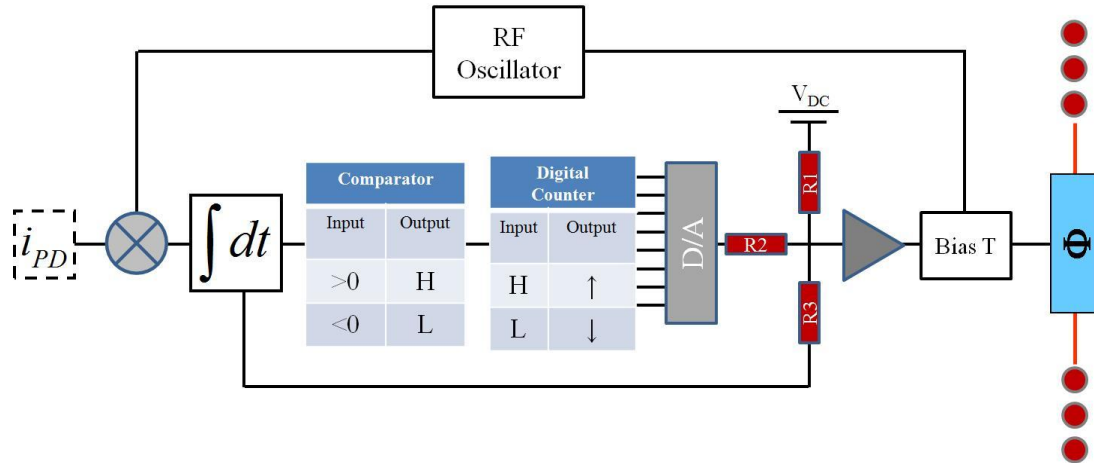
Figure 35: Basic operational schematic of single channel LOCSET operation. N-1 identical LOCSET channels, with the exception of different RF phase dither frequencies, are implemented in a Self-Referenced LOCSET system. (Also shown in Chapter 3).

The LOCSET schematic shown in Figure 35, and described in detail in Chapter 3, shows that there are 2 components to the final error signal feed to the phase modulator. A feed directly from the integrator, is combined with the digital to analog (D/A) output of the digital reset circuit (to the right of Figure 35, 2 of 3 inputs into the summing amplifier). As discussed in previous chapters the digital reset circuit works to remove the load from the integrator by adding, and holding, discrete voltage steps applied to the phase modulator that result in phase changes to the optical beam. Because the digital reset circuit acts as a 'memory' of the phase error signal generated by the integrator, the value returned to the integrator input (via the optical signal incident at the photodetector) will, ideally, hover near zero (optimal phase locking) for all time. By virtue of acting as the memory of the phase error signal created by the integrator output it is safe to assume that the digital reset circuit operates significantly slower than the integrator. As it turns out digital reset circuit operation is governed by a 1MHz TTL clock, holding the least significant bit (LSB) of the digital counter, shown in Figure 35, to operating at TTL time

141

steps, Δt_{LSB}, of 2×10^{-6}s (or 500kHz), approximately 12 times slower than the RC time constant of the integrator, τ_{Int}, of 160ns. It is then safe to assume that the time steps of the digital reset circuit governs just how fast the LOCSET control circuit can operate.

As discussed in previous chapters the digital counter shown in Figure 35 is an 8 bit bi-directional counter for a total of 256 bytes, or steps in voltage, which in turn steps the optical phase of a single channel or beam in the system. Typically the reset voltage is set to $N\pi$ where N is either 2 or 4 in an effort to protect the phase modulator from over voltage. For all coherent beam combination experiments described in this dissertation N was set to 2 so we will focus on 2π reset voltages. We can then divide the phase reset, 2π, by 256 to determine the phase step size of the digital reset circuit, $\Delta\phi_s = .025$ R. Because the LSB is the limiting bit of the circuit its step time, $\Delta t_{LSB} = 2 \times 10^{-6}$s, determines the rate at which LOCSET can correct for the optical phase, $\left(\dfrac{d\phi_{CL}}{dt} \approx \dfrac{\Delta\phi_s}{\Delta t_{LSB}} = 12500 \,{R}\!/\!{s} \right)$, where

$\dfrac{d\phi_{CL}}{dt}$ is the maximum rate at which the LOCSET control loop (CL) can apply changes in phase to the phase modulator. Notice that the maximum rate that LOCSET can change the optical phase of a beam is approximately 13x greater than required to maintain phase locking between the 2 power amplifiers described above (~950 R/s).

5.6. Chapter Summary:

In this chapter the reader was re-acquainted with single channel phase error measurements as they apply to measuring the phase behavior of a single high power amplifier during turn on and steady state operation. This author then proceed to quantify the background baseline noise and determined that the system capable of measuring phase disturbances as low as $\sim\lambda/30$. This author then isolated the amplifier phase behavior effects of quantum defecting heating and temperature cycling of both the industrial chiller and hot plate controllers acting on the gain fiber in the 100W NuFern amplifier. The chapter was then brought to a close by demonstrating that the LOCSET control electronics are indeed capable of maintaining excellent phase locking of at least two 100W NuFern Fiber amplifiers, even in the worst case scenario discussed earlier in the text.

Chapter 6.   Experimental Results: 2 - 32 Channel Coherent Beam Combination via the LOCSET Phase Locking Technique

Experimentally, up to this point we have explored the phase behavior of a single amplifier and determined that the LOCSET electronics are plenty capable of correcting for said phase behavior during both amplifier turn on and steady state operation. What needs to be demonstrated next is LOCSET's capability of coherently combining multiple optical sources. In this chapter we will discuss multi-beam coherent beam combination for 2, 16, and 32 low power beams. More specifically we will discuss the operational performance of said systems under controlled laboratory conditions.

6.1. General Coherent Beam Combination Setup
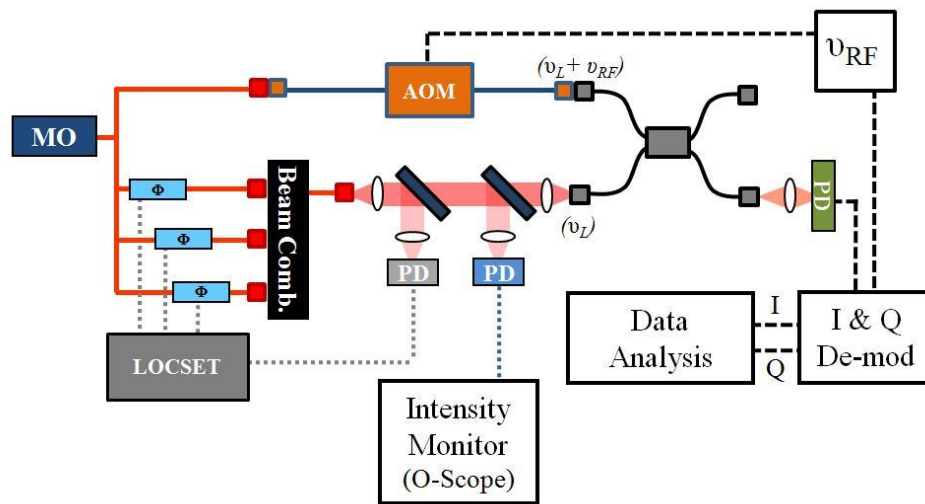
Figure 36: General 'black box' low power LOCSET coherent beam combination experimental setup.

Let's begin by discussing the general setup used in each experiment described below. The coherent beam combination test station used, shown in Figure 36, is essentially the same as described in Chapter 4, and begins to the far left with a single wavelength ($\lambda = 1.064$ μm), narrow linewidth (~10kHz), linearly polarized, master

oscillator (MO). Light from the MO is coupled into a single mode fiber patch cable and then split N ways (up to 32 + 1 channels in the discussions below). N-1 beams pass through LiNbO$_3$ phase modulators providing the LOCSET electronics with piston phase control of each beam for later coherent combination. The remaining beam, to the top of Figure 36, is coupled to an acousto-optic modulator where the light undergoes a frequency shift of υ_{RF} (for the experiments described below: $\upsilon_{RF} = 80$Mhz). Said frequency shifted light will be used as a phase stable reference beam for later optical phase error measurements of the coherent beam combination system. The output(s) of the phase controlled beams are then perfectly overlapped via a 'black box' beam combiner, the output of which is collimated and allowed to propagate through a set of beam combination diagnostics (experimentally the 'black box is replaced with different fiber and free space splitters/combiners as will be discussed in the following experimental descriptions). The collimated combined beam is then sampled via a 10% wedged beam sampler with the sampled light incident on a photodetector providing feedback to the LOCSET control electronics. The combined beam is again sampled via an identical beam sampler with the sampled light incident on another photodetector acting as an independent monitor of the optical intensity of the combined beam. Lastly, the remaining light in the combined beam is coupled into a 2x2 fiber splitter/combiner where it is interfered with the frequency shifted reference beam described above. The combined signal is then output and incident on a final photodetector that feeds into the in-phase (I) and quadrature (Q) demodulation electronics used in determining the optical phase error of the coherently combined beam, as discussed in Chapter 4. Said optical setup affords us the ability to demonstrate coherent beam combination via the LOCSET phase locking

145

technique while, at the same time, independently monitoring beam combination performance.

6.2. Background Phase Error Measurements
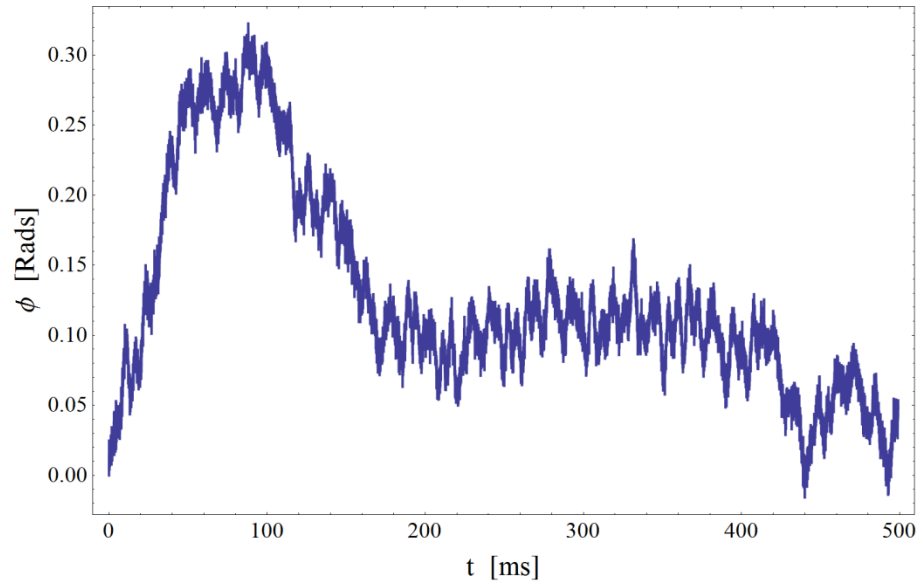
Figure 37: Time varying phase behavior of a single low power fiber channel of a broader LOCSET coherent beam combination system. Fluctuations governed by environmental disturbances.

Before delving into experimental demonstrations of 2, 16, and 32 channel LOCSET coherent beam combination it is important to quantify the system background phase behavior governed by laboratory environmental disturbances. The data shown in Figure 37 represents the optical phase behavior measurement error due to external disturbances acting on the optical fiber of a single channel of the coherent beam combination system measured with respect to the frequency shifted reference beam, also disturbed by its surroundings. Said phase behavior over a period of 0.5 seconds exhibits a larger slow oscillation with faster, much lower amplitude, phase disturbances riding along on top of it. To determine the resolution of the phase error measurement the RMS phase error

146

between data points separated by some time Δt, $\Delta\phi_{RMS}(\Delta t)$, the structure function, is

calculated for the data in Figure 36 and shown in Figure 38.
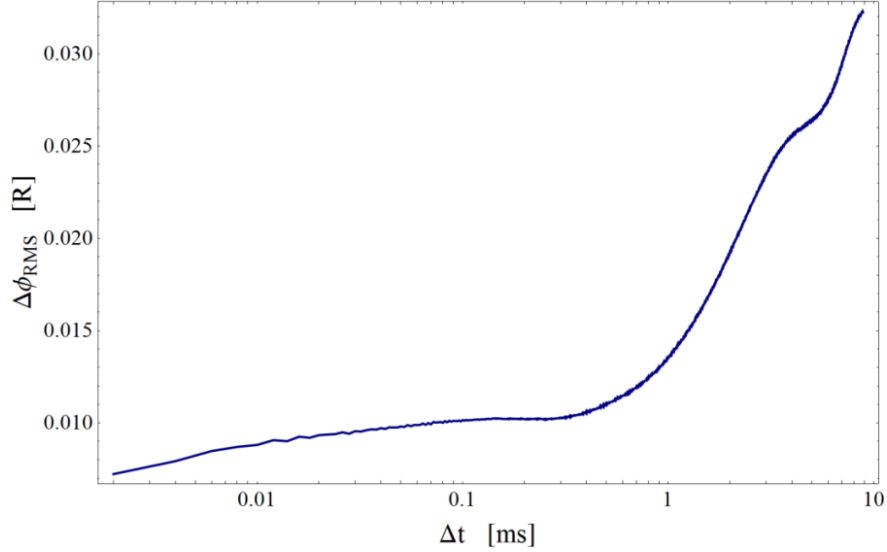
Figure 38: Phase error structure function of the background phase vs. time data set shown in Figure 37 (see discussion on structure function in Chapter 5). Notice that the RMS phase error remains very small, $\leq \lambda/450$ ($\sim$0.014R), and relatively constant through $\Delta t \approx$ 1ms.

Notice in Figure 38 that the RMS phase difference between data points,

$\Delta\phi_{RMS}(\Delta t)$, remains quite small, $\leq \lambda/450$ ($\sim$0.014R), and relatively constant for Δt up to

$\sim$1ms. This information tells us that larger environmental phase disturbances, $> \lambda/450$,

typically operate at time scales greater than 1ms. Therefore, when determining the RMS

phase behavior of a coherently combined beam, by choosing a data window less than or

equal to 1ms we can be confident that the phase behavior of the frequency shifted

reference beam is stable to $\leq \lambda/450$ when measured relative to any one beam in the

coherent beam combination system. This effectively establishes our phase error

measurement resolution at $\sim\lambda/450$ ($\sim$0.014R), 4 to 8 times the resolution needed to

measure expected coherent beam combination phase errors of $\lambda/50$ to $\lambda/100$.

147
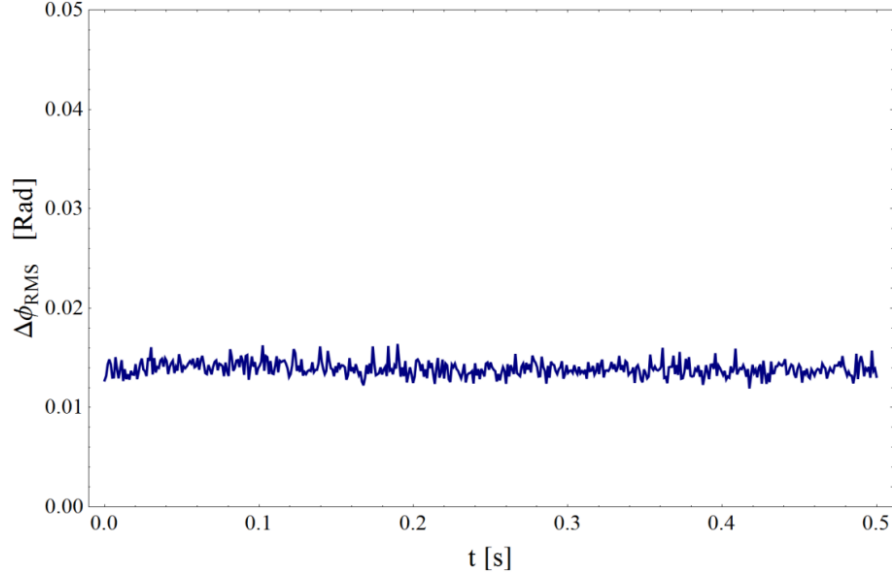
Figure 39: RMS phase error as a function of time for the background data shown in Figure 37. RMS values calculated over a period of 1ms. Average background RMS phase error: ~λ/450 (~0.014R).

To drive this point home let's calculate the background RMS phase error for the data shown in Figure 37. This is accomplished by simply dividing the data shown in Figure 37 into 1ms windows, calculating the RMS value for each phase vs. time data window, and plotting the result as is done in Figure 39. Notice that the average phase error, $\Delta\phi_{RMS}(t)$, remains relatively constant, and quite low, ~λ/450 (~0.014R), for the full 0.5 second data set. This is in excellent agreement with our interpretation of the structure function that the phase behavior of the reference beam, when measured relative to any one channel in the beam combination system, will remain small and constant with $\Delta\phi_{RMS}$ $\approx \lambda$/450 (~0.014R). This again supports our earlier conclusion that the effective phase error measurement resolution is ~λ/450 (~0.014R), significantly greater than needed to measure the expected phase errors of the coherent beam combination systems described below.

6.3. Two Channel Coherent Beam Combination
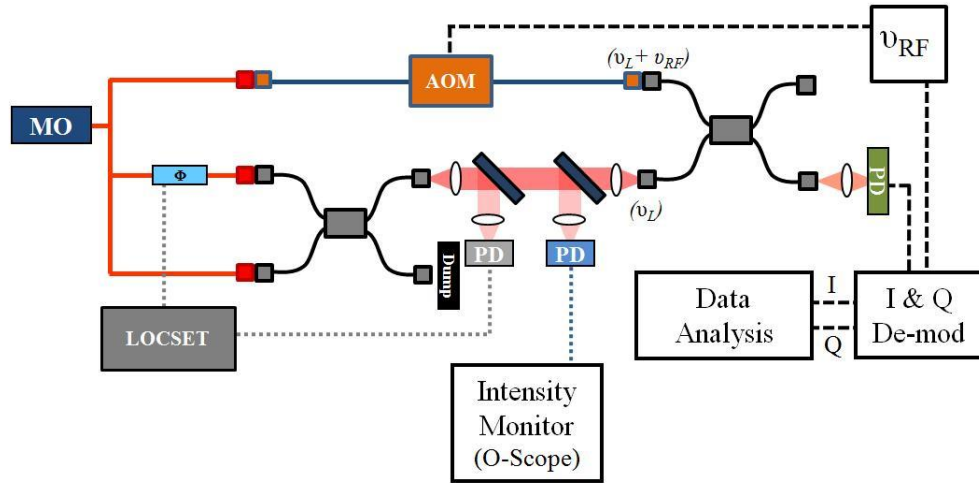
Figure 40: Experimental setup of a 2 channel LOCSET coherent beam combination system.

The first of 3 LOCSET beam combination demonstrations, shown in Figure 40, coherently combines 2 low power beams (1-2mW each) in the Self-Referenced LOCSET configuration (i.e. combines a phase modulated beam with an un-modulated reference beam). Beams were overlapped and interfered in a 2x2 fiber splitter/combiner with the free space output of only 1 port optimized at the photodetector providing feed back to the LOCSET phase control electronics (optical output of the remaining fiber port is fed to a beam dump). As it turns out, when light is optimized for one port of the fiber splitter/combiner (i.e. $\Delta\phi = 0$) no light exits the remaining port assuming of course that the two beams have equal intensity profiles, just as discussed near the beginning of Chapter 3. After optimization the coherently combined beam is then monitored for both intensity and phase behavior performance as described in previous chapters and discussed below.

6.3.1 Intensity Measurement: 2 Channel Beam Combination
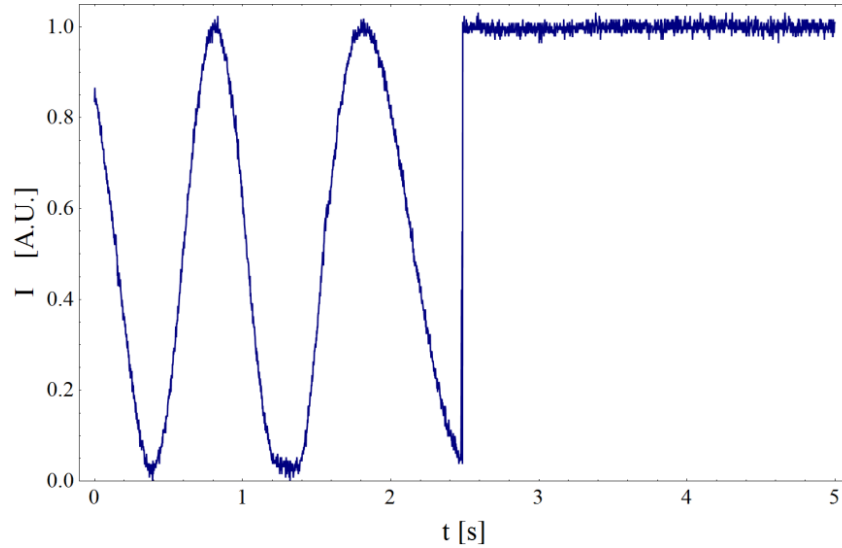
Figure 41: Time varying intensity of the 2 channel, low power, LOCSET coherent beam combination system shown in Figure 40. LOCSET electronics remain off until 2.5 seconds into data acquisition. Slow oscillations preceding the 2.5 second mark are governed by a time varying temperature induced change in index of refraction of the optical fiber.

Let's now take a look at the intensity behavior, shown in Figure 41, of our 2 channel coherent beam combination system as measured at the independent intensity monitor in Figure 40. For the first 2.5 seconds of data acquisition the LOCSET electronics are off allowing the intensity to drift due to environmental disturbances affecting the phase behavior of the 2 channel beam combination system. As alluded to above, the laboratory environment is stable enough not to expect a drastic phase drift, and therefore intensity change, in the system over just a few seconds. For the demonstration shown in Figure 41 this author held his hand 1 to 2 inches above just one of the fiber channels in the 2 channel beam combination system to thermally induce an index of refraction change in the optical fiber due to the heat transferred from his hand to the fiber $\left(\dfrac{dn}{dT} \right)$. After a few moments this author removed his hand, allowing the fiber to cool, and

started the data acquisition. Then, after a few seconds the LOCSET electronics were turned on to establish coherent combination of the 2 overlapped beams. Both scenarios are clearly seen in the data shown in Figure 41. As the phase of the light, guided in the cooling fiber, fluctuates with respect to the second beam in combination system the intensity also fluctuates as governed by the following 2 beam interference equation,

$$\frac{Int(\Delta\phi)}{Int_o} = 2(1+\cos(\Delta\phi)).$$

6.1

Then, also seen in Figure 41, after 2.5 seconds the LOCSET electronics are switched on and the phase difference, $\Delta\phi$, is held near zero regardless of the phase disturbances acting on each of the 2 beams. This is evidenced by the intensity in Figure 41 remaining peaked for the final 2.5 seconds of data acquisition, even though the thermally disturbed fiber was still cooling.

The data shown in Figure 41 is a nice demonstration of 2 beam coherent beam combination but it is difficult, if not impossible, to extrapolate from it the phase behavior of the 2 channel coherent beam combination system. Granted the expression found in equation 6.1 can easily be solved for $\Delta\phi$ but for very small phase errors, $< \lambda/25$ or so, the phase behavior quickly becomes lost in the measurement noise. We must therefore rely on the phase behavior measurements described in previous chapters to determine the phase locking performance of the beam combination system.

6.3.2 Phase Locking Performance: 2 Channel Beam Combination

Before revealing the phase error performance results for the 2 channel coherent beam combination system described above it needs to be noted that the RMS phase error, for typical LOCSET coherent beam combination systems, is not determined entirely from the

phase error measurement shown in Figure 40 (I and Q demodulation electronics). As the

reader may recall, in a LOCSET coherent beam combination system, each phase

controlled beam is tagged, or modulated, with a unique RF phase dither frequency of

some amplitude, β. For the 2 channel beam combination experiment described above the

RF phase dither frequency was approximately 100MHz with a peak to peak sinusoidal

dither amplitude, β, of approximately λ/67 (~0.094R). Said value of β was obtained by

measuring the RF phase dither voltage supplied to the $LiNbO_3$ modulator controlling the

optical phase of the sole phase modulated beam in the 2 channel system and relating it to

the manufacturer supplied $\dfrac{\Delta\phi}{\Delta V}$ scale factor. Because the phase error measurement

utilizes a 80MHz reference signal to demodulate the in-phase (I) and quadrature

components (Q) of the photodetector current, which is proportional to the AC

fluctuations of the optical intensity, it is unable to measure phase disturbances beyond the

80MHz reference signal. In practice, the maximum phase error measurement bandwidth

is just a few MHz governed by the manufacturer set integration time in the I and Q

demodulation module. Therefore, to obtain the total RMS phase error for the coherent

beam combination system, we must determine the RMS phase error of the of the

sinusoidal RF dither frequency of each beam in the coherent beam combination system,

$\Delta\phi_{RF(RMS)}$, and somehow combine it with the slower phase errors of the coherently

combined beam, $\Delta\phi_{<1MHz(RMS)}$, determined via the I and Q demodulation technique shown

in Figure 40.

Let's begin by determining the RMS phase error, $\Delta\phi_{RF(RMS)}$, governed by the

sinusoidal RF phase dither of the only phase controlled channel in the 2 beam coherent

beam combination system described above (remember that one beam is acting as an un-modulated reference beam). We know that time varying sinusoidal signals have an RMS value governed by the following equation,

$$\beta_{RMS} = \frac{\sqrt{2}}{2}\beta_{p-p},$$

6.2

where β_{p-p} is the peak to peak amplitude of the time varying sinusoidal signal and β_{RMS} is its RMS value. Therefore, for a peak to peak RF phase modulation amplitude of approximately $\lambda/67$ (~0.094R), we can calculate the corresponding RMS RF phase error, $\Delta\phi_{RF(RMS)}$, as shown below,

$$\Delta\phi_{RF(RMS)} = \beta_{RMS} = \frac{\sqrt{2}}{2}\beta_{p-p} = \frac{\sqrt{2}}{2}(0.094),$$

$$\Delta\phi_{RF(RMS)} = 0.067R.$$

6.3

Armed with the RF phase error contribution to the total phase error signal, and with the slower RMS phase error contribution of the coherently combined beam measured via the I and Q demodulation electronics, we can proceed with determining the total phase error of the coherently combined beam.

It is important to realize that, because the behavior of the sinusoidal RF phase modulation signal is well defined, and the phase errors of the coherently combined beam respond to the erratic whims of environmental disturbances and any LOCSET control loop errors, the two signals are effectively uncorrelated. Because the two signals are uncorrelated we can calculate the total RMS phase error signal, $\Delta\phi_{RMS}$, of the 2 channel coherent beam combination system by summing the squares of the two independent RMS phase errors and take the square root of the result as shown in the following equation,

153

$$\Delta\phi_{RMS} = \sqrt{\Delta\phi^2_{<1MHz(RMS)} + \Delta\phi^2_{RF(RMS)}}.$$

6.4

We can then plug equation 6.3 into equation 6.4 and write our final expression for

determining the total phase error of the 2 channel coherently combined beam as follows,

$$\Delta\phi_{RMS} = \sqrt{\Delta\phi^2_{<1MHz(RMS)} + \left(\frac{\sqrt{2}}{2}\beta_{p-p}\right)^2},$$

$$\Delta\phi_{RMS}\left[2 \text{ chl.}\right] = \sqrt{\Delta\phi^2_{<1MHz(RMS)} + \left(0.067\right)^2}.$$

6.5

This is an important result as it allows us to correct for any known, measurable, and

uncorrelated, phase error contributions beyond the limits of the I and Q demodulation

based phase error measurement discussed above.

Armed with an expression combining both the RMS phase errors measured via I

and Q demodulation, $\Delta\phi_{<1MHz(RMS)}$, and phase errors stemming for the intentional RF phase

dither applied to the single phase modulated beam of our 2 channel system, $\Delta\phi_{RF(RMS)}$, we

can render a final string of data points representing the total RMS phase error, $\Delta\phi_{RMS}$, of

said 2 channel beam combination system as shown in Figure 42.
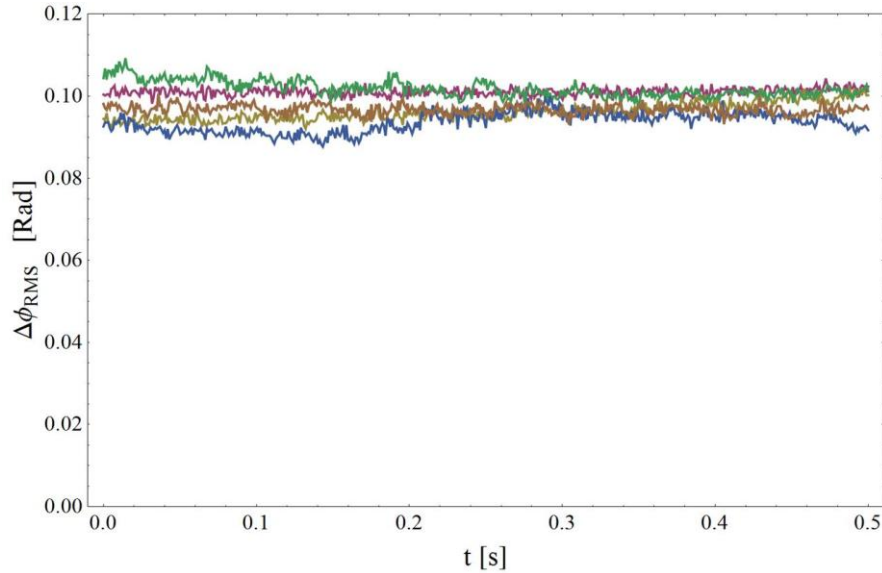
Figure 42: RMS phase error as a function of time for the 2 channel, low power, LOCSET coherent beam combination system shown in Figure 40. RMS values calculated over a period of 1ms. Multiple data sets, taken during a single run of the 2 channel system, were included to demonstrate consistency in beam combination performance. Average observed RMS phase error: $\overline{\Delta\phi}_{RMS} \approx \dfrac{\lambda}{66}$ (~0.095R).

Shown in Figure 42 are multiple RMS phase behavior data sets taken during a single 5 minute run of the 2 channel LOCSET coherent beam combination system described above. Each data set was included in an effort to convey to the reader the stability of the 2 channel coherent beam combination system as a function of time. Though the data shown in Figure 42 was limited to a 5 minute or so data collection period such beam combination performance and stability was often observed for hours at a time and maintained until the next day when the coherent beam combination system was turned back on again (no re-tuning of the LOCSET electronics required). For the data shown in Figure 42 the average RMS phase error of the 2 channel coherent beam combination system is approximately λ/66 with 2 standard deviations from the mean significantly less than λ/300 (governed mostly by measurement noise), a most welcome result.

6.4. Sixteen Channel Coherent Beam Combination
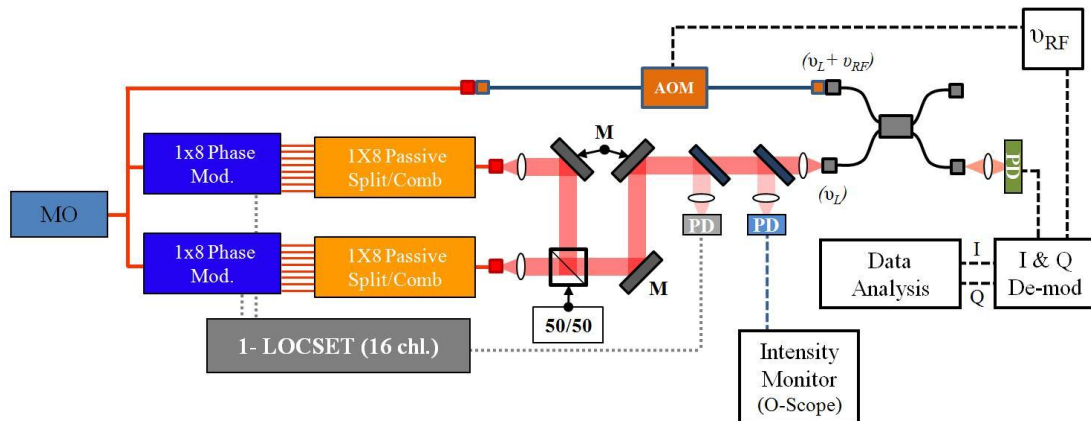
Figure 43: Experimental setup of a 16 channel LOCSET coherent beam combination system. M: Mirror. 50/50: 50% reflective/transmissive beam splitter.

The second of 3 LOCSET beam combination demonstrations, shown in Figure 43, coherently combines 16 low power beams (1-2mW each) in the Self-Referenced LOCSET configuration (15 phase controlled beams and 1 un-modulated reference beam). The experimental setup remains exactly the same as done for the 2 channel coherent beam combination system shown in Figure 40 with the exception of 16 combined beams instead of just 2. Just as before the setup begins with a single MO oscillator, the output of which is coupled into a single fiber patch cable and then split into 3 individual fiber channels, 2 of which will be cascaded into 16 individual fiber channels for later coherent combination. The remaining beam, just as before, is frequency shifted, via the AOM, and used as a reference beam for later phase error measurements. The 2 non-frequency shifted fiber channels to the left of Figure 43 are coupled into individual 1x8 $LiNbO_3$ phase modulators, each converting a single input beam into 8 phase controllable optical channels, for a total of 16 beams (though 1 will remain un-modulated to act as a reference beam). The outputs of each 1x8 $LiNbO_3$ module is then recombined via a passive 1x8 $LiNbO_3$ fiber splitter/combiner, combining 8 beams back into 1, leaving us with two

individually combined beams. The final two beams, each consisting of 8 individual phase

modulated/controlled beams, propagate in free space and combine at the interface of a

50/50 beam splitter/combiner. The final combined beam, after the 50/50

splitter/combiner, is then processed via the same optical setup providing the LOCSET

error signal and subsequent beam combination performance measures as done in Figure

40 for the 2 channel coherent beam combination demonstration.

6.4.1 Intensity Measurement: 16 Channel Beam Combination
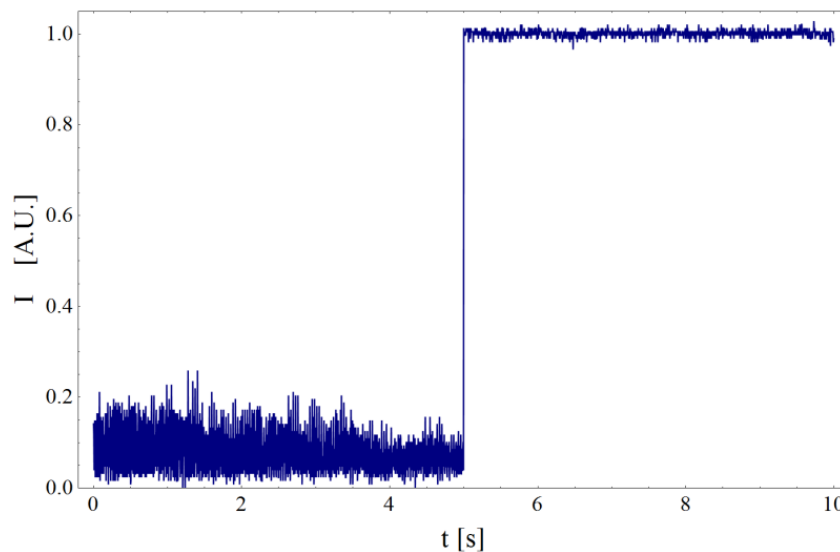
Figure 44: Time varying intensity of the 16 channel, low power, LOCSET coherent beam combination system shown in Figure 43. LOCSET electronics remain on for the entire data acquisition time. LOCSET return signal photodetector blocked for the first 5 seconds of the data acquisition depriving the control electronics of a feedback signal. After 5 seconds the LOCSET detector was unblocked allowing the system to return to optimal beam combination.

Just as done for the 2 channel beam combination demonstration, intensity

measurements were performed for the 16 channel coherent beam combination system

shown in Figure 43, the results of which are shown in Figure 44. Figure 44 demonstrates

the intensity performance disparity of the 16 channel beam combination system between

when the system is phase locked and when it is not. During the full duration of the test

shown in Figure 44 the LOCSET phase locking electronics were on and fully operational. For the first 5 seconds of data acquisition the optical signal to the LOCSET photodetector was blocked, depriving the control electronics of a usable error correction signal. Just because no light is incident on the LOCSET detector doesn't mean the control electronics are going to stop sending control voltages to the phase modulators controlling the optical beams. Instead, without a suitable error signal, the control electronics send erratic control voltages, governed solely by the electronic noise in the LOCSET circuit, to each of the 15 phase controlled beams wildly affecting the output intensity of the combined beam. Looking at Figure 44 we notice that while the feedback detector is blocked the intensity output of the combined beam does indeed fluctuate wildly due to the erratic phase behavior of the 15 phase modulated beams in the Self-Reference LOCSET beam combination system. Now notice that when the LOCSET photodetector is un-blocked, and a suitable error signal returns to the LOCSET control electronics, the system returns to optimal beam combination as evidence by intensity maximization for the remaining 5 seconds of the data acquisition.

Just as with the 2 channel coherent beam combination system, the data shown in Figure 44 is a nice demonstration of 16 beam coherent beam combination but it is difficult, if not impossible, to extrapolate from it the RMS phase behavior of the 16 channel coherent beam combination system. Therefore we must again rely on the phase behavior measurements described in previous chapters to determine the phase locking performance of the coherently combined beam.

6.4.2 Phase Locking Performance: 16 Channel Beam Combination
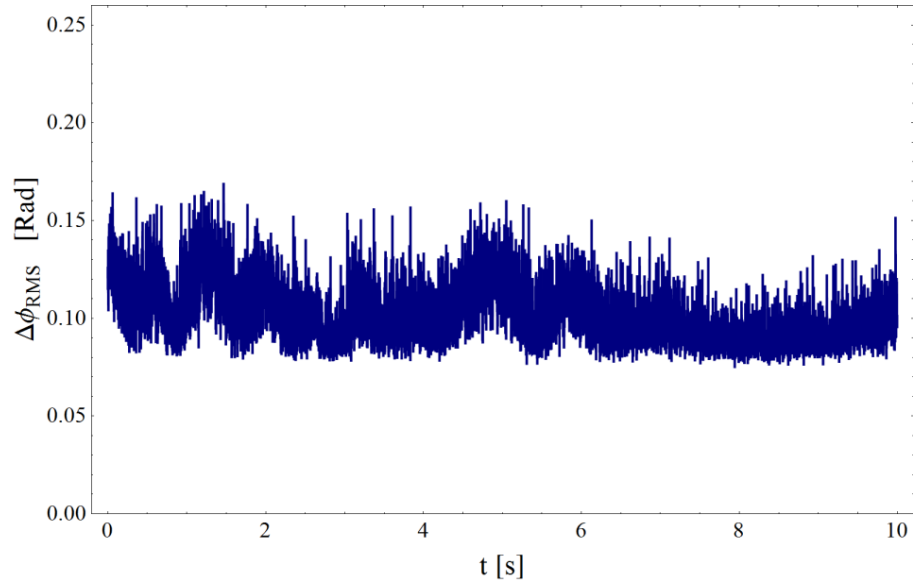
Figure 45: Measured RMS phase error as a function of time for the 16 channel, low power, LOCSET coherent beam combination system shown in Figure 43. RMS values calculated over a time period of 1ms. Average observed RMS phase error for 16 channel

system: $\overline{\Delta\phi_{RMS}} \approx \dfrac{\lambda}{62}$ (~0.1R).

The data shown in Figure 45 represents the RMS phase error, $\Delta\phi_{RMS}$, of the 16

channel coherently combined beam as a function of time. Notice though that the RMS

phase behavior appears to be much more erratic than that observed during 2 channel

beam combination. One might guess that such behavior evidences operational issues with

the LOCSET control electronics though this is not the case. Recall from our discussion

on LOCSET implementation in Chapter 3 that 2π phase reset voltages had to be

implemented to protect the $LiNbO_3$ phase modulators used to control the piston phase

behavior of individual beams in the overall beam combination system form a possible

over voltage demise. For a 2 channel system said resets are typically few and far between

when operating in a calm, stable environment; maybe one or two every 30 seconds to a

minute. Now with 16 beams coherently combined together, 15 of which are phase

controlled and therefore subject to sudden 2π phase reset voltages, the likely hood of a

voltage reset significantly increases. Even in the calm laboratory environment created for

these experiments, when implementing a 16 channel beam combination system, it is

typical to see 10-50 voltage resets per second in the combined beam, sometimes more. It

is important to note that there is nothing governing how many channels are allowed to

undergo a voltage reset in a given time frame. Theoretically multiple channels could reset

at exactly the same time. It is also possible that no voltage resets will occur in a over a

significantly long time frame. It all depends on the relative phase state of each of the 16

beams measured with respect to each other. It is this uncoordinated voltage reset behavior

that results in the erratic RMS phase behavior shown in Figure 45. Despite such behavior

the RMS phase error performance of a 16 channel coherently combined beam, phase

locked via LOCSET, exhibits an average RMS phase error of approximately $\lambda/62$

($\sim$0.1R), accounting for both slow and RF phase errors; again, a very welcome result.

6.5. Thirty-two Channel Coherent Beam Combination
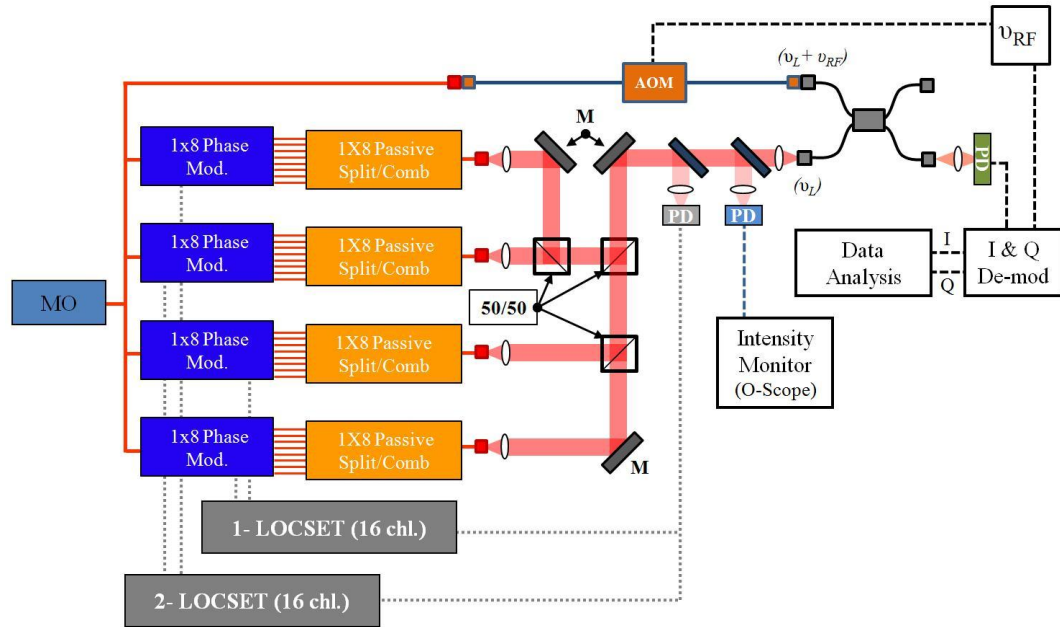
Figure 46: Experimental setup of a 32 channel LOCSET coherent beam combination system.

The third and final of 3 LOCSET beam combination demonstrations, shown in Figure 46, coherently combines 32 low power beams (1-2mW each) in the Self-Referenced LOCSET configuration (31 phase controlled beams and 1 un-modulated reference beam). The experimental setup remains exactly the same as done for both the 2 and 16 channel coherent beam combination systems, shown in Figure 40 and Figure 43 respectively, with the exception of 32 combined beams instead of just 2 or 16. Just as before the setup begins with a single MO oscillator, the output of which is coupled into a single fiber patch cable and then split into 5 individual fiber channels, 4 of which will be cascaded into 32 individual fiber channels for later coherent combination. The remaining beam, just as before, is frequency shifted, via the AOM, and used as a reference beam for later phase error measurements. The 4 non-frequency shifted fiber channels to the left of Figure 46 are coupled into individual 1x8 LiNbO$_3$ phase modulators, each converting a

single input beam into 8 phase controllable channels, for a total of 32 phase controllable channels (though 1 will remain un-modulated to act as a reference beam). The output of each 1x8 LiNbO$_3$ module is then recombined via a passive LiNbO$_3$ fiber splitter/combiner, combining 8 beams back into 1, leaving us with 4 combined beams. The final 4 beams, each consisting of 8 phase modulated beams, propagate in free space and combine via a binary tree of 50/50 beam splitters/combiners into single 32 channel beam. The final combined beam, after the binary tree, is then processed via the same optical setup providing the LOCSET error signal and subsequent beam combination performance measures as done in Figure 40 and Figure 43 for both the 2 and 16 channel coherent beam combination demonstrations.

6.5.1 Binary Tree Beam Combiner
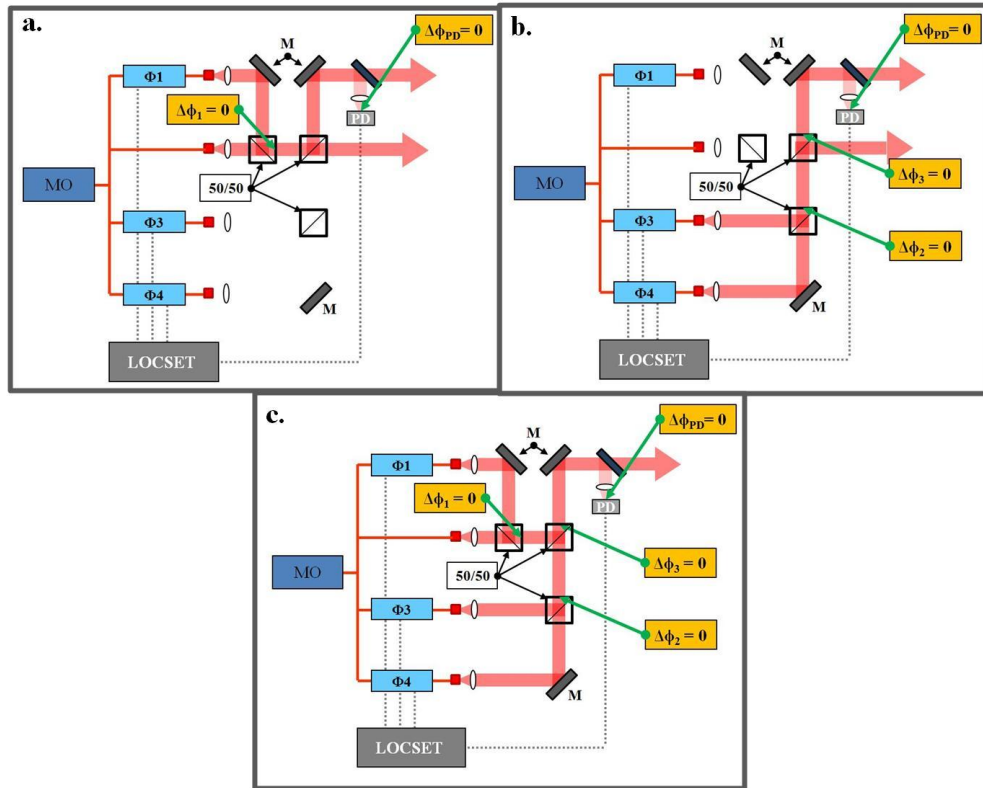
Figure 47: 4 beam coherent beam combination utilizing a binary tree of 50/50 splitters/combiners. [a.] If only beams 1 and 2 are on LOCSET will minimize $\Delta\phi$ at both the LOCSET detector (PD) and the exit of beam splitter 1. [b.] .] If only beams 3 and 4 are on LOCSET will minimize $\Delta\phi$ at both the LOCSET detector (PD) and the exit of beam splitter 2. [c.] If the phase difference between all beams are equal to 0 at each of the three intercepts of the binary tree then all beams will be coherently combined thereby maximizing the intensity out of the final port of the binary tree without losing any light at any of the unused beam splitter ports, assuming of course all 4 beams in the system share common polarization and intensity profiles.

It is worth taking a minute to discuss the basic operation of the binary tree of

50/50 splitters/combiners utilized as the final stage of the 32 channel beam combination

experiment shown in Figure 46. Imagine the simple 4 beam LOCSET coherent beam

combination system shown in Figure 47. As with each of our experimentally

demonstrated beam combination setups this system begins with a single MO, the output

of which is coupled into a single fiber patch cable and then split into 4 individual fiber

channels. 3 of the 4 fiber channels is phase controlled (1, 3 and 4) leaving light in the

remaining fiber channel to act as an un-modulated reference beam (beam 2). The optical

output of each channel is then collimated and free space propagated through a binary tree

of 50/50 beam splitters/combiners. Upon exiting the binary tree the combined beam is

sampled at a partial reflector with the sampled light incident on a photodetector providing

the necessary feedback signal to the LOCSET electronics for final beam combination.

It is easiest to understand how the binary tree beam combiner works by dividing it

into 3 operational components. The first, shown in Figure 47a, we will define as the

optical interaction at the first 50/50 beam splitter labeled $\Delta\phi_1$. As discussed in Chapter 3,

assuming identical polarization and intensity profiles for the two interfering beams (beam

1 and 2), all light will exit a single port of the beam splitter if the phase difference

between the two beams, $\Delta\phi_1$, is equal to zero. We can see in Figure 47a that if the

LOCSET beam combination electronics minimizes the phase difference between beams 1

and 2 at the LOCSET photodetector, $\Delta\phi_{PD}$, the phase difference between the two beams

at beam splitter 1 will also be minimized, despite passing through a second 50/50 beam

splitter (#3 in Figure 47). This is a result of the two overlapping beams following a

common path from beam splitter 1 to the photodetector and therefore experiencing

common phase disturbances along the way (no net phase difference between the two

beams encountered). We will denote the resulting combined beam, between beam 1 and

2, as beam 1|2. This very same behavior is also exhibited in our second operational

condition, shown in Figure 47b, only this time the interaction is between beams 3 and 4 at

beam splitter number 2. Similarly to beam 1|2 we will denote the resulting combined

beam between 3 and 4 as beam 3|4. The question then becomes how do we combined

these two independently combined beams at the third and final beam splitter.

Via the behavior described above we now have two independently coherently combined beams, 1|2 and 3|4, incident on common photodetector. If we allow both systems shown in Figure 47 a and b to operate at the same time, with a common photodetector, we'll find that all four beams will coherently combined together to form a single output from the binary tree, shown in Figure 47c, with no changes to the beam combination system required. This is because, as shown in Figure 47 a and b, once beam 1 and beam 2 are coherently combined they can be treated as a single beam, 1|2, incident on the 3rd beam splitter. The same is true after coherently combining beam 3 and 4 combining together to form beam 3|4, with is also incident on the third beam splitter. To coherently combine the resulting two beams all that needs to be done is add the appropriate piston phase control to each combined beam, 1|2 and 3|4, to minimize the phase difference between them at the 3rd and final beam splitter/combiner. The LOCSET electronics automatically achieve this piston phase shift to either or both beams, 1|2 and/or 3|4, in the setup shown in Figure 47c by the applying a common piston phase shifts to either beams 1 and 2, or beams 3 and 4. Said phase shifts to the individual beams will not effect the combination at beam splitter 1 or 2 because the net phase difference between the two beams incident on beam splitters 1 and 2 remain unaffected. This behavior allows the LOCSET electronics the degrees of freedom necessary to minimize the phase difference between interfering beams at all three beam splitters shown in Figure 47c by minimizing the phase difference between all 4 beams interfering at the photodetector, $\Delta\phi_{PD}$. The result of minimizing $\Delta\phi_{PD}$ is to have all light exit the final port of the binary tree without optical loss at any of the three 50/50 beam splitters. This

assumes of course that each of the 4 beams has identical polarization and intensity profiles.

6.5.2 Intensity Measurement: 32 Channel Beam Combination
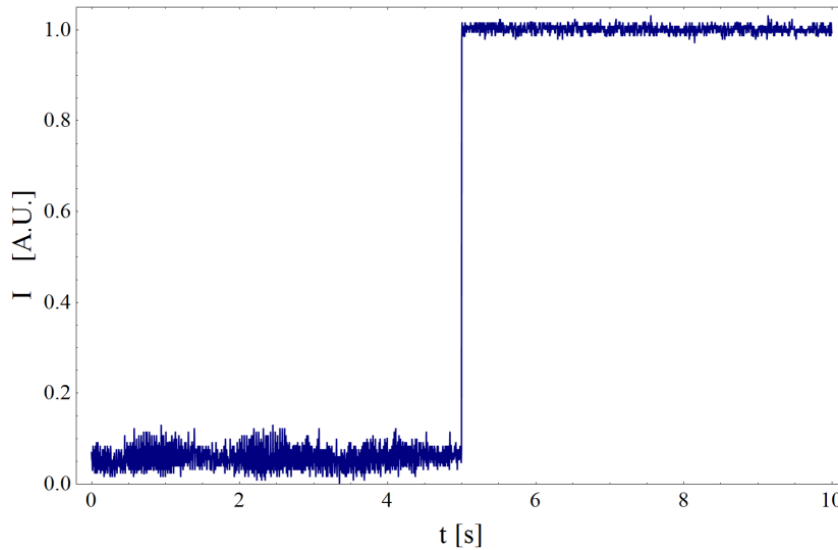
Figure 48: Time varying intensity of the 32 channel, low power, LOCSET coherent beam combination system shown in Figure 46. LOCSET electronics remain on for the entire 10 second data acquisition time. LOCSET return signal photodetector blocked for the first 5 seconds of data acquisition depriving the control electronics of a feedback signal. After 5 seconds the LOCSET detector was unblocked allowing the system to return to optimal beam combination.

Let's now discuss the results of the final, and possibly the most important, beam combination demonstration in this dissertation, that done for 32 lower power optical beams. As the experiments performed were identical to that done for the 2 and 16 channel demonstrations described above, all that remains is to present said results. Shown in Figure 48 is a beam combination demonstration similar to that done for the 16 channel coherent beam combination system that measures the relative optical intensity at the independent intensity monitor shown in Figure 46. For the entire 10 second data acquisition time the LOCSET electronics remained on and fully operational. For the first 5 seconds the light incident on the photodetector providing the LOCSET electronics a

feedback signal was blocked, forcing the system to make phase control decisions for each of the 31 phase controlled beams based on electronic noise in the circuit. After 5 seconds the light at the LOCSET photodetector was unblocked providing a useful error correction signal to the LOCSET electronics. Just as for the 16 channel demonstration both situations can be seen in the data shown in Figure 48. For the first 5 seconds, when LOCSET is deprived of a feedback signal, the system beam combination performance is dismal at best with intensities less than 20% of the peak. Once the optical feedback signal is reintroduced to the photodetector feeding the LOCSET electronics the 32 channel coherently combined beam is once again optimized as is evidenced by the maximization of the optical intensity for the remainder of the data acquisition.

Just as with the 2 and 16 channel beam combination systems, the data shown in Figure 48 is a nice demonstration of 32 beam coherent beam combination but it is difficult, if not impossible, to extrapolate from it the RMS phase behavior of the beam combination system. Therefore we must again rely on the phase behavior measurements described in previous chapters to determine the phase locking performance of the coherently combined beam.

6.5.3 Phase Locking Performance: 32 Channel Beam Combination
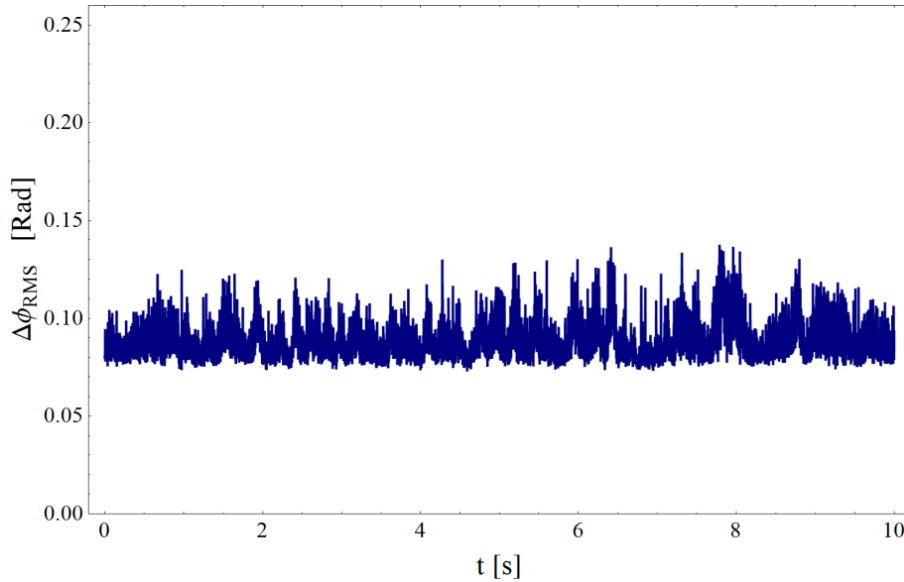
Figure 49: RMS phase error as a function of time for the 32 channel, low power, LOCSET coherent beam combination shown in Figure 46. RMS values calculated over a time period of 1ms. Average observed RMS phase error for 32 channel system:

$$\overline{\Delta\phi}_{RMS} \approx \frac{\lambda}{71} \, (\sim 0.09R).$$

The data shown in Figure 49 represents the RMS phase error, $\Delta\phi_{RMS}$, of the 32 channel coherently combined beam as a function of time. Notice again that the RMS phase behavior appears to be much more erratic than that observed during 2 channel beam combination. The issue here is the same as experienced in the 16 channel coherent beam combination system, the presences of 2π phase resets in each of the 31 phase controlled beams. Even in the calm laboratory environment created for these experiments, when implementing a 32 channel beam combination system, it wasn't uncommon to observe 100+ voltage resets per second in the combined beam. It is this uncoordinated voltage reset behavior of the 32 channel system that results in the erratic RMS phase behavior shown in Figure 49. Despite such behavior the RMS phase error performance of a 32 channel coherently combined beam, phase locked via LOCSET,

exhibits an average RMS phase error of approximately λ/71 (~0.09R), accounting for both slow and RF phase errors; another welcomed result.

6.6. Effects of RMS Phase Errors on a Rectangular Array of Rectangular Apertures

In the text above we discussed the operation and performance of 3 different LOCSET coherent beam combination systems where, for 2, 16, and 32 channel systems, RMS phase errors on the order of λ/65 were consistently demonstrated. The question then becomes how does this physically effect the output beam of a phased array system (i.e. some metric other than RMS phase error). In the demonstrations above phase errors typically affected the combined output by releasing light out of an undesired port(s) of the binary tree beam combiner effectively reducing the total optical power in the combined beam. When considering tiled array coherent beam combination, where the optical outputs of individual sub-apertures are spatially separate and combine only in the far field, the reduction in performance due to RMS phase errors results in a lower peak intensity in the far field diffraction pattern. An excellent metric relating the actual/measured peak intensity of a coherently combined beam, I_{oE}, to the theoretical optimal peak intensity of said beam, I_{oT}, is the Strehl Ratio defined as follows [77] for a rectangular array of individual but identical rectangular sub-apertures,

$$SR = \frac{Int_{oE}}{Int_{oT}} = e^{-\sigma_{\Delta\phi}^2} + \frac{1 - e^{-\sigma_{\Delta\phi}^2}}{N_x N_y},$$

6.6

where SR is the Strehl ratio of the coherently combined beam, $\sigma_{\Delta\phi}$, is the common statistical variance in the un-correlated optical phase state of each array element, and $N_{x,y}$ are the number of rectangular sub-apertures in the x and y directions of the rectangular

169

packed tiled array respectively [77]. It is important to note that equation 6.6 assumes that each array sub-aperture is uniformly illuminated and maintains such common optical characteristics as output power, intensity profile, and polarization state, leaving only the un-correlated optical phase states of each sub-aperture to differ. We can then relate the statistical variance, $\sigma_{\Delta\phi}$, to the RMS phase error, $\Delta\phi_{RMS}$, via the following equation [78],

$$\Delta\phi_{RMS}^2 = \overline{\Delta\phi}^2 + \sigma_{\Delta\phi}^2, \qquad\qquad 6.7$$

where $\overline{\Delta\phi}$ is the mean phase deviation in optical phase. Because the optical phase of each sub-aperture output oscillates about the optimal phase condition $\Delta\phi = 0$, $\overline{\Delta\phi}$ must also equal zero. We then plug equation 6.7 into equation 6.6 to obtain our final expression relating the far field Strehl ratio of an rectangular array of coherently combined beams to the common, though un-correlated, RMS phase error of each array sub-aperture, $\Delta\phi_{RMS}$, as shown below,

$$SR = e^{-\Delta\phi_{RMS}^2} + \frac{1 - e^{-\Delta\phi_{RMS}^2}}{N_x N_y}, \qquad\qquad 6.8$$

This is an important and useful result! Even though equation 6.8 was established via a set of relatively stringent conditions (uniform illumination of an N_x x N_y rectangular array of rectangular sub-apertures) it can still be used to *approximate* the expected behavior of most typical tiled array arrangements!

NxN	Total # of Sub-Apertures	% Reduction in SR
2x2	4	~0.69%
3x3	9	~0.82%
4x4	16	~0.86%
5x5	25	~0.88%
6x6	36	~0.89%
7x7	49	~0.90%
8x8	64	~0.90%
9x9	81	~0.91%
10x10	100	~0.91%

Table 5: Reduction in Strehl ratio, SR, for rectangular packed tiled arrays of identical rectangular apertures. Calculations assume common phase errors in each sub-aperture of $\lambda/65$ (0.096R).

Let's now take a quick look at how un-correlated phase errors on the order of those measured previously would affect NxN rectangular arrays of identical rectangular sub-apertures. Shown in Table 5 is a list of calculated 'percent reductions' in the far field Strehl ratio for 4 through 100 element square packed arrays (NxN) with un-correlated RMS phase errors of $\lambda/65$ (0.096R) across each array sub-aperture. Note that, for up to 100 array elements, such RMS phase errors effect a reduction in the far field Strehl ratio of the coherently combined beam of less than 1% [77]!

6.7. Coherent Beam Combination Summary

This chapter provided the reader a general description of the setup and implementation of 2 through 32 channel coherent beam combination systems, utilizing the LOCSET phase locking technique, and necessary diagnostics. Said beam combination systems demonstrated phase error performance as low as $\lambda/71$ for 32 low power coherently combined beams. The chapter then concluded with a discussion on the effect of such phase errors on a typical tiled array coherent beam combination system demonstrating that for un-correlated RMS phase errors of $\lambda/65$ across individual array sub-apertures the resulting reduction in the combined beam Strehl ratio would be less than 1% for up to

100 array elements [77]. This author has therefore demonstrated that the optical outputs of a large number of fibers can be coherently combined with high fidelity using the LOCSET phase locking technique.

Chapter 7.   Including a Remote Object In the Control Loop

In previous chapters we theoretically established, and experimentally demonstrated, a method of coherent beam combination known as the LOCSET phase locking technique. Also in previous chapters we theoretically established, and experimentally demonstrated, a technique for measuring the optical phase state of a single or coherently combined beam with respect to a phase stable frequency shifted reference beam. We then employed said phase measurement to characterize the optical phase behavior of a single 100W fiber amplifier and determined that the LOCSET phase locking is capable of maintaining phase lock of this narrow linewidth high power amplifier, when combined with a second high power output, during both turn on and steady state operation. We then proceeded to demonstrate coherent beam combination of 2, 16, and 32 low power optical beams, again employing the phase behavior measurement, demonstrating up to 32 coherently combined beams with RMS phase errors of $\sim\lambda/71$. It therefore isn't difficult to imagine the possibility of coherently combining up to 32 high power beams into a single, much higher power, coherent output.

Looking at the accomplishments listed above it might be tempting to say that all is well if left alone and close the book on further research and development of the LOCSET phase locking technique… but doing so would be most unfortunate. All the research, theory, and experimental demonstrations described thus far have confined the LOCSET phase locking technique to local beam optimization at a single photodetector, feeding the LOCSET control electronics, with no thought on what happens to the final output beam as it propagates to the business end of the laser system (i.e. to optimally illuminate a spatially remote object). This situation will be discussed in the text to follow.

7.1. Local Beam Combination via LOCSET
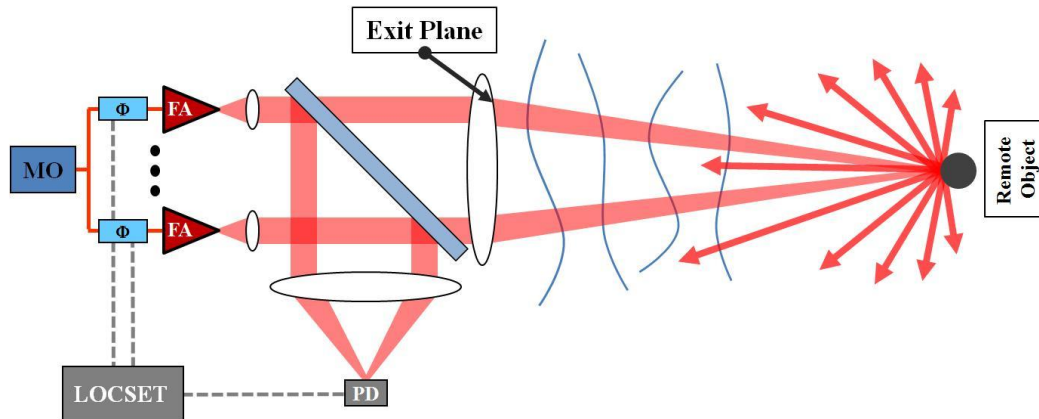
Figure 50: Local LOCSET phase locking technique via a tiled array. Beam optimization done only at the exit aperture plane of LOCSET beam combination system. After exiting the aperture plane each spatially separated beam will experience, in the presences of atmospheric turbulence, different spatial phase distortions. Said phase distortions, applied to the already phase optimized array output, will degrade the beam combination performance on the remote object in the far field.

As alluded to above each LOCSET phase locking demonstration discussed thus far has been confined to beam optimization at the exit aperture of the coherent beam combination system (i.e. the exit plane of the tiled array shown in Figure 50) with the unspoken assumption that the combined output would remain optimized for combination at some other remote point in space. This assumption holds true for the beam combination methods employed in previous chapters where all beams were combined into a single beam in a calm laboratory environment (i.e. no higher order spatial phase aberrations across the profile of the combined output beam due to atmospheric turbulence effects). This assumption does not necessarily hold true, even under calm laboratory conditions, when the beams are combined via a tiled array of spatially separate output sub-apertures before combination in the far field (in the lab a far field interference pattern is generated in the focal plane of a lens). This is due to the fact that each beam will individually experience low order phase aberrations (predominantly piston phase

changes) when propagating in spatially different atmosphere than all other beams in the system (i.e. not following a common path to the remote object). Such piston phase aberrations will affect the beam in a similar manner as heat or mechanical disturbances affect a beams phase state when guided in a fiber, via a uniform phase retardation relative to all other beams in the array. Therefore, when the output of a tiled array is optimized at the exit plane there are no guarantees that the combined beam will be, or remain, optimized on the remote object in the far field in the presence of atmospheric turbulence. We must therefore employ a technique for correcting for such disturbances.

7.2. Employment of a Deformable Mirror (DM)
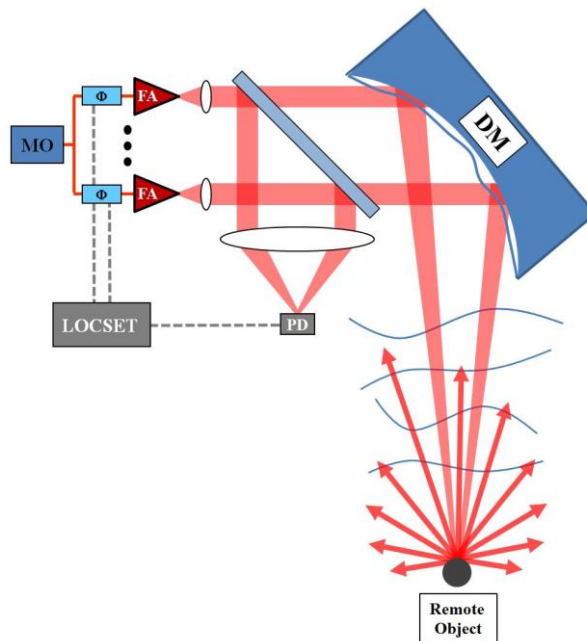
Figure 51: Utilizing a deformable mirror (DM) is a standard method of correcting for atmospheric turbulence. Technique often employed by ground based telescopes.

One possible solution to correcting for aberrations across a tiled array, due to atmospheric turbulence, is to employ a deformable mirror DM. If the system is somehow capable of measuring the atmospheric distortions, possibly by a secondary illuminator

175

laser and spatial phase detection system, introduced to the tiled array output as it propagates to a remote object in the far field then it is possible to dial in an appropriate conjugate of said phase distortions to a DM, shown in Figure 51, and optimize the combined beam at the remote object. Such a technique is well established for ground based telescopes and could very well be implemented in the tiled array beam combination system described above but, as we will discuss further in the section to follow, it may not necessarily be needed.

7.3. Including the Object In the Loop (OIL)

Let's take a moment to compare a simple tiled array, with piston phase control in each array sub-aperture, to the operation of a basic DM. The simplest of DM's consist of a tiled array of flat reflective surfaces with mechanical push, pull, tip, and tilt controls. Push/pull controls alter the optical path length of a single segment of the corrected beam propagating to a remote object in the far field. Tip/tilt controls of each reflective segment alter the left/right and up/down pointing positions of light reflected off of each DM segment. These 4 controls can then be utilized in correcting for many phase aberrations caused by light propagating through turbulent atmosphere towards a remote object in the far field. Let's now compare these controls to a mechanically static, tiled aperture, phased array of individual piston phase controllable beams. Said piston phase control behaves effectively the same as the mechanical push/pull controls of a DM, as altering the piston phase of a single sub-aperture output is essentially the same as changing the optical path of a single beam segment reflecting off of a DM. Therefore, we can treat a mechanically static, tiled aperture, phased array, with piston phase control, as a crude DM without tip/tilt beam control capabilities. Such an array can then potentially correct for, at the

very least, low order atmospheric phase distortions introduced to the tiled array optical output. All that needs to be done is somehow collect an optical return signal from an illuminated object in the far field to act as a feedback signal for the phase control electronics.
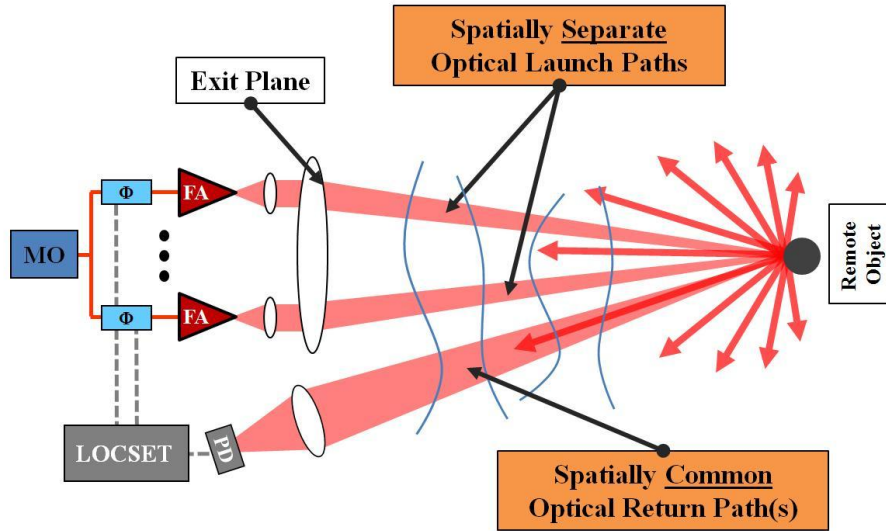
Figure 52: Conceptual setup of the LOCSET Object In the Loop (OIL) coherent beam combination system.

Looking at Figure 52 we see a conceptual drawing of an Object In the Loop (OIL) phase locking system, pioneered by this author [51,52,53,57], utilizing the LOCSET control electronics for phase optimization. The OIL beam combination system starts with a single master oscillator (MO), the output of which is coupled into a single fiber patch cable and then split into N individual fiber channels for later combination in the far field. The light in each fiber channel is phase controlled via a LiNbO$_3$ phase modulator providing the LOCSET control electronics piston phase control of each of the N beams. After the LiNbO$_3$ phase modulators, the light in each of the N channels is optically amplified and launched from a tiled array of individual, spatially separate, array sub-

177

apertures. Unlike previously demonstrated LOCSET beam combination systems the light from the array is not sampled via a partial reflector before propagating to the far field. Instead the light is simply allowed to propagate to the remote object with each beam in the array output experiencing unique optical phase disturbances due to atmospheric effects (if the beams are significantly small they will experience primarily piston phase errors with little or no higher order aberrations). Each beam is then incident on a remote object in the far field, a ball bearing in Figure 52, where a percentage of the light, that which is not absorbed or misses that remote object all together, is scattered in many directions, some of which is directed back in the general direction of the array launch optics. In the same plane as the array launch optics is a spatially separate collection aperture consisting of a single lens and photodetector, drawn just below the launch optics in Figure 52. Said collection aperture collects a fraction of the light scattered from the remote object and focuses it onto a photodetector. The signal from the photodetector is then utilized by the LOCSET control electronics to apply the appropriate piston phase corrections to each array sub-aperture to minimize the optical phase difference between all beams in the array at the photodetector. Because the light from each array sub-aperture, scattering off of the remote object and collected at the collection aperture, follows a common 'return' path (i.e. perfectly overlapped) any phase disturbances introduced to the collected light while propagating along the return path will be common and therefore not change the difference in phase between each beam as measured at the remote object. Therefore, by minimizing the optical phase difference between each beam in the system at the collection aperture in the plane of the tiled array the beams will be coherently optimized at the remote object! This beam combination system effectively

includes the remote object in the phase control loop and is known as Object In the Loop (OIL) phase locking.

7.3.1 Laboratory Demonstration of OIL Phase Locking

It is important to mention that Object In the Loop (OIL) phase locking via LOCSET is not just an idea but a demonstrated reality. Late in 2008 OIL phase locking via LOCSET was demonstrated by this author for the first time in the AFRL Joint High Power Fiber Amplifier test bed [51,52,53,57]. For said demonstration a tiled array of three 5W beams, arranged in a triangle pattern, was utilized. The 3 collimated optical outputs of the tiled array were then focused via a lens to create a 'far field' diffraction pattern governed by array arrangement and sub-aperture optical fill factor. Said pattern was then re-imaged and magnified onto a flat black beam dump nearly 14 feet away at the end of the optical table. A single ball bearing, resting on an optical post, was placed in the magnified far field image of the combined beam to behave as a point source reflector/scatterer. A fraction of the light scattering/reflecting off of the ball bearing was then collected via a simple collection lens, in the same plane as the final turning mirror of the tiled array output, and focused onto the active area of a photodetector. The signal of said photodetector was then feed to the LOCSET control electronics to establish coherent beam combination on the ball bearing.
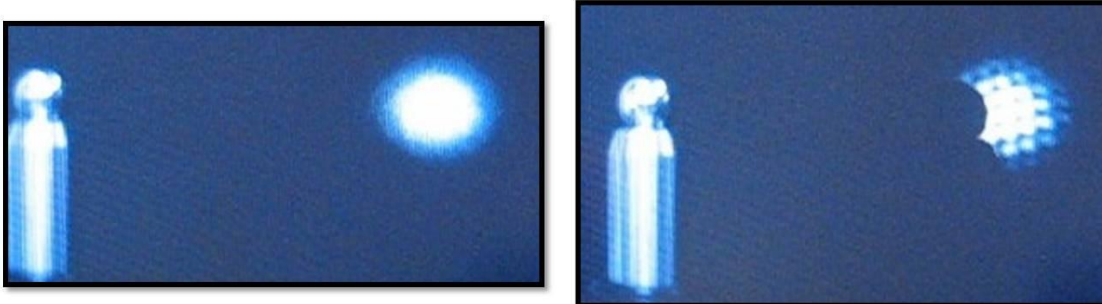
Figure 53: Screen shots from video of first ever Object In the Loop (OIL) phase locking demonstration. 3 beams, arranged in a triangular array pattern are coherently combined on a spatially remote object, a stainless steel ball bearing. Left: ball bearing not in beam path; system unable to phase lock (no return signal). Right: tiled array coherently combined when ball bearing is in the beam path (note the presence of fringes in the image plane).

The results of said demonstration are represented in Figure 53 as screen shots from a video taken during OIL operation. The left most image in Figure 53 shows a large washed out, or blurry, beam incident on the backdrop with the ball bearing positioned out of the beam path. The combined beam is washed out because there is no optical return signal incident on the photodetector feeding the LOCSET electronics leaving beam combination behavior to the erratic whims of noise in the control circuit. The result is an erratic time varying phase behavior, and therefore erratic time varying intensity behavior, of the combined beam while the control circuit searches for a correction signal. Now look at the right most image of Figure 53. The ball bearing is position in the beam path, as evidence by the shadow of the ball bearing on the backdrop, with the combined beam exhibiting distinct interference fringes in the image plane indicating coherent beam optimization on the remote object. With the ball bearing in the beam path laser light is scattered into a very large solid angle, some of which is collected by the collection aperture feeding the LOCSET control electronics. This optical feedback signal contains all the phase error information needed, governed by the LOCSET discussion in Chapter

180

3, to coherently combine the 3 beams onto the remote object. When atmospheric turbulence was introduced to both the launch and return beam paths, via a heat gun, the system maintained piston phase controlled phase lock on the ball bearing.

It is important to remind the reader that the OIL phase locking system is unable to account for spatial phase disturbances beyond piston phase control. When atmospheric turbulence was introduced to the beam path of the tiled array, via a simple heat gun, tip and tilt aberrations were often observed in the individual propagation paths of the 3 beams. As long as the beams remained overlapped on the ball bearing, therefore providing an optical return signal at the LOCSET photodetector, the OIL phase locking system would maintain phase lock and coherently combined the tiled output on the object in the far field. Due to the pointing errors from the un-corrected tip and tilt aberrations the combined beam was not at its optimal diffraction limit. With that said, beam combination performance was still observably better than without OIL phase locking.

7.4. Chapter Summary:

In this chapter the LOCSET control electronics, previously confined to local coherent beam combination at, or near, the exit aperture of a beam combination system, were extended to include light reflected/scattered off of a remote object as part of the control feedback loop in a technique known as Object In the Loop (OIL) phase locking. When coherently combining the output of a tiled array onto a remote object said adaptation will correct for low order, atmospheric turbulence induced, phase aberrations encountered by the propagating array of beams. To date OIL phase locking has been demonstrated in a laboratory setting at a distance of approximately 14 feet with plans to demonstrate, and further diagnose, the beam combination technique in a turbulent outdoor environment.

Chapter 8. Research Summary and Future Work

As you, the reader, are fully aware, experimental science is most often a team endeavor. Even if the present, or most recent, work is entirely your own someone before you likely paved the way for you via an idea, prototype, or a functioning component to be later incorporated in your research. The research discussed in the dissertation is no exception to this general rule. The LOCSET electronics were not this author's idea or personal invention. In no way does this author wish, or intend, to take credit for the fundamental development of the LOCSET phase locking technology. Instead, LOCSET is the pre-existing idea and prototype from which this author's research, the work detailed in this dissertation, is built upon. In the text to follow I will provide a brief summary of the theory and experimentation performed and discussed in detail in previous chapters. In the same breath of explanation, I will also call out my unique contribution to the work presented. The chapter will then conclude with a brief discussion on future plans for the LOCSET and OIL technologies.

8.1. Theory and Operation of LOCSET

Chapter 3 outlined in great detail the theory and fundamentals of LOCSET operation. The chapter began with a discussion on basic beam combination and established the need for active piston phase control when coherently combining the output of multiple fiber amplifiers into a single output. The text then proceeded to define and develop the complete LOCSET error signal for a single channel in a broader coherent beam combination system. This author then developed the first detailed error analysis of the complete LOCSET error signal expression for a single channel and showed that, for the following strictly defined control loop integration time conditions,

$$\tau \gg \frac{2\pi}{\left| \omega_x - \omega_{j \neq x} \right|},$$ 3.39

$$or$$

$$\tau \cdot \Delta\omega = N \cdot 2\pi,$$ 3.76

$$\&$$

$$\tau \cdot \omega_i = M \cdot 2\pi,$$ 3.77

where M and N are independent integers, the complete Self-Reference LOCSET error

signal, S_{SRx}, for a single channel reduced nicely to the following expression,

$$S_{SRx} = R_{PD} \cdot P_x^{\frac{1}{2}} \cdot J_1\left(\beta_x\right) \left(P_u^{\frac{1}{2}} \sin\left(\phi_u - \phi_x\right) + \frac{1}{2} \sum_{\substack{j=1 \\ j \neq x}}^{N-1} P_j^{\frac{1}{2}} \cdot J_o\left(\beta_j\right) \cdot \sin\left(\phi_j - \phi_x\right) \right).$$ 3.73

It was then shown that the un-modulated reference beam utilized in the Self-Referenced

LOCSET configuration was not required to maintain a suitable error single. This was

accomplished by simply setting the optical power of the un-modulated reference beam to

zero. This reference beam free technique is known as Self-Synchronous LOCSET and its

error signal is written as follows,

$$S_{SSx} = R_{PD} \cdot P_x^{\frac{1}{2}} \cdot J_1\left(\beta_x\right) \frac{1}{2} \sum_{\substack{j=1 \\ j \neq x}}^{N-1} P_j^{\frac{1}{2}} \cdot J_o\left(\beta_j\right) \cdot \sin\left(\phi_j - \phi_x\right).$$ 3.74

The two elegant expressions for the LOCSET error signal form the basic principles from

which the LOCSET phase locking electronics are physically built upon.

The chapter was then concluded with a discussion on the physical implementation of

the LOCSET electronics under practical constraints of electrical and optical components.

Said constraints were evidenced in a simple example demonstrating that, for typical off

the shelf components, the LOCSET electronics would be unable to perfectly track and

correct for significantly large, though physically realizable, phase changes in the optical

sources. These physical constraints were then overcome with the introduction of a

conceptually straight forward digital reset circuit capitalizing on the optical interference

condition that if the phase difference between multiple beams is an integer multiple of 2π,

and not just 0, the beams will constructively interfere (assuming coherence length

requirements are met). This behavior is nicely evidenced in the following 2 beam

interference equation,

$$\frac{Int(\Delta\phi)}{Int_o}\bigg|_{MAX} = 2\big(1+\cos(0)\big) = 2\big(1+\cos(2\cdot N\cdot\pi)\big) = 4, \qquad 3.1$$

demonstrating constructive interference between 2 beams of equal intensity for phase

differences of $N2\pi$ where N is an integer including 0.

  As was stated before, this author did not invent, or participate in inventing, the

LOCSET electronics [41,42,43]. That honor belongs to Dr. Thomas Shay, formerly of

AFRL and UNM [41,42,43]. Portions of the theory governing LOCSET operation were

previously derived and published even before this author's employment with the Air

Force [34,37,39]. In regards to the theory of LOCSET this author's unique contribution to

the work rests primarily in re-deriving and extending the complete LOCSET error signal,

with no simplification in error signal terms, and then, for the first time, performing the

rigorous error signal analysis leading to the integration time conditions that must be met

for optimal LOCSET operation.

8.2. Theory of Optical Phase Error Measurements: Single and Multi-Channel Systems

The theory of optical phase behavior measurements, presented in Chapter 4, was included in this dissertation to support/justify the experimental use of said technique in separate single amplifier and low power beam combination experiments. The chapter began with an introduction to the physical implementation of optical phase behavior measurements on a single channel system (i.e. measure the phase behavior of a single fiber amplifier). Said introduction was to provide a basic understanding of phase behavior measurements before proceeding into the basic theory of measuring the optical phase of a single or multi-channel beam with respect to a phase stable, frequency shifted, reference beam. The chapter then proceeded in relating the optical phase state of a single or multi-channel beam to the measureable quantities, the in-phase (I) and quadrature (Q) components, of the resulting photocurrent measured at the optical photodetector as shown in the following equation,

$$\Delta\phi = \tan^{-1}\left(\frac{Q(\Delta\phi)}{I(\Delta\phi)}\right). \qquad 4.23$$

This result provides the basis for an elegant and useful method of measuring the optical phase behavior of a single or multi-channel beam with respect to a phase stable, frequency shifted, reference beam.

It is important to make clear that this author is not an early pioneer of such phase behavior measurements described in this chapter. That honor primarily belongs to Dr. Scott of QinetiQ UK and Dr. Fan of MIT Lincoln Laboratories as their work is most often cited in relation to optical phase behavior measurements [63,64,65]. Instead, this

author's unique contribution stems from building and implementing, in both hardware and software, a similar phase behavior measurement based on the limited info obtained from Dr. Scott's and Dr. Fan's publications and then, to the best of this authors knowledge, for the first time, applying said measurements to characterizing the phase locking performance of coherently combined beams.

8.3. Experimental Results: Phase Fluctuations in a 100W Fiber Amplifier

Chapter 5 was wholly devoted to optical phase behavior measurements of a single 100W fiber amplifier, built by NuFern, and utilized in the Joint High Power Fiber Amplifier Test Bed here are AFRL. Early on in the text the reader was re-introduced to the single channel phase behavior measurement as it is implemented in the 100W fiber amplifier phase behavior demonstration. The chapter then proceeded with establishing the effective measurement noise, including all environmental phase disturbances, of approximately $\lambda/30$. Said information provided a baseline for phase behavior measurements to occur during amplifier turn on and steady state operation. The results of said measurements indicated that quantum defect heating during amplifier turn on is the primary contributor to the change in optical phase of the light emitted at the amplifier output. After the system reached steady state operation temperature fluctuations in the amplifier cold and hot plate controllers dominated the changes in optical phase. The chapter then concluded with a brief discussion on LOCSET's capability of keeping up with the measured phase behavior during both turn on and steady state operation of the amplifier.

It is important to make clear that phase behavior measurements on single beam systems are nothing new. As alluded to above, Dr. Scott and Dr. Fan each performed similar phase behavior measurements on their respective fiber amplifier systems

[63,64,65]. This author's work is unique in that this was the first time such measurements had been applied to the 100W amplifiers, built by NuFern, and utilized in the Joint High Power Fiber Amplifier Test Bed here at AFRL.

8.4. Experimental Results: 2 – 32 Channel Coherent Beam Combination via the LOCSET Phase Locking Technique

In Chapter 6 the reader was provided with a general description of the setup and implementation of 2 through 32 channel LOCSET coherent beam combination systems and necessary phase behavior and intensity measurement diagnostics. Said beam combination systems demonstrated RMS phase error performance as low as $\lambda/71$ for 32 low power coherently combined beams. This is the highest measured phase fidelity for any electronically phased fiber array for comparable channel counts. The chapter then concluded with a discussion on the effect of such phase errors on a typical tiled array coherent beam combination system demonstrating that, for un-correlated RMS phase errors of $\lambda/65$ across individual array sub-apertures, the resulting reduction in the combined beam Strehl ratio would be less than 1% for up to 100 array elements [77]. This author therefore demonstrated that the optical outputs of a large number of fibers can be coherently combined with high fidelity using the LOCSET phase locking technique.

As stated above, this author is not the inventor of the LOCSET phase locking technique. That honor belongs to Dr. Thomas Shay, formerly of AFRL and UNM [41,42,43]. This author's unique contribution to the LOCSET technology rests primarily in utilizing it to demonstrate coherent combination of 32 low power beams with record RMS phase errors of approximately $\lambda/71$. The previous LOCSET channel count record

was 16 channels with RMS phase errors of approximately λ/25. Said accomplishment(s) stemmed from significant adaptations to the broader beam combination system while leaving the LOCSET electronics, for the most part, unaltered. Though not discussed in this dissertation this author also broke the previous performance record for a 2 channel LOCSET beam combination by demonstrating RMS phase an errors of approximately λ/84 (previous record was approximately λ/60 RMS).

8.5. Future Work: Including a Remote Object In the Control Loop

Chapter 7 outlined the basic behavior and first ever demonstration of Object In the Loop (OIL) beam combination via the LOCSET phase locking technique. In previous demonstrations the LOCSET control electronics were confined to local coherent beam combination at, or near, the exit aperture of a beam combination system. This author extended the conventional LOCSET technique to include light reflected/scattered off of a remote object, incident on a collection aperture via a spatially separate return path, as part of the control feedback loop resulting in OIL beam combination. When coherently combining the output of a tiled array onto a remote object this adaptation automatically corrects for low order, atmospheric turbulence induced, phase aberrations encountered by the propagating array of beams. To date OIL phase locking has been demonstrated in a laboratory setting at a distance of approximately 14 feet with plans to demonstrate, and further diagnose, the beam combination technique in a turbulent outdoor environment.

For fear of sounding boastful this author was the first to propose the OIL adaptation to the LOCSET phase locking technique. This author then proceeded to be the first to demonstrate coherent beam combination on a remote object, technique described above and in Chapter 7, while utilizing the LOCSET electronics. Said demonstration has

resulted in a patent submission [51] and 3 well received conference papers/presentations [52,53,57].

8.6. Possible Future Work: LOCSET and OIL Beam Combination

Research on LOCSET and OIL phase locking could go any number of directions as there are a lot of questions that need to be answered. Pertaining to the more conventional local LOCSET technique, the primary research direction is in scaling up the total number of optical beams phase locked. To date up to 32 coherently combined beams have been demonstrated… is it possible to demonstrate 48? What about coherently combining 64 beams? The lack of degradation when scaling LOCSET from 2 to 32 elements suggests that channel scaling even further will be successful. Ultimately what needs to be determined is how many channels can be physically implemented before running into experimental issues (i.e. photodetector saturation, electronic amplifier saturation, electronic bandwidth limitations, etc.)? These are very important questions to have answered when considering future channel scaling efforts of the LOCSET beam combination technology. As a practical matter, one needs to determine how many beams are required for specific applications.

In regards to OIL phase locking, quite possibly the most important question that needs addressed is how well will OIL phase locking perform when beam combining onto a remote, rough, extended object? This object could be as simple as a rough surfaced, flat, metal plate. Will the system be able to phase lock to such an object? If the combined beam does appear to coherently combine on an extended object, likely evidenced by the presence of interference fringes, how optimal is said beam combination in the presence of extra spatial phase information collected at the collection aperture? The issue here is the

collection of scattered light from multiple point sources along the surface of the extended

object, containing extra spatial phase information, feeding the LOCSET control

electronics (vs. locking to a single point source scatter as previously demonstrated).

Finally, how does the speckling of the scattered light effect OIL phase locking

performance? Does the system actually phase lock on such a surface? If so, again, is the

combined beam actually optimized? If any of the issues present in these questions prove

insurmountable by the current iteration of OIL phase locking then is it possible to adapt

the present OIL beam combination technique to mitigate said issues? Can mitigation be

accomplished without significantly increasing system complexity? These are very

important questions to have answered when considering future use for the OIL phase

locking technology. Once again, the basic practical question is what level of performance

is necessary to meet the requirements for specific applications.

Another important question that needs to be addressed is how well will the OIL

phase locking technique work in an outdoor environment? Disturbing the air in a

laboratory with a heat gun is one thing but performing OIL phase locking, at greater than

laboratory distances, in the controlled chaos of atmospheric turbulence is another. The

first question that needs to be addressed is whether or not enough scattered light, from the

remote object, can be collected to provide the LOCSET control electronics with a suitable

error correction signal? The result of this inquiry will strongly depend on distance, the

material of the scattering object, and the objects angular position. The next question to be

addressed is at what distance will the optical time of flight affect beam combination

performance on the remote object? The further away the remote object the longer it takes

light to make a complete round trip from the launch aperture, to the remote object, and

back to the collection aperture. If this round trip time is longer than the time scale of atmospheric changes then the system will not optimally combine the beams on the remote object. All these questions, and many more, still need to be addressed as, to date, OIL phase locking has only been performed as a simple demonstration in the AFRL Joint High Power Fiber Amplifier Test Bed.

References

1. Maiman, T. (1960), "Stimulated Optical Radiation in Ruby," *Nature*, Vol. 187, 493-494

2. Towns, C. (2003). "The First Laser." Garwin & Lincoln (Eds.), *A Century of Nature* (107-112), Chicago, Il: Univ. of Chicago Press

3. McNaught, S., et. al., (2009), "100kW Coherently Combined Slab MOPAs." *CLEO: Lasers & Electro-Optics*, pgs. 1-2

4. McNaught, S., et. al. (2009), "100kW Coherently Combined Nd:YAG MOPA Laser Array." *Frontiers In Optics, OSA Technical Digest*, paper: FThD2

5. Snitzer, E. (1961), "Optical Maser Action of Nd^{+3} in a Barium Crown Glass." *Physical Review Letters*, Vol. 7, Iss. 12, pgs. 444 – 449

6. Snitzer, E. (1961), "Proposed Fiber Cavities for Optical Masers." *Journal of Applied Physics*, Vol. 32, Iss. 1, pgs. 36 – 39

7. Galvanauskas, A. (July 2004), "High Power Fiber Lasers." *Optics & Photonics News*, pgs. 42 – 47

8. Mears, R., et. al. (1985), "Neodymium Doped Silica Single Mode Fiber Laser." *Electronics Letters* Vol. 21, pgs. 738 – 740

9. Poole, P., et. al. (1985), "Fabrication of low loss optical fibers containing rare-earth ions." *Electronics Letters*, Vol. 21, pgs. 737 – 738

10. Snitzer, E., et. al. (1988), "Double Clad, Offset Core, Nd Fiber Laser." *OSA Technical Digest Series, Optical Fiber Sensors*, Paper: PD5-2

11. Richardson, D., et. al. (2010), "High power fiber lasers: current status and future perspectives." *Journal of the Optical Society of America*, Vol. 27, Iss. 11, pgs. B63 – B92

12. Dominic, V., et. al. (1999), "110W fibre laser." *Electronics Letters*, Vol. 35, Iss. 14, pgs. 1158 – 1160

13. Stiles (2009), "New Developments in IPG Fiber Laser Technology." Proceedings of the 5th International Workshop on Fiber Lasers

14. IPG Photonics. (2010), "IPG Photonics – The Power To Transform." Retrieved From: www.ipgphotonics.com/apps_materials_multi_advantages.html

15. Gray, S., et. al. (2007), "502 Watt, single transverse mode, narrow linewidth, bidirectionally pumped Yb-doped fiber amplifier." *Optics Express*, Vol. 15, Iss. 25, pgs. 17044 – 17050

16. Jeong, Y., et. al. (2007), "Power Scaling of Single Frequency Ytterbium Doped Fiber Master Oscillator Power Amplifier Sources up to 500W." *IEEE Journal of Selected Topics in Quantum Electronics*, Vol. 13, Iss. 3, pgs. 546 – 551

17. Robin, C., et. al. (2010), "Experimental and theoretical studies of single frequency PCF amplifier with output of 400W." *Proc. of SPIE*, Vol. 7580, pgs. 75081I-1 – 75081I-11

18. Robin, C., et. al. (2011), "Experimental studies of segmented acoustically tailored photonic crystal fiber amplifier with 494 W single-frequency output." *Proc. of SPIE*, Vol. 7914, pgs. 79140B-1 – 79140B-8

19. Robin, C. (2011). *Novel Approaches to Power Scaling of Single-Frequency Photonic Crystal Fiber Amplifiers*, Albuquerque, NM: University of New Mexico

20. Goodno, G., et. al. (2007), "Brightness-Scaling Potential of Actively Phase-Locked Solid-State Laser Arrays." *IEEE Journal of Quantum Electronics*, Vol. 13, Iss. 3, pgs. 460 – 472

21. Anderegg, J., et. al. (2006), "Coherently Coupled High Power Fiber Arrays." *Proc. of SPIE*, Vol. 6102, pgs. 61020U-1 – 61020U-5

22. Cheung, E., et. al. (2008), "Diffractive-optics-based beam combination of a phase-locked fiber laser array." *Optics Letters*, Vol. 33, Iss. 4, pgs. 354 – 356

23. Goodno, G., et. al. (2010), "Active phase and polarization locking of a 1.4 kW fiber amplifier." *Optics Letters*, Vol. 35, Iss. 10, pgs. 1542 – 1544

24. Goodno, G., et. al. (2006), "Coherent combination of high-power zigzag slab laser." *Optics Letters*, Vol. 31, Iss. 9, pgs. 1247 – 1249

25. Vorontsov, M., et. al. (1997), "Adaptive Phase Distortion Correction Based On Parallel Gradient Descent Optimization." *Optics Letters*, Vol. 22, Iss. 12, pgs. 907 – 909

26. Liu, L., et. al. (2007), "Adaptive Phase-Locked Fiber Array with Wavefront Phase Tip-Tilt Compensation using Piezoelectric Fiber Positioners." *Proc. of SPIE*, Vol. 6708, pgs. 67080K-1 – 67080K-12

27. Wang, X., et. al. (2009), "Coherent Beam Combination of Two W-Level Fiber Amplifiers in Turbulence Atmospheric Environment Based on Stochastic Parallel Gradient Descent Algorithm." *Laser Physics: Coherent Phenomena and Holography*, Vol. 19, Iss. 5, pgs. 984 – 988

28. Zhou, P., et. al. (2009), "Coherent Beam Combination of Two Dimensional High Power Fiber Amplifier Array Using Stochastic Parallel Gradient Descent Algorithm." *Applied Physics Letters*, Vol. 94, Iss. 231106, pgs. 231106-1 – 231106-3

29. Zhou, P., et. al. (2009), "Coherent Beam Combination of Three Watt-Level Fiber Amplifiers Using a DSP-Based Stochastic Parallel Gradient Descent Algorithm." *Chinese Physics Letters*, Vol. 26, Iss. 4, pgs. 044202-1 – 044202-4

30. Zhou, P., et. al. (2009), "Coherent Beam Combining of Two Fiber Amplifiers Using Stochastic Parallel Gradient Descent Algorithm." *Optics & Laser Technology*, Vol. 41, pgs. 853 – 856

31. Cauwenberghs, G. (1993), "A Fast Stochastic Error-Descent Algorithm for Supervised Learning and Optimization." *Proc. of Advances in Neural Information Processing Systems*

32. Kansky, J., et. al. (2006), "Beam control of a 2D polarization maintaining fiber optic phased array with high fiber count." *Proc of SPIE*, Vol. 6306, pgs. 63060G-1 – 63060G-11

33. Shay, T. (2007), "Theoretical Model for Self-Synchronous Locking of Optical Coherence by Single-detector Electronic Frequency Tagging." *CLEO Proceedings,* paper: CWD2

34. Shay, T. (2006), "Theory of electronically phased coherent beam combination without a reference beam." *Optics Express*, Vol. 14, Iss. 25, pgs. 12188 – 12195

35. Shay, T., et. al. (2009), "A Novel Technique for Electronic Phasing of High Power Fiber Amplifier Arrays." *Proc. of SPIE*, Vol. 7386, pgs. 73860W-1 – 73860W-8

36. Shay, T., et. al. (2009), "High power phase locking of a fiber amplifier array." *Proc. of SPIE*, Vol. 7195, pgs. 71951M-1 – 71951M-8

37. Shay, T., et. al. (2007), "Self-Synchronous and Self-Referenced Coherent Beam Combination for Large Optical Arrays." *IEEE Journal of Selected Topics in Quantum Electronics*, Vol. 13, Iss. 3, pgs. 480 – 486

38. Shay, T., et. al. (2010), "Phasing Locking of High Power Fiber Amplifier Arrays." *OSA: Proc. of ASSP*, paper: AMA1

39. Shay, T., et. al. (2006), "First experimental demonstration of self-synchronous phase locking of an optical array." *Optics Express*, Vol. 14, Iss. 25, pgs. 12015 – 12021

40. Shay, T., et. al. (2007), "Narrow Linewidth Coherent Beam Combining of Optical Fiber Amplifier Arrays." *Proc. of SPIE*, Vol. 6451, pgs. 64511N-1 – 64511N-15

41. Shay, T. (2007). "Self-Referenced Locking of Optical Coherence by Single Detector Electronic-Frequency Tagging," *U.S. Patent No. 7233433*. Washington, DC: U.S. Patent and Trademark Office

42. Shay, T. (2007). "Self-Referenced Locking of Optical Coherence By Single Detector Electronic Frequency Tagging," *U.S. Patent No. 7187492*. Washington, DC: U.S. Patent and Trademark Office

43. Shay, T. (2006). "Self-Synchronous Locking of Optical Coherence By Single Detector Electronic-Frequency Tagging," *U.S. Patent No. 7058098*. Washington, DC: U.S. Patent and Trademark Office

44. Fan, T., et. al. (2010), "Coherent Combining of a Seven Element Hexagonal Fiber Array." *Optics & Laser Technology*, Vol. 42, 274 – 279

45. Zhou, P., et. al. (2009), "Coherent Beam Combining of Fiber Amplifiers Using Stochastic Parallel Gradient Descent Algorithm and its Application." *IEEE Journal of Selected Topics in Quantum Electronics*, Vol. 15, Iss. 2, pgs. 248 – 256

46. Zhou, P., et. al. (2009), "Coherent Beam Combination of a Hexagonal Distributed High Power Fiber Amplifier Array." *Journal of Applied Optics*, Vol. 48, Iss. 33, pgs. 6537 – 6540

47 Uberna, R., et. al. (2010), "Coherent Polarization Beam Combination." *IEEE Journal of Quantum Electronics*, Vol. 46, Iss. 8, pgs. 1191 – 1196

48 Uberna, R., et. al. (2010), "Power scaling of a fiber master oscillator power amplifier system using a coherent polarization beam combination." *Applied Optics*, Vol. 49, Iss. 35, pgs. 6762 – 6765

49. Dong, H., et. al. (2009), "Coaxial Combination of Coherent Laser Beams." *Chinese Optics Letters*, Vol. 7, Iss. 11, pgs. 1012 – 1014

50. Rice, R., et. al. (2008). "Coherent Fiber Diffractive Optical Element Beam Combiner," *U.S. Patent No. 7440174*. Washington, DC: U.S. Patent and Trademark Office

51. Pulford, B., et. al. (Pending). "Remote Phase Locking an Array of Optical Amplifiers," *U.S. Patent No. (Pending)*. Washington, DC: U.S. Patent and Trademark Office

52. Pulford, B., et. al. (2010), "Phase Locking an Array of Fiber Amplifiers onto a Remote Object." *CLEO*, paper: CThO5

53. Pulford, B., et. al. (2009), "Phase Locking of a Fiber Array onto a Remote Object." *Solid State Diode Laser Technology Review*, paper: Beam Control – Pulford

54. Bourdon, P., et. al. (2008), "Coherent beam combining of fiber amplifier arrays and application to laser beam propagation through turbulent atmosphere." *Proc. of SPIE*, Vol. 6873, pgs. 687316-1 – 687316-9

55. Bourdon, P., et. al. (2009), "Theoretical analysis and quantitative measurements of fiber amplifier coherent beam combining on a remote surface through turbulence." *Proc. of SPIE*, Vol. 7195, pgs. 719527-1 – 719527-8

56. Jolivet, V. et. al. (2009), "Beam Shaping of Single-Mode and Multimode Fiber Amplifier Arrays for Propagation Through Atmospheric Turbulence." *IEEE Journal of Selected Topics in Quantum Electronics*, Vol. 15, Iss. 2, pgs. 257 – 268

57. Pulford, B., et. al. (2009), "Atmospheric Compensation via Separate Return Path Remote Phase Locking." *Directed Energy Professional Society Beam Control Conference*, Monterey, CA

58. Hecht, E. (2002). *Optics (4th ed.)*. San Francisco, CA: Addison Wesley

59. Klein, M., Furtak, T. (1986). *Optics (1st ed.)*. USA: John Wiley & Sons

60. Gradshteyn, Ryzhik. (1965). *Tables of Integrals, Series, and Products*. London: Academic Press

61. McNaught, S., et. al. (2010), "Coherent Combining of a 1.26-kW Fiber Amplifier." *Proc. of the Optical Society of America*, paper: a154_1

62. Zhou, P. et. al. (2009), "Coherent beam combination of three two-tone fiber amplifiers using stochastic parallel gradient descent algorithm." *Optics Letters*, Vol. 34, Iss. 19, pgs. 2939 – 2942

63. Augst, S., et. al. (2004), "Coherent beam combining and phase noise measurements of ytterbium fiber amplifiers." *Optics Letters*, Vol. 29, Iss. 5, pgs. 474 – 476

64. Jones, D., et. al. (2007), "Phase stabilization of a large-mode-area ytterbium-doped fiber amplifier." *Optics Letters*, Vol. 32, Iss. 5, pgs. 466 – 468

65. Jones, D., et. al. (2007), "Characterization and stabilizing dynamic phase fluctuations in large mode area fibres." *Proc. of SPIE*, Vol. 6453, pgs. 64530Q-1 – 64530Q-10

66. Seeley, D. (2010), *Analysis and Modeling of Phase Noise in LOCSET and the AFRL High Power Fiber Test Bed*. Albuquerque, NM: University of New Mexico

67. Dawson, J, et. al. (2008), "Analysis of the scalability of diffraction-limited fiber lasers and amplifiers to high average power." *Optics Express*, Vol. 16, Iss. 17, pgs.13240 – 13266

68. Edgecumbe, J., et. al. (2008), "Kilowatt-Level PM Amplifiers for Beam Combination." *OSA/FiO/LS/META/OF&T*, paper: FTuJ2

69. Hofer, S., et. al. (2001), "Single-frequency master-oscillator fiber power amplifier system emitting 20W of power." *Optics Letters*, Vol. 26, Iss. 17, pgs. 1326 – 1328

70. Jeong, Y., et al. (2005), "Single-frequency, single-mode, plane-polarized ytterbium-doped, fiber master-oscillator power amplifier source with 264 W output power." *Optics Letters*, Vol. 30, Iss. 5, pgs. 459 – 461

71. Yu, C., et al. (2011), "Coherent combining of a 4 kW, eight-element fiber amplifier array." *Optics Express*, Vol. 36, Iss. 14, pgs. 2686 – 2688

72. Flores, A., et. al. (2011), "Coherent Beam Combining of Fiber Amplifiers in a kW Regime." *CLEO/OSA*, paper: CFE3

73. Payne, D., et. al. (2005), "Kilowatt-class single frequency fiber sources." *Proc. of SPIE*, Vol. 5709, pgs. 133 – 141

74. Machewirth, D., et. al. (2007), "Current Developments in High Power, Monolithic, Polarization Maintaining Fiber Amplifiers for Coherent Beam combining Applications." *Proc. of SPIE*, Vol. 6453, pgs. 64531F-1 – 64531F-7

75. CVI Melles Groit. (2010). Optical Coatings and Materials. *All Things Photonic [The CVI Melles Groit Catalog]*. pg. 1.24

76 Paschotta, R., et al. (1997), "Ytterbium-Doped Fiber Amplifiers." *IEEE Journal of Quantum Electronics*, Vol. 33, Iss. 7, pgs. 1049 – 1056

77. Nabors, C. (1994), "Effects of phase errors on coherent emitter arrays." *Applied Optics*, Vol. 33, Iss. 12, pgs. 2284 – 2289

78. Milton, S, Arnold, J. (2003). *Introduction To Probability and Statistics 4*[th] *ed*. USA: McGraw-Hill